Laser-initiated Coulomb explosion imaging of small molecules

by

Jean-Paul Brichta

A thesis
presented to the University of Waterloo
in fulfillment of the
thesis requirement for the degree of
Doctor of Philosophy
in
Physics

Waterloo, Ontario, Canada, 2008

I hereby declare that I am the sole author of this thesis. This is a true copy of the thesis, including any required final revisions, as accepted by my examiners.

I understand that my thesis may be made electronically available to the public.

Abstract

Momentum vectors of fragment ions produced by the Coulomb explosion of $CO_2^{z+}(z = 3 - 6)$ and $CS_2^{z+}(z = 3 - 13)$ in an intense laser field ($\sim$50 fs, 1 x 10^{15} W/cm^2) are determined by the triple coincidence imaging technique. The molecular structure from symmetric and asymmetric explosion channels is reconstructed from the measured momentum vectors using a novel simplex algorithm that can be extended to study larger molecules. Physical parameters such as bend angle and bond lengths are extracted from the data and are qualitatively described using an enhanced ionization model that predicts the laser intensity required for ionization as a function of bond length using classical, over the barrier arguments.

As a way of going beyond the classical model, molecular ionization is examined using a quantum-mechanical, wave function modified ADK method. The ADK model is used to calculate the ionization rates of H_2, N_2 and CO_2 as a function of initial vibrational level of the molecules. A strong increase in the ionization rate, with vibrational level, is found for H_2, while N_2 and CO_2 show a lesser increase. The prospects for using ionization rates as a diagnostic for vibrational level population are assessed.

Acknowledgements

Many individuals contributed to the development of the ultrafast imaging system. Upon my arrival at the University of Waterloo in 2003, the instrument was in a very early stage of development. The design of the detector hardware was initiated by undergraduate student Robin Helsten and the early software development was performed by undergraduate Ian Szufnara. I took charge of the project and saw to the completion and debugging of the hardware and debugging of the data acquisition software. Assistance in the software development was provided by undergraduates Dwight Koji Fujita and James Nesbitt.

Early version data acquisition software and implementation of the mySQL data base was completed in 2005. Katia Bassenko provided assistance with the mySQL winnowing routine which selects triple coincidence events from the data. While I wrote the initial version of the simplex algorithm for fast molecular structure analysis, further development was provided by Aden Seaman.

Many other individuals made contributions to the system as it evolved. Professor Joseph Sanderson offered valuable advice and assistance throughout development. The laser system was constructed by Stephen Walker and Dr. Xiaoming Sun. Fabrication of the vacuum chamber, time-of-flight mass spectrometer and detector mount was performed by the staff of the Science Machine Shop. Funding for various research projects was provided by the Natural Science and Engineering Research Council, the Canadian Fund for Innovation and the Premier's Research Excellence Award.

Dr. Michael Spanner was ever a source of encouragement and provided vital programming assistance. Our discussions were particularly useful during the development of the ADK theoretical work. He is a champion bread-maker.

My father, Frank Brichta, provided moral and financial support throughout my education. Thanks for everything, Dad.

Dedication

This is dedicated to Jessica.

Contents

List of Tables

List of Figures

Chapter 1

Overview of Molecular Imaging

This chapter will introduce the structure of matter from a historical perspective, expanding in greater detail some of the common techniques for analyzing matter. The chapter will then delve into the details of Coulomb explosion imaging including previous significant experiments. The future of molecular imaging is hinted at with a brief description of the work to date on the imaging of molecular dynamics.

1.1 The Structure of Matter

Investigating the structure of matter is one of the fundamental tasks in chemistry and physics. The first atomic theories were developed in the 6th century BC by ancient Indian philosophers such as Kanada and Pakudha Katyayana. Indian atomists believed an atom could be one of six elements, with each element having up to twenty-four properties. They developed theories how atoms could combine into pairs, react, vibrate and perform other actions. They also suggested the idea of splitting an atom [1]. The earliest Western atomic theory was proposed by Leucippus of Miletus or Abdera in the first half of the 5th century BC. Leucippus believed that everything was composed of various imperishable, indivisible parts called atoms [2]. His student, Democritus of Abdera (BC 450-370) was responsible for the publication of the first atomic theory, and furthermore argued that atoms only possessed relatively few inherent properties, namely size, shape and mass. Other properties of matter, such as colour and taste, are the result of complex interactions between our bodies and the matter being observed [3].

The last three centuries have seen numerous advances in our understanding of atomic structure. Rudjer Boscovich [4] developed a modern atomic theory in the 18th century based largely on the principles of Newtonian mechanics [5]. In 1808, John Dalton [6] applied the atomic theory to chemistry and posited fundamental ideas such as the atomic uniqueness of different elements, indivisibility of atoms and combining atoms to create compounds. Ludwig Boltzmann contributed to the kinetic theory and developed the Maxwell-Boltzmann distribution for molecular

speeds in a gas independently from James Clerk Maxwell. Further advances would follow, including Rutherford's gold foil experiment in 1911 [7] which proved that most of an atom's mass was located in the nucleus, Bohr's model of the atom in 1913 [8] and Chadwick's discovery of the neutron in 1932 [9]. In 1916, Lewis provided the electron pair model for chemical bonding [10].

Despite these myriad advances in our understanding, our basic model still bears more than a passing resemblance to that of the earliest philosophers, that is that a molecule's composition is made of atoms which combine in various ways by chemical bonds.

1.2 Frequency Domain Spectroscopy

Although relatively recent measurement techniques such as atomic force microscopy allow for direct measurement of surfaces on the atomic scale, most of our knowledge of molecular structure comes from the study of periodic molecular motion, motion in the frequency domain. The simple Newtonian analogy of two balls joined by a spring has proven very robust for modeling diatomic molecules. In the simple model, if the masses are known, the force constant and length of the spring can be ascertained by measuring the vibrational and rotational frequencies [11]. Similarly, the vibrational and rotational spectra can be used to determine a molecule's equilibrium bond length and the strength of the bond [12]. While this model is very robust for diatomic molecules, polyatomic molecules can stretch, bend and oscillate in many ways. These additional degrees of freedom make molecular structure determinations exponentially more difficult as the number of atoms increases. Early pioneers such as Herzberg used pre-laser techniques to determine the structure of most small molecules by the middle of the twentieth century [13, 14, 15]. The invention and application of the laser in 1960 ushered in the era of high-resolution spectroscopy.

Although spectroscopy has been called "the study of the interaction of light with matter" [12], it has influenced many areas of modern science. The struggle to understand molecular spectra provided a direction for early quantum mechanics. Group theory found an application in the classification of molecular geometries. Observational astronomy was revolutionized with the new-found ability to analyze the chemical composition of stars and galaxies.

1.3 Scattering Techniques

While both spectroscopy and scattering techniques are used to measure molecular structure, they do so in complementary ways. As indicated earlier, the utility of frequency domain spectroscopy suffers when determining the structure of large molecules since the spectra are too complicated. To address this problem, several diffraction techniques were developed in parallel to spectroscopy [16, 17, 18]. In a

diffraction experiment, a molecular sample is bombarded with electrons, neutrons or X-rays whose de Broglie wavelength is shorter than the internuclear distance within the target. By analyzing the diffraction pattern, the molecular structure can be determined. The structure of countless crystalline materials have been determined over the last century by scattering techniques.

Biomolecules are a target of much interest and our structural knowledge of them is largely derived from scattering. X-ray diffraction was used to measure the structures of DNA [19], proteins [20] and enzymes [21]. Synchrotrons built in the 1960's provided an X-ray source for scattering experiments with improved flux and spatial resolution. However, synchrotrons are not viable for determining the molecular structure of large biomolecules. The x-ray diffraction process works best on large arrays of regularly spaced units with long range order. However, most large biomolecules cannot be crystallized and the subsequent x-ray diffraction signal is too low to measure even from large synchrotron sources. Furthermore, even if a sufficiently powerful synchrotron source did exist, its large X-ray flux would destroy the sample during the measurement process [22]. Fourth generation free-electron lasers will provide pulses of x-rays. The European X-ray Laser Project (XFEL) in Germany is presently under construction and is scheduled for completion in 2013.

1.4 Coulomb Explosion Imaging

Coulomb explosion imaging (CEI) is the general technique wherein a molecule is ionized and fragmented. The structure of the molecule is then inferred from the measurement of fragment momenta. Three methods have been used to initiate Coulomb explosions for the purpose of studying molecular structure. These methods are beam-foil, collision with highly charged ions, and laser-initiated explosion. The advent of each technique corresponded with technological maturation of particle and laser physics, respectively. The three approaches share several characteristics:

- only molecules in the gas phase are examined
- the interaction that initiates the Coulomb explosion is short and non-perturbative
- molecular structure is inferred from measurement of fragment momenta

Each technique and important results that were produced will be described in detail.

1.4.1 Beam-foil

Developed in 1978 at Argonne National Laboratory (USA) and the Weizmann Institute (Israel) [23], beam-foil CEI is a non-scattering technique that determines

molecular structure using nuclear and particle physics methods [24, 25]. In a beam-foil CEI experiment, a negatively charged molecular ion is accelerated to a kinetic energy on the order of MeV before impinging on an ultrathin (∼100 Å) foil target. Within an interaction time of ∼0.1 fs, many electrons are stripped off the molecular ion as it passes through the foil. Once it exits the foil, the molecular ion explodes due to the Coulomb repulsion of its positively charged atomic cores. By measuring the three-dimensional momentum of each fragment, the structure of the molecular fragment prior to explosion can be computed. Due to technological constraints, beam-foil CEI can only be used to measure the structure of small molecules which frequency domain spectroscopy has already been used to measure. Furthermore, the necessity to utilize highly energetic molecular ions limited the feasibility and scientific impact of the technique. Nevertheless, the technique did reveal previously unknown information about the structure of weakly bound molecules such as C_2H_2 and CH_2. Beam-foil CEI cannot measure molecular dynamics.

1.4.2 Highly charged ion

Beam-foil experiments require that sample molecules be accelerated to MeV energies and necessitate the use of a particle accelerator that costs millions of dollars. A much less expensive option is to fragment the sample molecule via collision with a highly charged ion (HCI). Like beam-foil, HCI cannot be used to measure dynamics.

When a highly charged ion (HCI) collides with a triatomic molecule, the molecule may be multiply ionized and then fragment into atomic ions each possessing relatively large kinetic energies. For example,

$$X^{8+} + CO_2 \rightarrow CO_2^{m+} \rightarrow O^{p+} + C^{q+} + O^{r+}, \tag{1.1}$$

where $m = p+q+r$. Throughout this work, the notation used to describe explosion channels will be written (p, q, r).

The simplest technique used to measure fragment kinetic energy is time-of-flight mass spectrometry (TOFMS) [26]. However, when a bent triatomic molecule Coulomb explodes, it is impossible to extract unambiguous momentum information from just the TOF signal. This is because the molecular fragments move in a plane, not just along the axis of the detector. During the mid-1990s, major advances were made in detector technology. Time-of-flight and position sensitive detection were combined so that it became possible to record the (x, y, t) information for each ionic fragment following a Coulomb explosion [27, 28].

Early work by Becker *et al.* [28] measured the double ionization and fragmentation of H_2 by 200 keV H^+ and He^+ ions. They found that the kinetic energy spectra of correlated protons emitted from the collisions was identical, regardless of whether H^+ or He^+ was used as the colliding ion. However, the kinetic energy measured was still somewhat lower than for a purely Coulombic process. The same group studied water shortly afterwards [29, 30]. Of particular interest were the

dynamics of the complete fragmentation process $H_2O \rightarrow H^+ + H^+ + O^{q+}$ ($q \geq 1$). In [29], the authors defined a practical choice of characteristic variables as shown in figure 1.1. Defined in velocity space, these variables are the angles χ and θ_v and contain a great deal of information about the fragmentation process. In particular, the angle χ between the velocity of the of the O^{q+} ion and the H^+–H^+ relative velocity was used to determine if the two H–O bonds broke simultaneously (concerted) or in a step-wise (sequential) manner. The concerted process is said to occur if both bonds break in a time which is short on the rotational and vibrational time scales of molecular motion. Two limiting cases illustrate the physics surrounding χ. If a concerted fragmentation always produced the same momentum values in all fragments, the cos χ distribution would look like a δ function. On the other hand, if sequential fragmentation always occurs, the OH fragment will have time to rotate about its centre of mass one or more times. In this case, cos χ will be a flat distribution. The results shown in figure 1.1 show that the fragmentation of water by 100 keV H^+ ions is largely concerted – the cos χ distribution is sharply peaked at $\chi = 90°$, with a characteristic width. For the (1,1,1) explosion channel, the angle θ_v was measured to be somewhat more bent than the equilibrium bond angle $\theta_0 \sim 105°$. This was attributed to the strong H^+–H^+ repulsion. When higher molecular charge states were analysed, θ_v approaches the equilibrium bond angle. Finally, the authors noted the weakness of the pure Coulomb model when reporting the kinetic energy distribution of coincident fragments. The measured kinetic energy distribution was narrower than that predicted using an MCSCF calculation taking into account the nine lowest molecular states of the intermediate H_2O^{3+} ion.

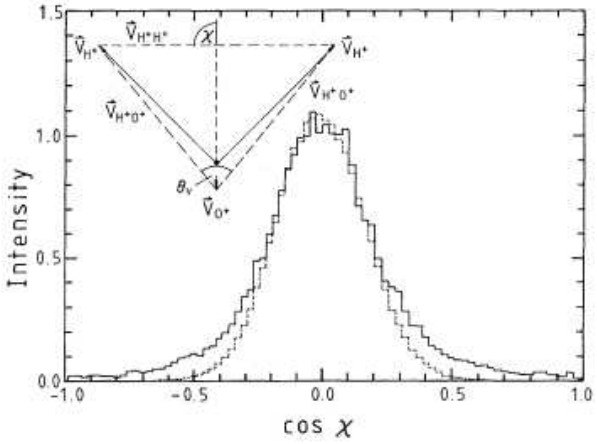

Figure 1.1: cos χ distribution of $H^+ + H^+ + O^+$ coincidences from collisions of 100 keV He^+ on H_2O (solid line). The dashed line is a simulation based on a MCSCF calculation assuming a concerted breakup of both H–O bonds. Reprinted with permission from [29]. © 1995 The American Physical Society.

Sanderson *et al.* [31] measured the structure of CO_2^{q+} (q=3–6) created by collision with 120 keV Ar^{8+} ions and reported a number of significant observations.

The bend angle or θ distribution of the (2,2,2) fragmentation pathway was seen to be extremely close to the zero-point motion for a neutral molecule. Furthermore, the kinetic energy of carbon ions should increase as the molecular skeleton is bent. The authors reproduced this trend and showed that the measured fragment kinetic energies were close to those expected from a purely Coulombic interaction. By considering the momentum vectors of two equally charged oxygen ions, the authors observed that the fragmentation process was largely concerted, not sequential. Finally, the authors reported the signal strengths of the various dissociation channels. However, these were not the true fragmentation cross-sections as the trigger probability of the data acquisition oscilloscope depended directly on the number of Auger electrons ejected from the collision. Therefore, higher charged molecular ions were more likely to be detected. Similarly, the structure of the bent NO_2 was studied [32] and, despite poor statistics, the authors observed satisfactory agreement between the reconstructed and zero-point bend angles.

Rajgara *et al.* [33, 34] undertook a detailed investigation of the fragmentation dynamics of CS_2^{q+} (q=3–10) using 120 keV $Ar^{6,8+}$ as the HCI . The authors noted that the bend angles reported in [31] and [32] approached the equilibrium bend angles when the charge state of the intermediate molecular ion was large. For this reason, they postulated that CS_2, which has a low single-ionization energy of 10.08 eV, would be an excellent candidate to study for high-charge state experiments. In particular, the authors hoped to test the validity of the Coulomb potential for fragmentation of highly charged molecular ions and note the relationship between parent charge state and recovered bend angle. The kinetic energy release (KER) was measured for the different fragmentation channels and compared with a pure Coulombic model where the equilibrium geometry was assumed and *ab initio*, quantum-chemical calculations based on an all-electron, self-consistent field (SCF) molecular orbital computation. The measured KER values were consistent with the Coulombic values, and, in most cases, more than the calculated ones. The authors postulated this discrepancy was due to ignoring higher electronic states. Therefore, it was suggested that their experimental findings pointed to the formation of precursor ions in electronically excited states. Another important finding was the likelihood of a particular molecular ion to fragment into a symmetric or asymmetric channel, as shown in figure 1.2. For example, CS_2^{5+} could fragment symmetrically into (2,1,2) or asymmetrically into (2,2,1). The data suggested that a molecular ion will preferentially fragment along the most exothermically favourable pathway. The χ-angle distribution indicated that fragmentation was instantaneous and concerted. The bend angle distributions were all 5–10° more bent than the most probable bend angle of 175.2°.

Chirality is an attribute of an object that is non-superimposable on its mirror image. The most common example are human hands. Chiral molecules are referred to as enantiomers and have substantial significance in fields such as pharmaceuticals. As traditional methods such as frequency domain spectroscopy cannot deduce a molecule's chirality, CEI was proposed as a potential solution. Kitamura *et al.* demonstrated the ability to determine a molecule's absolute chirality using CEI

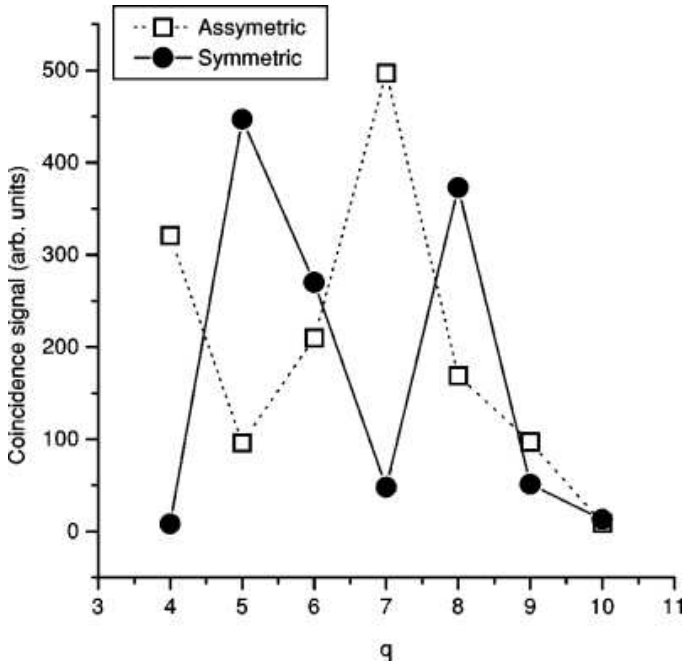

Figure 1.2: Propensity for fragmentation into symmetric (solid symbols and lines) and asymmetric channels (unfilled symbols and broken lines) for different molecular charge states. Reprinted with permission from [34]. © 2001 The American Physical Society.

[35] on CD_4. While CD_4 is not a chiral molecule in its equilibrium geometry, the authors observed a geometry where all C–D bonds were different due to zero-point vibrations. This was termed "dynamic" chirality, in contrast to the more common "static" chirality. Although the authors were only able to measure three of the four deuterium ions as well as the carbon ion, this was sufficient information to extract the handedness of each molecule.

1.5 Laser-Initiated Dissociation

This section will describe in detail the efforts of various experimental and theoretical research groups to describe the physical processes surrounding molecular ionization and fragmentation. The structure of this review is overwhelmingly chronological with emphasis placed on emerging techniques and key findings.

1.5.1 Early work

Pioneering work in the field was done by Frasinski *et al.* [36, 37, 38, 39]. Using long, intense pulses (600 nm, 0.6 ps, 3 x 10^{15} W cm^{-2}), Codling *et al.* [36] attempted to distinguish between sequential and direct ionization using HI and

produced a molecular parent ions up to HI^{6+}. If the ionization were direct, six electrons would be rapidly removed and the H^+ ion would be separated from the I^{5+} ion by the ground-state equilibrium bond distance of 1.61 Å. In this circumstance, the Coulomb repulsion would produce protons with 45 eV of kinetic energy. In the case of a sequential ionization, the molecule would ionize as it dissociated. The final inter-ion distance would be larger and the proton energy correspondingly smaller. During the experiment, the maximum proton energy measured was 21 eV, leading to the conclusion that ionization was sequential. Furthermore, the ionization sequence $HI^{2+} \rightarrow HI^{6+}$ occurred on a timescale of $\sim$ 20 fs.

Frasinski *et al.* [37] studied nitrogen using the same laser system. They deduced the molecular charge states and kinetic energy release from a simple TOF. The authors were able to create molecular ions with charge states as high as N_2^{6+}. Using a simple Coulomb model, the ionization sequence $N_2^{2+} \rightarrow N_2^{6+}$ was determined to take $\sim$ 30 fs. The authors proposed the following sequence of events:

$$
\begin{array}{rll}
N_2 \rightarrow & [N_2^{2+}] & \rightarrow N^+ + N^+ + 7 \text{ eV} \\
& \downarrow & \\
& [N_2^{3+}] & \rightarrow N^+ + N^{2+} + 14 \text{ eV} \\
& \downarrow & \\
& [N_2^{4+}] & \rightarrow N^{2+} + N^{2+} + 25 \text{ eV} \\
& \downarrow & \\
& [N_2^{6+}] & \rightarrow N^{3+} + N^{3+} + 38 \text{ eV}
\end{array}
$$

The square brackets denote transient molecular ions and vertical arrows indicate the possibility of a particular ion ionizing again as it dissociates.

1.5.2 Covariance mapping

To better understand the multiple ionization pathways, Frasinski *et al.* [40] realized the necessity to observe correlated Coulomb explosion products with high detection efficiency. Using the original TOF design, the authors aligned the E field of their laser along the TOF axis. In this configuration, the fragment ions were ejected preferentially along the TOF axis, and a DC electric field ensured that both "forward" and "backward" ions hit the detector, with the "forward" ions arriving first. This resulted in pairs of ions seen in the time-averaged TOF spectrum of figure 1.3 along with a covariance map.

The covariance mapping technique [38] is a graphical technique of seeing correlations between all of the fragment ions. The various channels appear as separate islands on the covariance map and momentum conservation requires that correlated pairs lie along a straight line. The islands are labelled as: 1, $N_b^+ + N_f^+$ (b = backward, f = forward); 2, $N_b^+ + N_f^{2+}$; 3, $N_f^+ + N_b^{2+}$; 4, $N_b^{2+} + N_f^{2+}$; 5, $N_b^{2+} +$

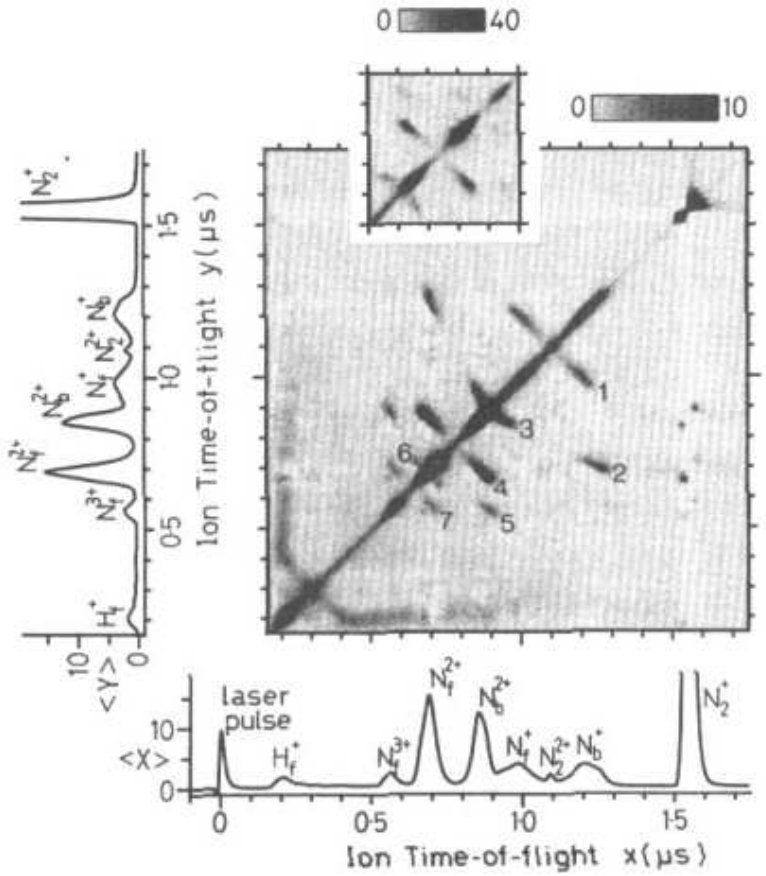

Figure 1.3: Covariance map of N_2 with the TOF spectrum placed along the x- and y-axes. Reprinted with permission from [40]. © 1989 Elsevier B.V.

N_f^{3+}; 6, $N_f^{2+} + N_b^{3+}$; 7, $N_b^{3+} + N_f^{3+}$. The power of the technique is demonstrated by considering the N_b^+ ions in islands 1 and 2. Even if the ions in these features had identical energies and would therefore be indistinguishable in a conventional TOF spectrum, a covariance map unambiguously associates the N_b^+ ions with either N_2^{2+} or N_2^{3+} molecular ions. This group would continue to apply this technique to a variety of systems including CO [41], I_2 [42] and CO_2 [43].

With improvements in laser pulse compression techniques [44] and wider use of Ti:sapphire lasers, Coulomb explosion experiments with laser pulses in the 100 fs regime became realizable by the mid-1990s. The Saclay, France group performed a number of important experiments [45, 46, 47, 48, 49, 50, 51, 52] that would verify the general applicability of laser-initiated CEI, in particular for larger molecular systems.

Cornaggia *et al.* performed a series of experiments on hydrocarbon ions, specifically, $C_2H_2^+$ [49], $C_3H_3^+$ and $C_3H_4^+$ [50] using intense laser pulses from a Ti:sapphire source (790 nm, 130 fs, 2.5 x 10^{16} W cm^{-2}). Fragment ions were collected in a Wiley-McLaren TOF [53]. The kinetic energy released was measured for a number

of different fragmentation channels and the ratio of the experimentally observed energy, E_{expt}, and the Coulomb energy from the neutral geometry, E_{Coul}, was calculated. For all ions, the ratio of E_{expt}/E_{Coul} was ∼0.53 for carbon ions and ∼0.45 for protons, regardless of the fragmentation channel that produced them. The systematically lower kinetic energies were attributed to light-induced modification of the molecular structure by physical processes as orientation along the laser electric field, bond softening and light dressed states. Coincident ion signals were analyzed using the covariance mapping technique. The absence of dissociative states such as C_2H^+ that did appear when synchrotron light was used suggested direct, instantaneous explosion of the $C_2H_2^+$ ion after removal of the electrons by the laser field. In the experiment on $C_3H_3^+$ and $C_3H_4^+$ [50], the authors again noted the near-constant kinetic energy ratio $E_{expt}/E_{Coul} \sim 0.47$ for the carbon ions. This corresponds to an observed bond length about twice the equilibrium bond length, which was in agreement with field-ionization [54] and quantum mechanical time-dependent calculations [55, 56]. Since the fragment ions were measured with a TOF, complete momentum information could not be obtained. However, by assuming a molecular skeleton with a bend angle that began at 140° and peaked at 180°, the authors were able to reconstruct the measured double-correlation map. It is important to note that this experiment only measured carbon ions. Nevertheless, it showed that the double-correlation technique (a variation of the covariance technique) could be applied to triatomic systems, although the results were open to some interpretation. In later papers, the authors would observe large amplitude bending (∼ 40°) in CO_2 accompanied by stretching [51] and straightening of the bent SO_2 molecule [52] from 119.5° in the neutral configuration to 180° as SO_2^{q+} (q=6–8) molecular ions were produced. The bend angle analysis was based upon the shape of the islands in the double-correlation map and a crude model that could be used to reproduce these island shapes.

1.5.3 Theoretical advances

As experimental techniques improved over the past 25 years, so too did the theoretical models used to describe molecular ionization. This section will describe two models developed in this time.

Enhanced ionization

The enhanced ionization (EI) at critical internuclear separation, R_c, model proposed by Posthumus *et al.* [54] was constructed to explain multielectron dissociative ionization of diatomic and triatomic molecules in intense laser fields. It was not understood why fragment ions emerging from a Coulomb explosion always appeared to have kinetic energies that were the same ratio with respect to predicted kinetic energies resulting from a Coulomb explosion in the equilibrium geometry. The observed kinetic energy ratio was always the same, even for ions of different charge states (∼ 45% for N_2, ∼ 70% for I_2) [43, 42, 48]. In the case of a diatomic, the

Coulomb energy is given by $E_e = kQ_1Q_2/R_e$, where Q_1 and Q_2 are the charges of the ions and R_e is the equilibrium interatomic distance of the neutral molecule. Two possibilities exist for a reduction in the Coulomb energy. First, screening could occur at each ionization step, effectively reducing the values of Q_1 and Q_2. Second, the molecular ion could relax to a critical distance, R_c, where subsequent ionization occurs.

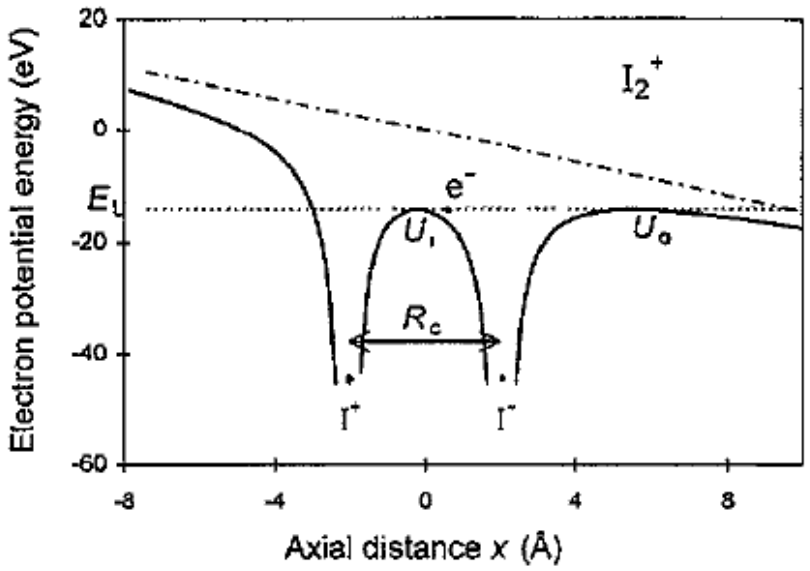

Figure 1.4: Model of I_2^+ in a laser field. The full curve represents the potential energy of the outermost electron in the combined field of two point like I^+ ions and the laser. The internuclear distance, R_c, and the field, F_c, have critical values such that the electron energy level, E_L touches both the inner potential barrier, U_i and the outer potential barrier, U_o. Reprinted with permission from [54]. © 1995 Institute of Physics and J. Posthumus.

Consider, the dissociation of the molecular ion I_2^+ on the rising edge of a laser field that is polarized along the molecular axis. The outermost electron is free to move in the double well formed by combining the remaining electrons and nuclei into two point-like atomic ions. As the ions move apart, the inner barrier rises and impedes the motion of the electron. The electron can no longer follow the field and the system makes a transition. Figure 1.4 shows the situation where the ions have moved to the critical distance and the inner potential barrier, U_i touches the electron level, E_L. In general, the double-well potential energy is given by

$$U = -\frac{Q_1}{|x + R_c/2|} - \frac{Q_2}{|x - R_c/2|} - F_c x \tag{1.2}$$

where F_c is the electric field amplitude. The position of the electron energy level in this double well can be approximated by

$$E_L \approx \frac{(-E_1 - Q_2/R_c) + (-E_2 - Q_1/R_c)}{2} \tag{1.3}$$

where E_1 and E_2 are the known ionization potentials of the atomic ions that are lowered by the Coulomb potential of the neighbouring ion, Q/R_c. This model is sometimes known as the over the barrier ionization (OBI) model and will be used in a later chapter.

As the laser field increases, the molecule will ionize again. The next electron has a much higher binding energy but since one of the atomic ions is more positively charged, the inner potential barrier is lower. To good approximation, these two effects reproduce the previous situation and the critical distance R_c is virtually unchanged. This continues through the multiple ionization process.

The authors compare their model to previously reported experimental results for N_2 [46], Cl_2 [48], O_2 [45], I_2 [42], CO [45, 41] and CO_2 [47, 43]. In general, the agreement is quite good.

A different interpretation has been proposed [55], in which the lowest unoccupied molecular orbital (LUMO) is Stark shifted by the electric field of the laser. As the molecule expands, population exchange can occur nonadiabatically between the highest occupied molecular orbital (HOMO) and LUMO. Once the LUMO is above the Coulomb barrier, ionization proceeds. Experimental studies of N_2 and I_2 [57, 58] have revealed the tendency for these molecules to ionize along asymmetric pathways. Analogous to the HOMO and LUMO in EI, the authors postulate strong coupling between $g - u$ symmetry states, as well as an internal rescattering mechanism that ionizes an inner electron and leaves the molecule in an excited state.

ADK tunnelling ionization

Unlike enhanced ionization, which can be classically described as an over the barrier model, the quasi-static theory of Ammosov, Delone and Krainov (ADK) [59] is based on the calculation of the tunnelling ionization rate in the presence of a static electric field. In this regime, the potential barrier formed by the core of the atom or molecule and the electric field of the laser becomes small enough for tunnelling to become possible. Due to a field-ionization process, the electron is "pulled off". However, there is an important difference between a static field and an oscillating field of the same magnitude. A tunnelling current will always build up in a static field. In an oscillating field, the starting tunnelling current is pushed back in the next half-cycle unless it is fast enough to reach the other side of the barrier. The ADK approximation is justified for low laser frequency when ionization occurs at a time scale that is small compared to the laser period.

For the simplest case of a hydrogen atom in its ground state, the tunnelling ionization rate in the presence of a static electric field F in atomic units is [60]

$$W_{stat}(F) = \frac{4}{F} \exp\left(-\frac{2}{3F}\right). \tag{1.4}$$

In a low frequency field $F \cos \omega t$, the ionization rate can be calculated from averaging over the static rate over half a cycle of the laser oscillation:

$$W(F) = \frac{1}{\pi}\int_{-\pi/2}^{\pi/2} \mathrm{d}\tau W_{stat}(F \cos \tau) = \frac{1}{\pi}\int_{-\pi/2}^{\pi/2} \mathrm{d}\tau \frac{4 \sec \tau}{F} \exp\left(-\frac{2 \sec \tau}{3F}\right), \tag{1.5}$$

where $\tau = \omega t$. For $F \ll 1$, this integral can be evaluated using the method of steepest descent, yielding the result [61]

$$W(F) = \sqrt{\frac{3}{\pi F}} W_{stat}(F). \tag{1.6}$$

ADK generalized this result to the case of complex atoms and ions [59], and their theory has been successful in describing atomic ionization [62, 63]. This theory has also been shown to be applicable to small molecules [64, 65, 66, 67, 68]. The ADK theory has recently been modified to include the effects of symmetry of the molecular system and the asymptotic behaviour of the molecular electronic wave function, resulting in the MO-ADK theory [69, 70, 71]. For our purpose, the simpler ADK theory, taking into account the dependence of the ionization potential of the molecule on the nuclear coordinates, suffices. The ADK tunnel ionization rate, w_{ADK}, is given in atomic units by [59]:

$$w_{ADK}(R, I) = \left(\frac{3\mathrm{e}}{\pi}\right)^{3/2} \frac{Z^2}{n^{*9/2}} \left(\frac{4\mathrm{e}Z^3}{n^{*4}F}\right)^{2n^*-3/2} \exp\left(-\frac{2Z^3}{3n^{*3}F}\right), \tag{1.7}$$

where $\mathrm{e} = 2.718\ldots$, Z is the ionic charge, and $I = (c/8\pi)F^2$ is the laser intensity. The effective quantum number, n^*, is related to I_p, the ionization potential of the system, by

$$n^* = Z/\sqrt{2I_p(R)}. \tag{1.8}$$

A particularly compelling example of the experimental applicability of ADK was seen in the work of Urbain *et al.* in 2004 [72]. The authors examined the tunnel ionization of H_2 and in so doing, challenged the assertion that the vibrational excitation of molecular ions follows the Franck-Condon principle in this regime. If the laser-molecule interaction can be described by a field-ionization process, the molecular ion will be in its electronic ground state and the vibrational wave packet will be conserved. For H_2^+, the vibrational population distribution will peak in $v' = 2$ but will also have population in higher levels as seen in figure 1.5(e).

The authors contended that the Franck-Condon principle was unable to explain the results of ionization in the tunnelling regime since the rate of tunnelling as given in 1.7 is strongly dependent upon bond length, R. Furthermore, as laser intensity increases, molecular alignment becomes ever more important. Molecules aligned parallel to the laser field will experience a non-resonant coupling effect known as bond-softening. Bond-softening has the effect of readily dissociating a vibrationally excited molecular ion. Molecules that are aligned perpendicular to the laser field are not subject to bond-softening, but do experience shifts in the vibrational excitation population distribution. As can be seen in figure 1.5(a)–(d), as laser intensity increases, the distribution of the perpendicularly aligned molecules approaches the distribution obtained with electron impact ionization (e).

1.5.4 Mass-resolved molecular imaging

The University of Tokyo group in Japan contributed a great deal of experimental work to the field in the late 1990s and early 2000s [75, 76, 77, 78, 79, 80]. The group pioneered a new technique called mass-resolved momentum imaging (MRMI) and provided a theoretical basis for molecular deformation by using a sophisticated potential energy surface dynamical model. The MRMI technique was later improved by the University College London group [81, 82] to make quantitative studies of water and carbon dioxide.

Hishikawa *et al.* studied the momentum characteristics of ionic fragments produced by CEI of N_2 [75, 76] and SO_2 [75] using intense, short pulses (795 nm, ∼50 fs, 7 x 10^{15} W cm^{-2}) and the MRMI technique. The MRMI technique utilizes a zero-order half-wave plate to rotate the laser polarization with respect to the TOF detection axis. The half-wave plate was rotated in 6° increments and 15 high-resolution TOF spectra were recorded to create the MRMI map. By construction, a symmetric MRMI pattern is expected when viewing the line connecting the 0° and 180° positions. Any indication of asymmetry suggests variation of experimental conditions during the repetitive TOF data acquisition. An example of an MRMI map for N^{2+} is shown in figure 1.6.

The MRMI technique in [75] clearly showed that the momentum of the charged atomic N^{q+} (q=1–3) fragments increased as the charge number increased. This was due to the larger kinetic energies that are released from the Coulomb explosions of highly charged parent molecular ions. Furthermore, the ejection arc of the fragments became smaller as the charge number increased. This was attributed to the N–N molecular axis being more aligned with the laser polarization. In fact, another interpretation is that for randomly aligned N_2 molecules, those molecules that are particularly well aligned with the laser field will preferentially ionize.

The fragmentation dynamics of SO_2 were then analyzed as shown in figure 1.7. The plots (a) and (b) reveal how different areas of an MRMI plot correspond to different dissociation channels. However, they also reveal a weakness of the MRMI technique. The technique is not coincident, and the fragmentation pathway cannot

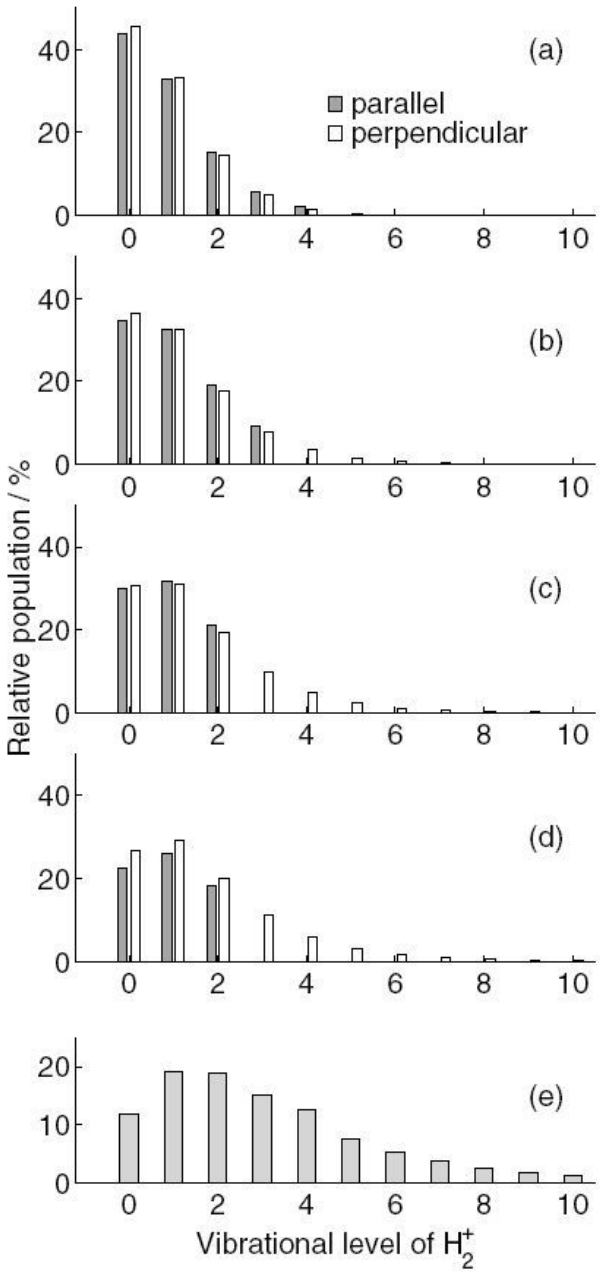

Figure 1.5: (a)–(d) Theoretically predicted vibrational excitation of H_2^+ produced by tunnelling ionization of H_2 in intense laser fields. Calculations for molecules aligned parallel and perpendicular to the laser E field are presented. The laser intensities are (a) 3.5 x 10^{13} W cm^{-2}, (b) 5.4 x 10^{13} W cm^{-2}, (c) 7.8 x 10^{13} W cm^{-2}, and (d) 1.06 x 10^{14} W cm^{-2}. The vibrational excitation of H_2^+ produced by electron impact ionization (E_0 = 10–1500 eV) of H_2 as measured by Dunn and Van Zyl [73] and interpreted by von Busch and Dunn [74] is shown in (e). Reprinted with permission from [72]. © 2004 The American Physical Society.

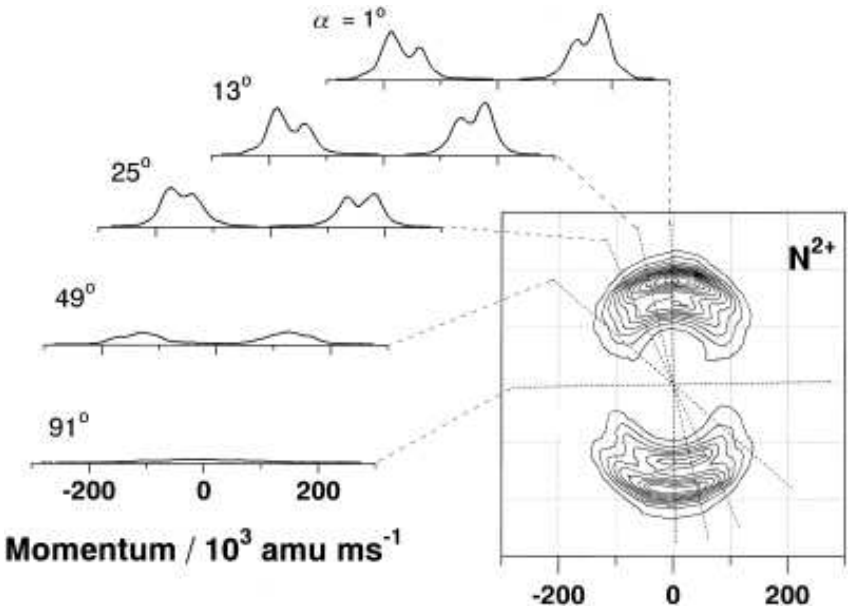

Figure 1.6: Illustration of the MRMI procedure. An MRMI map is constructed from momentum-scaled TOF spectra measured with the laser polarization at various angles α with respect to the detector axis. On the left-hand side of the MRMI map are five experimental TOF spectra of N^{2+} with angles of $\alpha = 1°$, 13°, 25°, 49°, and 91°. Each TOF spectra corresponds to the cross-section of the MRMI map at the angle α. Typically, 17 momentum-scaled TOF spectra are used to make an MRMI map. Reprinted with permission from [76]. © 1998 Elsevier B.V.

be determined with absolute confidence. In figure 1.7(c), the shape of the MRMI pattern is different that the others. The crescent patterns are in the direction perpendicular to the laser polarization. Since the molecular axis of the SO_2 molecule should be aligned with the laser polarization direction, the authors interpreted these crescents as evidence of the Coulomb explosion process occurring from a highly bent geometry. Using the MRMI maps, the authors deduced the bond angle to be $\theta = 130°$ for the (2,3,2) channel and $\theta = 110°$ for the (1,3,1) channel. Although these were close to the equilibrium value of $\theta_e = 119.5°$ for the neutral molecule, the authors admitted there were large uncertainties due to the large momentum distributions. Hishikawa *et al.* also found that the S–O bond lengths were about twice the equilibrium bond lengths, in agreement with the findings of Cornaggia *et al.* [52]. Hishikawa *et al.* provided additional experimental details in their follow-up paper [76]. Further MRMI work on CO_2^{q+} [77] and NO_2^{q+} [78] would suggest in both cases that the molecular ions became straighter as q increased and that the bond lengths stretched as q increased. The authors attempted to explain these results in terms of the light dress potential energy surfaces (LDPES). At low laser intensity, molecular ions with smaller q are formed. In this case, the authors postulated that the laser field coupled to the bending coordinate, producing a substantially bent

geometry. However, near the focal spot, higher intensities produce molecular ions with larger q values. In this case, the laser field coupled with the linear stretching coordinate. Iwamae *et al.* studied the branching ratios of NO with MRMI [79] while formalizing the detector efficiency a hitherto free parameter that had not been discussed.

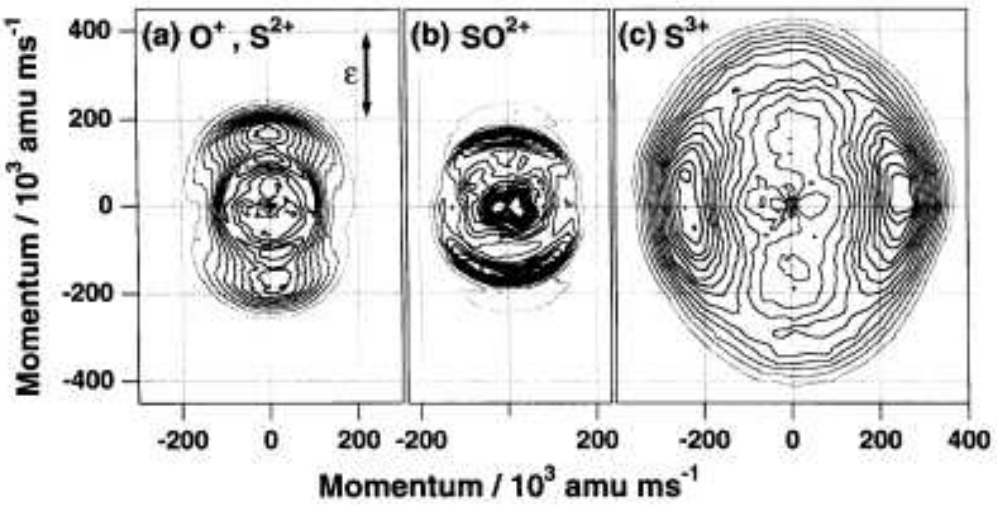

Figure 1.7: MRMI map of SO_2 with chamber pressure 1.5 x 10^{-7} Torr. The vertical arrow in (a) represents the direction of the laser polarization vector. (a) O^+ / S^{2+} channel: two pairs of crescents are visible in the polarization direction which result mostly from the three body explosion of SO_2 but are also attributed to the channels $SO_2^{2+} \rightarrow SO^+ + O^+$ and $SO_2^{3+} \rightarrow SO^{2+} + O^+$. (b) SO^{2+} channel: a pair of the crescents located in the polarization direction represent the $SO_2^{3+} \rightarrow SO^{2+} + O^+$ explosion pathway while the central region which is lower in energy is attributed to the neutral pathway $SO_2^{2+} \rightarrow SO^{2+} + O$. (c) S^{3+} channel: prominent crescents located in the direction perpendicular to the laser polarization indicate a bent molecular structure prior to Coulomb explosion. Reprinted with permission from [75]. © 1998 Elsevier B.V.

The final MRMI study done by the group was on CS_2 [80] wherein they attempted to understand the mechanisms of alignment, ionization and skeletal deformation. This study was unique in that the authors used ns-laser light pulses (1064 nm, 7 ns, 1.9 x 10^{12} W cm^{-2}) to initiate the processes of alignment and skeletal deformation. These two processes were then probed using *circularly* polarized fs pulses (795 nm, 100 fs, 5.5 x 10^{14} W cm^{-2}). In this way, the authors ensured that any alignment of the molecules was done by the ns-laser light. Furthermore, the MRMI maps were created by rotating the polarization of the ns pulses. By examining the (3,2,3) fragmentation using only the circularly polarized light, the authors found the interatomic C–S bond length to be twice the equilibrium length. The bend angle distribution was centred at 180° and had a half-width of ∼9°. However,

when the ns-pulse and fs-pulse were both used, another pattern emerged in the MRMI maps. When the fs-pulse arrived on the rising or falling edge of the ns-pulse (4 ns from the peak), the MRMI maps showed a nearly isotropic distribution, with only a very slightly larger distribution along the ns-pulse polarization direction. When the fs-pulse arrived at the peak of the ns-pulse, the S^{3+} ions were strongly aligned with the laser polarization while the C^{2+} ions were ejected perpendicular to the polarization. While the derived C–S bond lengths were nearly identical to the case where no ns-pulse was used, the bend angle distribution was substantially wider with a half-width of $\sim$15°. The authors attributed this increased bending to coupling of the $\tilde{X}^1\Sigma_g^+$ ground electronic state of CS_2 with the $\tilde{B}^1B_2$ excited state via a three-photon absorption at 1064 nm. This explanation is plausible given the equilibrium bend angle of the $\tilde{B}^1B^2$ state is 163°.

Sanderson *et al.* examined water using an improved MRMI technique [81] with intense pulses (790 nm, 50 fs, 3 x 10^{16} W cm^{-2}). Unlike previous MRMI maps, the authors recorded TOF spectra at many different polarization angles, producing MRMI maps that were much more detailed and less reliant on linear interpolation. The authors postulated that the very intense laser field was able to reorient the light H_2O molecule on a femtosecond time scale. The bent nature of the H_2O molecules was reconstructed by the MRMI maps and based on simulation, the maximum of the bend angle distribution was 130° for the (1,1,1) channel while the (1,2,1) channel had a maximum of 140° in its bend angle distribution. This change from the equilibrium bend of 104° was attributed to a single photon transition from the bent $\tilde{X}^2B_1$ ground state to the excited $\tilde{A}^2A_1$ state which has a straight equilibrium geometry. Using the same laser system, the authors performed an extensive study of CO_2 [82] using covariance and MRMI techniques. This paper was the first study of CO_2 that did not report a linear configuation. In fact, the authors pointed out that a perfectly linear configuration should never occur due to the absence of phase space at 180°. They compare their bend angle distributions to the long-pulse experiments of Cornaggia [51] and the HCI experiment of Sanderson *et al.* [31] and find better agreement with the HCI bend angle distribution. They attribute this, in part, to Cornaggia using a deliberately simple distribution for ease of calculation. Nevertheless, the authors report a peak in their bend angle distribution at 171°, somewhat less than the true equilibrium bend angle of 174.6°.

1.5.5 Image labeling

In 2001, the University of Maryland group introduced a novel technique called image labeling [83]. Described as a two-dimensional analogue of covariance mapping, this technique consists of an ultrafast laser (800 ns, 100 fs, 10^{14}–10^{16} W cm^{-2}), a TOF spectrometer equipped with imaging grade MCPs, a phosphor screen and a CCD camera. Fragment ions are accelerated toward the MCP by a DC electric field. The operating voltage on the MCPs is gated to allow the study of specific ionic species and charge states. The temporal resolution is a somewhat coarse 100 ns, but this is sufficient to separate low mass ions (H, C, N, O) into their various charge

states. Evidently, the mass resolution of this detector was quite poor. Along the laser polarization axis (shown in figure 1.8), energetic ions appear in the image at a distance from the centre given by

$$r = 2\sqrt{L\varepsilon/qF} \tag{1.9}$$

where ε is the ion's kinetic energy, q is the charge on the ion, F is the DC electric field strength and L is the distance between the focal point and the detector. The angular distribution is independent of the azimuthal angle about the polarization axis, ϕ, so equation 1.9 only holds for polar angles $\theta = 0$ and π. It is possible to deconvolve images so that equation 1.9 applies for all values of θ. In their initial paper, the authors measured the bend angle of CO_2 to be $\sim 170°$ [83].

The authors used their new technique to study the charge-symmetric fragmentation of $CO_2^{6+} \rightarrow O^{2+} + C^{2+} + O^{2+}$ [84]. Correlation images were created by selecting a C^{2+} ion (the square areas in figure 1.8) with a specific $p_\perp$. In this case $p_\parallel \equiv 0$. Frames with the specified C^{2+} ions were averaged along with the correlated O^{2+} ions. Since the ions are ejected simultaneously, momentum and energy are conserved. Therefore, $p_\parallel$ for the two groups of O^{2+} ions along the polarization axis are equal and opposite. Similarly, $p_\perp$ for the C^{2+} ion must equal the sum of the $P_\perp$ for the O^{2+} ions.

The authors examined their results in terms of the charge defect, $\sigma \equiv Z(1 - \sqrt{R_{eq}/R_c})$, where Z is the ionic charge, R_{eq} is the equilibrium bond length and R_c is the critical bond length. From their data, $R_c = 2.15$ Å and $\sigma = 0.5$. The value of R_c was nearly independent of the bend angle. This suggests that the R_c or enhanced ionization model more accurately reproduces their findings as the dynamic screening model [85, 86] predicts that σ should decrease as the bend angle decreases. Based on the measured bend angle of 145°, the authors estimate the bending level to be v=9, corresponding to about half the photon energy. This large bending motion is attributed to electron-molecule rescattering, similar to the three-step model that produces high harmonics in the strong-field regime.

While this technique is certainly novel, no other groups have adopted it as of this writing. This may be because the technique requires that bent target molecules be in a particular orientation i.e. parallel to the MCP plane. Alternatively, it may be because the results of image labeling are somewhat more ambiguous than measurements taken with a coincident ultrafast imaging technique, described in the next section.

1.5.6 Coincidence techniques

The group from the University of Tokyo performed a number of studies on CS_2 and N_2O using a device which combined a TOF with a position-sensitive detector [87, 88, 89, 90] similar to that used by Rajgara *et al.* [34]. The development of this instrument was made possible, in part, thanks to the development of new

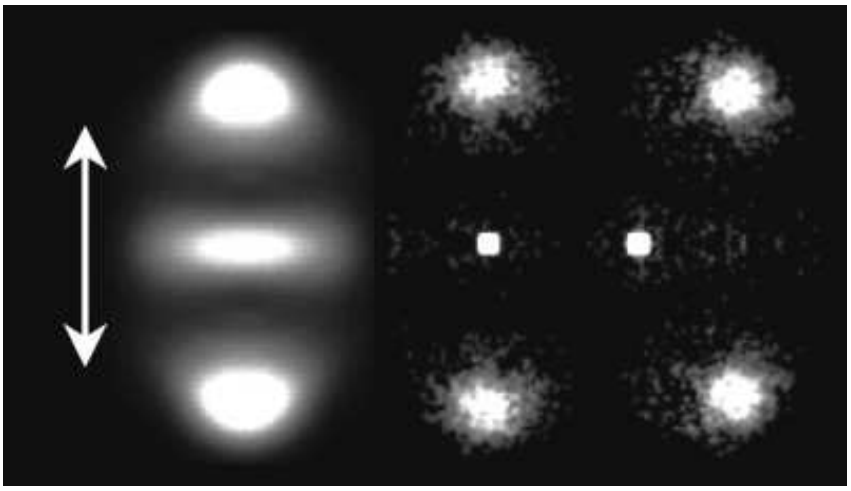

Figure 1.8: Momentum distributions of the C^{2+} and O^{2+} ions associated with the symmetric six-electron Coulomb explosion channel of CO_2: (left) average image composed of 5 x 10^5 laser shots; correlation images showing only the momenta of the three charges ejected simultaneously from a CO_2^{6+} parent that is linear and parallel to the polarization axis (centre) and bent at an angle of $\sim$161° with the molecular plane parallel to the MCP plane (right). The centre of each image corresponds to the centre of mass and the arrow indicates the laser polarization. Reprinted with permission from [84].

delay-line anode technology [91], which allowed the measurement of all fragment momenta in coincidence and the derivation of the geometry of individual molecules. The triple-coincidence technique shall be described in greater detail in the following chapter.

In the first paper by Hasegawa *et al.* [87] laser-initiated (800 nm, 60 fs, 3.6 x 10^{14} W cm^{-2}) coincidence imaging was used to study the structure of CS_2 during fragmentation. The S^+ ions in the explosion channels showed a sharp angular distribution, indicating preferential ionization of the CS_2 molecules that were aligned with the linearly polarized laser. This was in contrast with earlier, likely incorrect, studies of CS_2, which showed an isotropic distribution of S^+ ions [92]. Hasegawa *et al* postulated that the isotropic distribution of earlier studies, which did not use coincident techniques, was due to non-Coulomb explosion pathways such as the dissociation of CS_2^+. The kinetic energy release of the fragmentation was measured and although the kinetic energy spectrum has relatively low signal, the distributions clearly widen as charge state increases. An iterative, non-linear least squares fitting routine was used to reproduce the bond lengths and bend angle. These reconstructed geometries indicate that CS_2^{3+} was deformed significantly towards the bent configuration with a mean bend angle of $\langle\theta\rangle = 145°$ and standard deviation, $\sigma = 27°$, about 30° smaller than the equilibrium bend angle. Furthermore, the mean bond length was $\langle r\rangle = 2.5$ Å ($\sigma = 1.1$ Å) about 1.6 times larger than the

equilibrium bond length of 1.55 Å. It was noted that other results for CS_2^{z+} (z = 6–8) [80], determined a larger value of the bond length, showing that bond length increases with parent ion charge state.

In the second CS_2 paper [88], the authors begin a study of the sequential and concerted fragmentation dynamics. While concerted pathways have been discussed in terms of direct transitions from the neutral molecule or some intermediate, metastable molecular ion, the sequential pathway is more complicated. Typically, in a triatomic molecule, one of the ions on the end of the molecule will fragment, leaving a metastable diatomic molecular ion. This molecular ion will rotate for some time before fragmenting again. In a reaction pathway description, a concerted Coulomb explosion is written

$$CS_2^{3+} \rightarrow S^+ + C^+ + S^+ \tag{1.10}$$

while a sequential, two-step process is written

$$CS_2^{3+} \rightarrow S^+ + CS^{2+} \rightarrow S^+ + C^+ + S^+ \tag{1.11}$$

The momenta of the fragment ions can be used to describe the fragmentation as sequential or concerted. The authors defined two angles, χ and θ as

$$\chi = \cos^{-1}\left[\frac{\mathbf{p_{S_1}} - \mathbf{p_{S_2}}}{p_{S_1} - p_{S_2}} \cdot \frac{\mathbf{p_C}}{p_C}\right] \tag{1.12}$$

and

$$\theta = \cos^{-1}\left[\frac{\mathbf{p_{S_1}}}{p_{S_1}} \cdot \frac{\mathbf{p_{S_2}}}{p_{S_2}}\right] \tag{1.13}$$

As defined, the angle θ is in actuality θ_v, the angle between the momentum vectors of the S^+ fragments, whereas θ is the bend angle. The angle χ is the angle between the difference in momentum of the sulphur ions and the momentum of the carbon ion.

The χ–θ plane is shown in figure 1.9. The dense central region where $p_{S_1} \sim p_{S_2}$ and $\chi = 90°$ is the contribution from the concerted fragmentation pathway. However, in the case of a sequential process, the CS^{2+} molecular ion has a longer lifetime than its rotational period. Thus, a broad χ distribution is indicative of sequential fragmentation. The arms seen in figure 1.9 represent the contribution from the sequential pathway.

The concerted Coulomb explosion of CS_2 was discussed in [89]. The authors found that substantial structural deformation occurred on the light-dressed potential energy surfaces (PES) of CS_2^{q+} (q=0–2) where the C–S bonds stretched along the symmetric coordinate and the molecular skeleton bent substantially. These

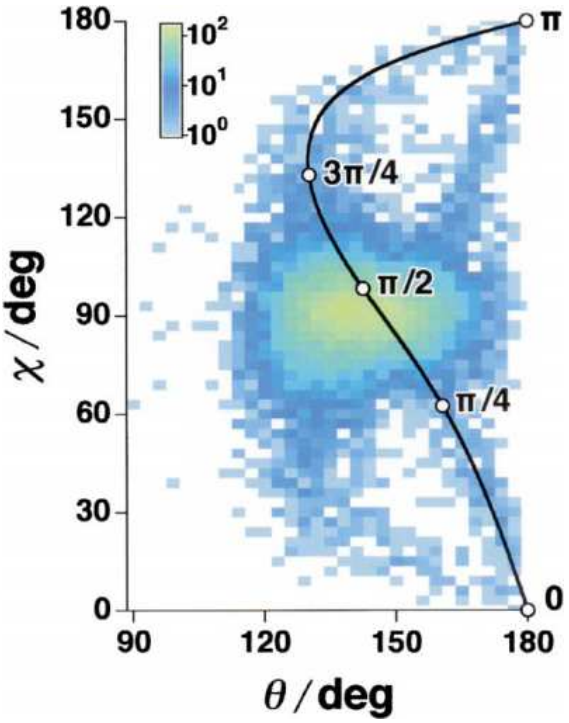

Figure 1.9: Map of the χ–θ_v correlation for the three-body Coulomb explosion of CS_2^{3+}. The two curved arms extending from the dense central region are the contribution from sequential explosion processes. The solid curve represents the theoretical χ–θ_v trajectory obtained by the classical equations of motion assuming that the second S^+ ion and the C^+ ion are ejected from the metastable CS^{2+}. The open circles are (χ, θ_v)s for the five rotational angles, $\phi = 0, \pi/4, \pi/2, 3\pi/4, \pi$, between the molecular C–S axis of CS^{2+} and p_1^{seq}. Reprinted with permission from [88]. © 2002 Elsevier B.V.

results were explained by using a model for CO_2 developed by Kono *et al.* [93, 94] which showed that the PES of CO_2^{2+} is deformed by light fields through the mixing of a large number of electronic states and opening an energetically favourable pathway along the bending coordinate.

A similar investigation was performed on N_2O^{3+} [90] in which the authors identify the N_2O dissociation pathways and observe, as above, evidence of a sequential pathway where the N–N bond dissociates first. The lifetime of the NO^{2+} molecular ion was estimated to be 0.38 ps. The N–N and N–O bonds stretched by factors between 1.34 and 1.68 while the bend angle decreased from 170° to 100°. The relationship between the stretching and bending was remarkably linear.

The National Research Council group in Ottawa, Canada performed structural studies of D_2O and SO_2 [95] using 40 fs and 8 fs laser pulses from a hollow-core fibre [96]. To generate $\sim$ 8 fs pulses, the output of a Ti:sapphire regenerative amplifier (810 nm, 40 fs, 250 μJ, 500 Hz repetition rate) was coupled into a 250

μm diameter hollow-core fibre with a length of 1 m. The hollow-core fibre was filled with argon at a pressure of 1 atm. When the 40 fs pulse entered the fibre, self-phase modulation broadened the bandwidth from 30 nm to 200 nm. Once the pulse was compressed, few-cycle pulses with a duration of 8 fs were obtained. The results of [95] are interesting for two reasons. First, by employing a few-cycle laser pulse, the authors were able to measure bond lengths shorter than predicted by the R_c model and thereby set a limit on the validity of the model. Secondly, the authors utilized *ab initio* potential energy surfaces to recover the structure of D_2O. The recovered bend angle distribution for D_2O^{4+} compared poorly to that expected from the neutral $v = 0$ stationary state. The authors attributed this to a contribution from electronic states in intermediate charge states during the multiple ionization, in effect, the same argument used by Kono *et al.* [93, 94] to describe CO_2.

1.5.7 Molecular dynamics

A molecule's dynamical nature will have a significant influence on its participation in chemical processes. If the aim is to understand and coherently control these chemical processes, the motion of a molecule must be imaged on the timescale that it occurs.

The first time-resolved approach for observation of molecular dynamics occurred in the late 1980's with the advent of time domain spectroscopy. Developed by several groups [97, 98, 99], the technique utilizes ultrashort laser pulses. Analogous to a photographic camera, an ultrashort laser pulse can be used to "freeze" a dynamical process. Time domain spectroscopy makes use of two femtosecond pulses in a "pump-probe" arrangement. The first pulse (pump) initiates some dynamical process such as vibration, rotation, etc. in the target molecule which continues until the second (probe) pulse arrives. The molecule is further excited by the probe pulse and either absorbs or emits a spectrum which can be used to infer the molecular structure. By varying the delay between the pump and probe pulses, the time evolution of the molecule's structure can be measured.

Ahmed Zewail's pioneer work on pump-probe time domain spectroscopy helped win him the 1999 Nobel Prize in Chemistry. Unfortunately, the technique requires precise knowledge of molecular potential energy surfaces, polarizabilities, dipole moments and transition dipole moments to correctly interpret a molecule's structure from the measured spectrum. Structure measurements for small molecules derived from time domain spectroscopy are typically open to interpretation while the structures of large molecules are impossible to determine.

Laser-initiated CEI combined with pump-probe provided a unique solution to the problem of measuring molecular dynamics. Much like Zewail's method, dynamics are observed by imaging a molecule's structure at different times using a pump-probe method. A femtosecond pulse is used to initiate the dynamics while a

second, delayed pulse serves as the probe pulse. The probe pulse is sufficiently intense that a Coulomb explosion occurs. By necessity, both pump and probe pulses must be as short as possible, with few-cycle pulses ($\sim$ 8 fs) typically achievable. If the pulses are much longer, the dynamics will be "blurred" in the same way that a camera with a slow shutter will produce blurred photographs of moving objects.

Numerous advances in ultrafast dynamic imaging were achieved by the National Research Council group. The system used to perform the experiments is described in some detail in [100], where the authors measured rotational wave packets in N_2, O_2 and, later, D_2 [101]. Légaré *et al* [102, 103] examined the D_2 molecule using a pump-probe technique to gain insight into the dynamics. Using few-cycle pulses with an intensity of $I = 3$ x 10^{14} W cm^{-2}, the molecule was excited to the D_2^+ $X^2\Sigma_g^+$ state. By delaying the arrival time of the probe pulse, which had intensity $I = 1$ x 10^{15} W cm^{-2}, the D_2^+ wavepacket could evolve along the $X^2\Sigma_g^+$ potential energy curve before being ionized again to the dissociative $D^+ + D^+$ curve. D_2^+ has a vibrational period of 24 fs and from simulation, the wavepacket should dephase within 60 fs. By measuring the kinetic energy release of the fragments, the interatomic distance could be calculated. By varying the pump-probe delay between 0 and 75 fs, the mean bond length was observed to oscillate between 0.9 Å and 1.6 Å. The oscillations had a vibrational period of $\sim$ 24 fs as expected and by 75 fs, the mean bond length was 1.25 Å and oscillations were no longer evident, indicating dephasing of the wavepacket.

Légaré *et al* [102, 103] studied the dynamics of SO_2 using a pump-probe technique. An 8 fs, 1 x 10^{15} W cm^{-2} pump pulse was used to create SO_2^{2+} and SO_2^{3+} molecular ions. The probe pulse, with intensity $I = 5$ x 10^{15} W cm^{-2}, was delayed in time with respect to the pump from 0 fs to 220 fs and created a charge state of SO_2^{7+}. They studied the kinetic energy release of the correlated oxygen fragments and found three features in the energy plot. The lower energy feature, where $E_{O_1} \sim E_{O_2}$, came from concerted, three-body fragmentation. The off-diagonal features, where $E_{O_1} > E_{O_2}$ or vice versa, come from sequential fragmentation. The angle, θ_v, between the O^{2+} ions indicated the presence of two concerted channels. The first, with a narrower θ_v distribution, came from the higher energy fragmentation of $SO_2^{3+} \rightarrow O^+ + S^+ + O^+$. The lower energy fragmentation of $SO_2^{2+} \rightarrow O^+ + S^+ + O$ had a wider θ_v distribution. SO_2 has an equilibrium geometry of $r_{SO} =$ 1.43 Å and $\theta = 119°$. By using few-cycle laser pulses and a 0 fs delay between pump and probe, Légaré *et al* recovered a geometry of $r_{SO} = 1.7$ Å and $\theta = 120°$ (see figure 1.10(a)). This was a significant step forward, as it showed that structural deformation due to enhanced ionization could be overcome for molecules with light atoms by employing few-cycle laser pulses. Previously, this was only possible for heavy molecules, such as I_2 [104]. The pump-probe technique allowed some investigation of symmetric and asymmetric dynamics. As seen in figure 1.10(b), 60 fs after the initiation of the asymmetric break-up of $SO_2^{2+} \rightarrow O^+ + SO^+$, $\theta \sim 70°$, $r_{SO} = 2$ Å and the distance between fragments was $\sim$ 3.7 Å. These dynamics were quite different in the three-body breakup of $SO_2^{3+} \rightarrow O^+ + S^+ + O^+$ where after 45 fs, $r_{SO} = 4.1$ Å and $\theta = 100°$, shown in figure 1.10(c).

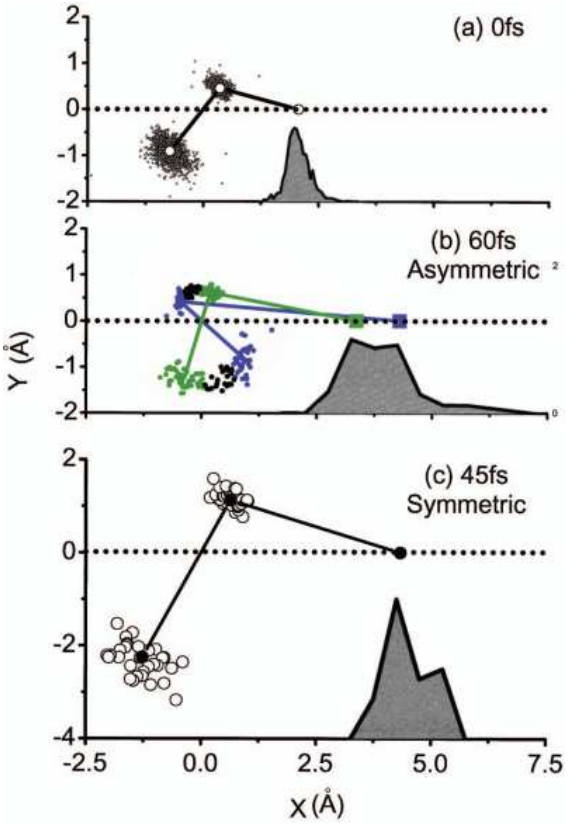

Figure 1.10: (a) Structure of SO_2 at Δt=0 fs (final charge state is $SO_2^{7+} \rightarrow O^{2+} + S^{3+} + O^{2+}$). (b) Structure of SO_2^{2+} undergoing asymmetric dissociation ($SO_2^{2+} \rightarrow SO^{+} + O^{+}$) at Δ=60 fs. Blue: average structure for bend angle $< 50°$. Green: average structure for bend angle $> 70°$ (final charge is $SO_2^{7+} \rightarrow O^{2+} + S^{3+} + O^{2+}$). (c) Structure of SO_2 in the concerted dissociation channel at Δt=45 fs (final charge is $SO_2^{10+} \rightarrow O^{3+} + S^{4+} + O^{3+}$). Reprinted with permission from [102]. © 2005 The American Physical Society.

Clearly, there have been significant achievements made in the field of molecular dynamic imaging. These observations would not have been possible without the CEI technique. The results of the National Research Council group are very encouraging, although they have yet to be repeated. Nevertheless, CEI will doubtless continue to drive progress in the study of molecular dynamics.

Chapter 2

Ultrafast Imaging Apparatus

2.1 Laser System

The multi-gigawatt femtosecond laser system used in this work was developed by Stephen J. Walker and is described in detail in his Master thesis [105]. Briefly, the Kerr lens mode-locked Ti:sapphire oscillator (Femtolasers Femtosource Scientific Pro) is pumped by a 5 W Nd:YVO_4 (Spectra-Physics Millennia, 532 nm, $M^2 < 1.1$) and produces 9.2 fs, 5 nJ, 800 nm pulses with a repetition rate of 75 MHz. Unlike a typical chirped pulse amplification scheme [106], no stretcher is used. Instead, the pulse is stretched by the transmissive optical elements in the regenerative amplifier. The regenerative amplifier consists of a Brewster-cut Ti:sapphire crystal pumped by a 20 W frequency-doubled Nd:YLF (Quantronix Falcon, 527 nm, 20 mJ, $M^2 <$ 17), two curved end mirrors, a polarizing beam splitter and a Pockels cell operating as either a quarter or half wave plate. The Pockels cell rejects the majority of the seed pulses from the oscillator and only a single seed pulse will circulate within the cavity at any given time. A seed pulse switched into the cavity will make sixteen passes through the Ti:sapphire crystal and acquires $\sim$ 400 μJ of energy before being switched out by the Pockels cell. A double prism-pair is used to compress the amplifier output and yields compressed pulses with $\sim$ 300 μJ of energy, a repetition rate of 1 kHz and a pulse duration as low as 40 fs.

2.1.1 Peak intensity

50 fs laser pulses were focused by a parabolic mirror (f = 2.1 cm, ϕ = 14 mm) located within the time-of-flight spectrometer (described in a later section). The laser power, P, is defined as:

$$P = E/t \tag{2.1}$$

where E is the energy per pulse and t is the pulse duration. Many molecular phenomena are determined by the intensity of the focused laser spot, I, defined as:

$$I = \frac{P}{A}$$

where A is the area of the focus. For a Gaussian beam, the on-axis peak intensity is given by

$$I(z) = \frac{2P}{\pi w^2(z)} \tag{2.2}$$

where $w(z)$ is the beam radius. If the minimum spot size of the incoming Gaussian beam, w_0, is located at the mirror, the spot size at the focus, w_f, is related to the focal length of the parabolic mirror, f and the wavelength of the light, λ, according to

$$w_f \cong \frac{\lambda f}{\pi w_0} \tag{2.3}$$

where we have assumed that the focal distance is large with respect to the Rayleigh range [107]. Upon substituting the parameters of our laser system into equations 2.2 and 2.3, we find the maximum intensity within the focus to be $\sim$ 2.4 x 10^{15} W cm^{-2}.

2.2 Vacuum System

The experimental apparatus is a stainless steel vacuum chamber designed and fabricated by the Science Machine Shop at the University of Waterloo (figure 2.1). The chamber is cylindrical with a height of 12", and a diameter of 6". The chamber is equipped with an 8" ConFlat top flange from which the time-of-flight mass spectrometer is suspended, two 4.5" ConFlat side flanges, and six 2.75" ConFlat flanges for view ports and instrumentation. The 4.5" and 2.75" flanges sit in two "decks". A turbomolecular pump (Pfeiffer Vacuum, TMU 071 P, 50 L/s) mounted to one of the chamber's side 4.5" ConFlat flanges evacuates the chamber to an ultimate pressure of 7 x 10^{-10} Torr. A cold cathode gauge (MKS Instruments, HPS 943) is used for pressure monitoring. The laser propagation axis passes through centre of two of the 2.75" ConFlat flanges on the lower deck. The windows are zero profile quartz (1.4" diameter, 0.125" thick). The experimental target gas is introduced effusively through a leak valve, which is attached to one of the 2.75" flanges on the lower deck. Kapton wiring in the detector limit the chamber's bake-out temperature to $\sim$ 150° C. A gas manifold is attached to the vacuum chamber to allow up to three experimental targets to be mounted to the system simultaneously.

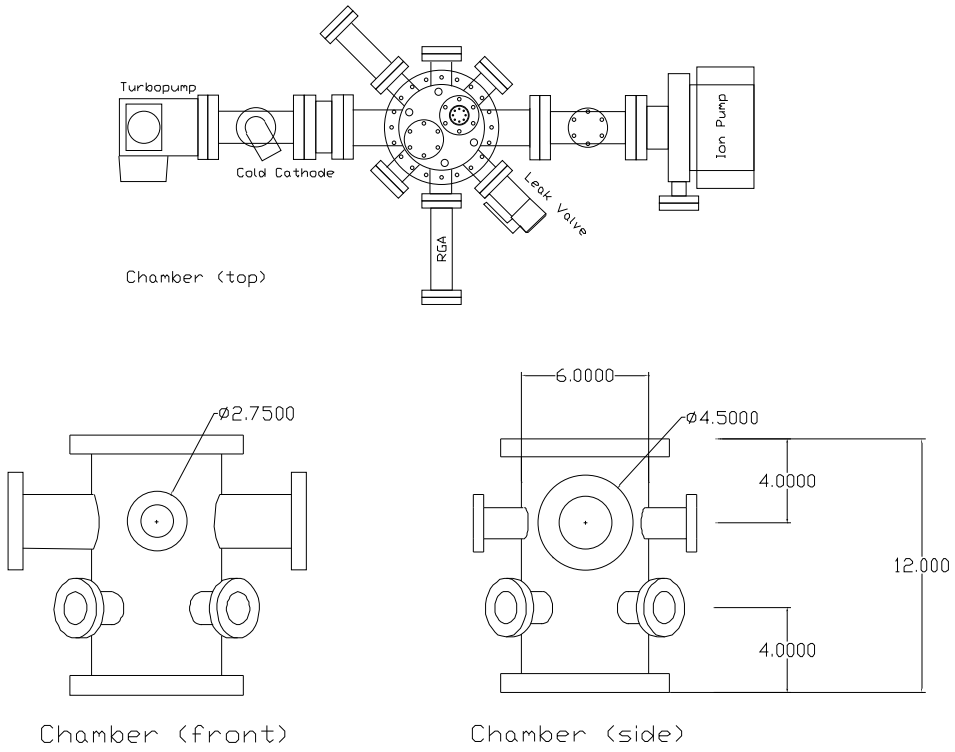

Figure 2.1: Schematic diagram of vacuum chamber. The topmost figure shows the chamber integrated into the vacuum system, with the front of the chamber pointing towards the top of the page. The lower left and lower right diagrams show only the chamber, with the upper and lower flange decks offset by 45°.

2.3 Time-of-Flight Mass Spectrometer

Laser pulses are focussed within a high-resolution time-of-flight mass spectrometer. Ions produced by laser-molecule interaction are accelerated towards the position-sensitive detector by the spectrometer's static electric field.

2.3.1 Single-stage extraction

Conventional Wiley-McLaren spectrometers include one or two acceleration regions and a field-free or "drift" region [53]. The instrument created for this work differs in that it is composed of a single acceleration region with no internal grids and no drift region. Since the ultimate goal was to produce high-quality images with the position-sensitive detector, internal grids were not employed as these tend to act as lenses, scattering ions enroute to the detector. Unlike traditional Wiley-McLaren instruments, the single-stage, no-drift design does not permit space- or

velocity-focusing of ions at the detector which is not strictly necessary. These drawbacks are mitigated by the large extraction field (up to 27000 V m^{-1}) and small laser-molecule interaction volume (about 1 μm focal spot diameter). For Xe^+ ions ($m = 2.2$ x 10^{-25} kg) or lighter, the lack of space-focusing results in a temporal width of 0.1 ns. Since the ultimate temporal resolution of the detector is 1 ns, and the typical operational resolution is 2 ns, space-focusing is irrelevant. Since our gas sample is produced from a nozzle rather than a molecular beam, the kinetic energy distribution of the target is a concern. However, as shown in the following calculation, the effect of the initial kinetic energy distribution is small.

2.3.2 Physical dimensions

Note: The majority of the machined parts of the instrument have been designed on the Imperial system. For the purpose of completeness, measurements will be presented in Imperial and S.I. units where appropriate.

The time-of-flight spectrometer (pictured in figure 2.3 with schematic shown in figure 2.4) is cylindrical with an outer diameter of 76.2 mm (ϕ 3"), an inner diameter of 55.9 mm (ϕ 2.2"). The total length is 112.3 mm. The distance from the centre of the parabolic mirror to the detector is 89.3 mm. The stack consists of 17 stainless steel ring electrodes (thickness 3.3 mm, 0.13" or 0.61 mm, 0.024") separated by teflon spacers (3.8 $\pm$ 0.2 mm). The stack is held together by four stainless steel threaded rods. The end of each rod has an additional teflon plug, a washer and two nuts. The centre of the electrode stack is held in place by a teflon mount which is connected to the detector chamber's 8" ConFlat flange with additional threaded rods. The ring electrodes have been designed to create a near-homogeneous field. The electric field uniformity was modelled using SIMION, a commercial software package.

Electrode geometry

The orientation of the electrode stack is referenced from the point of view of normal operation. Therefore, the picture in figure 2.3 is inverted according to the following description. The electrode furthest from the detector (the end plate) is a solid disk. A variation of this electrode was designed with two 6.1 mm (ϕ 0.24") holes to accommodate a lamp filament during calibration of the detector. Electrodes 2, 3 and 6–16 are identical to previously described. Electrodes 4 and 5 are not cylindrically symmetric. A 20 mm window was machined out of each ring to define the laser axis. The mount holding the parabolic mirror sits opposite this window. As the top flange of the chamber is non-rotatable, the holes for the threaded rod have been elongated to allow for an additional 5° of rotation. This additional rotation allows minor changes in the mirror orientation to ensure proper laser focussing. Each of these sixteen electrodes are fitted with a threaded rod on their edge to enable electrical biasing. The final electrode has an inner diameter of 40.1 mm (ϕ 1.58") and

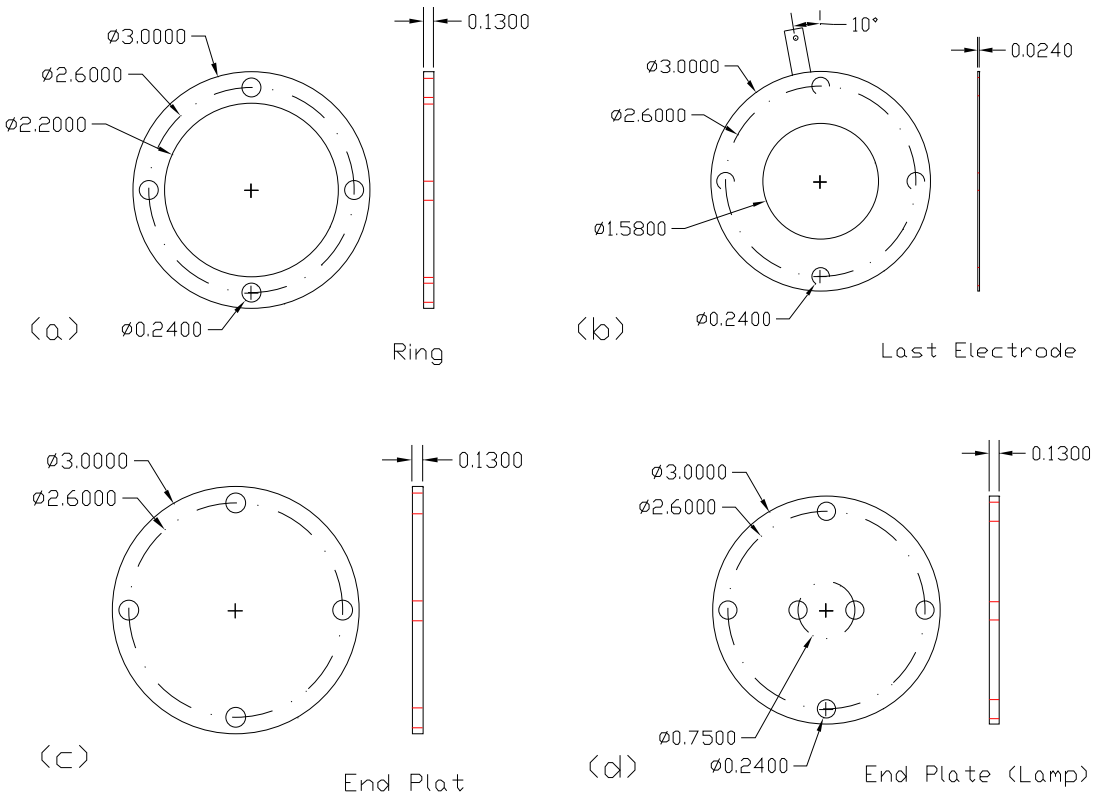

Figure 2.2: Time-of-flight mass spectrometer components. The majority of the components in the electrode stack are rings as shown in (a). The last electrode has a thickness of 0.024" and includes a tungsten mesh to ensure electric field uniformity (not shown). The end plate, shown in (c), has identical thickness to the rings. Under normal operation, (c) is used, however, a variant (d) allows for a lamp filament to be placed at the bottom of the electrode stack for use as an ion source.

a thickness of 0.61 mm (0.024"). The aperture on this electrode is covered with tungsten mesh (Unique Wire Weaving, 40 x 40 wires per inch, ϕ 0.001", 92.2% open area), which is clamped in place with a small stainless steel spacer. The design of the last, or top electrode is similar to those in the detector and it includes a tab for electrical biasing.

On-axis parabolic mirror

The on-axis parabolic mirror (aluminum-coated glass, ϕ 14 mm, 21 mm focal length) is mounted in a custom teflon holder that is attached to the fourth electrode in the stack. The metallic surface of the mirror is biased at the average potential of the fourth and fifth electrodes.

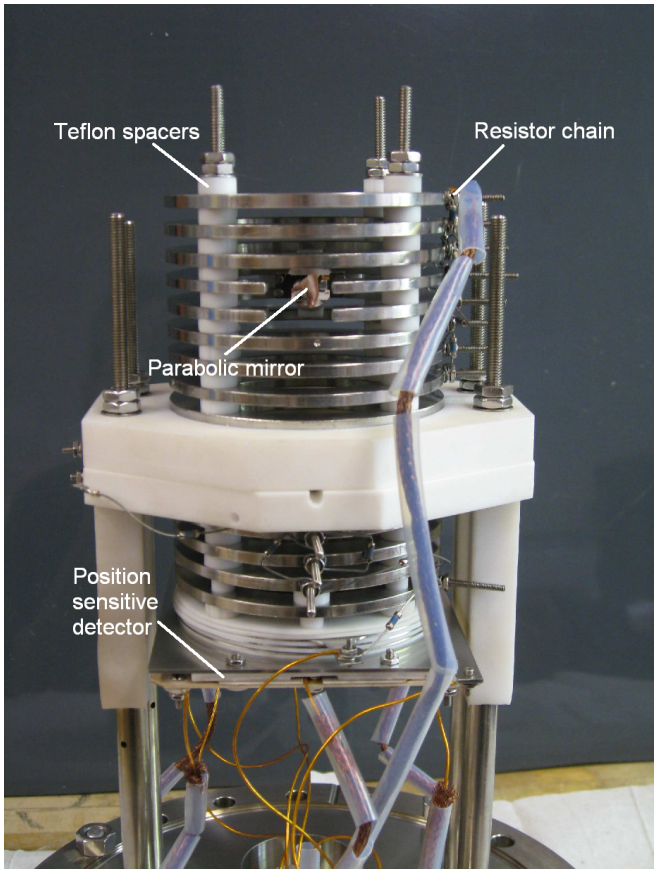

Figure 2.3: Time-of-flight mass spectrometer. The 17 electrodes are separated by teflon spacers (white areas in photograph). The electrode stack is cradled by the teflon frame. The frame is suspended from the 8" ConFlat flange by four threaded rods. The bright disk near the top is the parabolic mirror. The resistors used for electrical biasing can be seen down the right-hand side of the stack.

Electrode biasing

The electrode stack is electrically isolated to allow flexibility when biasing the spectrometer. Under typical operation when ions are collected, the bottom electrode is biased at a positive voltage while the top electrode is independently biased to a near-zero voltage. Two power supplies (Fluke model 415B) are used to generate high voltages (0–3 kV) corresponding to a maximum acceleration voltage of 270 V cm^{-1}. A uniform electric field is created by decreasing the potential of each electrode with a voltage divider network. Adjacent electrodes are connected with 2 MΩ ultrahigh vacuum-compatible resistors (Riedon Inc., 2 MΩ ± 0.5%, uncoated, P/N MF2207). Once mounted to the electrodes, as seen on the right side of figure 2.3, the entire electrode stack can be biased using only two electrical feedthroughs. The parabolic mirror, located between the fourth and fifth electrodes, is biased using resistors chained to the electrode stack. Two resistors in parallel connect the mirror to the fourth electrode and another pair of resistors in parallel connect the

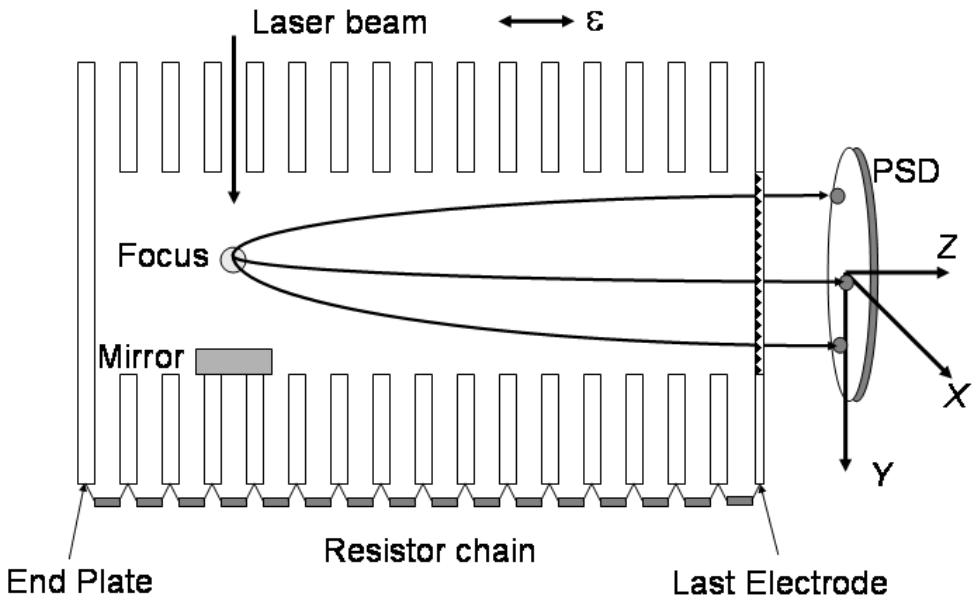

Figure 2.4: Time-of-flight mass spectrometer schematic. The laser k-vector is approximately parallel to the Y-axis in the laboratory frame. Typically, the laser polarization, ε, points along the TOF axis, Z in the laboratory frame.

mirror to the fifth electrode. Gold wire connects the resistors to front surface of the mirror. This ensures that the mirror remains biased to the average of the fourth and fifth electrodes regardless of the accelerating potential.

2.3.3 Theoretical description and ion calibration

An ion with the charge q, accelerated through a distance s by an electric field E, will obtain kinetic energy. Assuming that the initial kinetic energy is small in comparison to that obtained by the electric field (see the following section for a justification), the arrival time, t_s of the ion can be described by:

$$
\begin{aligned}
KE &= qEs \\
\frac{1}{2}mv^2 &= qEs \\
\frac{ds}{dt} &= v = \sqrt{\frac{2qEs}{m}} \\
\int_{t_0}^{t_s} dt &= \sqrt{\frac{m}{2qE}} \int_0^s \frac{ds}{\sqrt{s}} \\
t_s - t_0 &= \sqrt{\frac{2ms}{qE}} \\
t_s &= \sqrt{\frac{2ms}{qE}} + t_0 \qquad (2.4)
\end{aligned}
$$

It should be noted that equation 2.4 is not exact since there is a small gap between the top electrode and the input of the detector. However, by applying a small positive voltage to the top electrode, the homogeneous electric field can be extended to the input of the detector, even though the detector and electrode stack are electrically isolated. Therefore, s can be taken to be the distance between the focus of the parabolic mirror and the detector input ($\simeq$ 89.3 mm). The magnitude of the electric field, E, is given by V/L, where V is the accelerating voltage and L is the total length of the electrode stack, 112.3 mm.

Referring to equation 2.4, calibration of the instrument is performed by plotting the arrival time, t_s of a series of ions versus $\sqrt{m/q}$ for a known composition of gas. Typically, one will use background ions and noble gas ions, for example H_2^+, N_2^+, O_2^+, H_2O^+ and Xe^+. If the mass and charge assignments of the ions is correct, the plot will be linear with a slope of $\sqrt{E/2s}$ and an intercept of $\sqrt{E/2s}t_0$. In the case of figure 2.6, the y-axis has been plotted with m and q in natural numbers. For this reason, the slope of the graph is $\sqrt{q_0E/2m_0s}$, where q_0 is the charge on an electron and m_0 is one atomic mass unit. Similarly, the intercept is $\sqrt{q_0E/2m_0s}t_0$. The quantity t_0 is the delay between the trigger signal from the Pockels cell driver and the pump laser firing.

Based on the peak width in figure 2.5, the mass resolution of the spectrometer is $\simeq$ 125 using a sampling rate of 250 MS s^{-1}. Under typical operating conditions, a faster sampling rate of 500 MS s^{-1} is used to acquire data, giving a temporal resolution two times better than indicated here.

Justification of small initial kinetic energy

Let us assume that a singly charged carbon ion (m = 1.993 x 10^{-26} kg, e = 1.602 x 10^{-19} C) is accelerated through a distance of s = 8.93 x 10^{-2} m by an electric field E = 18000 V m^{-1}. The kinetic energy picked up by such a particle would be:

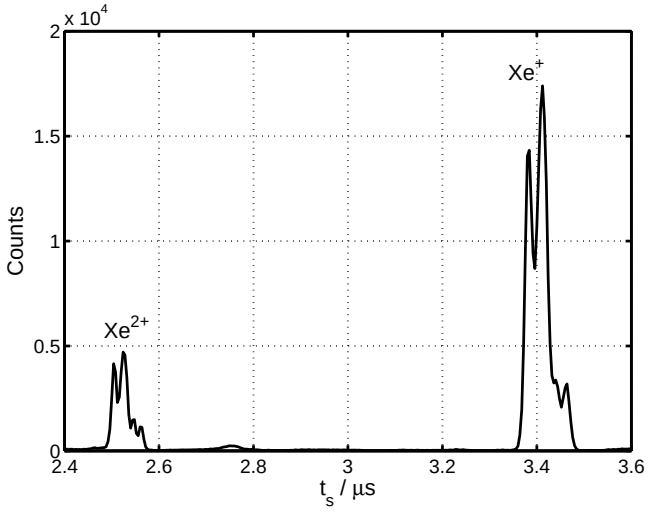

Figure 2.5: Time-of-flight spectrum for xenon isotopes with charge 2+ (first group) and charge 1+ (second group). Within each group, the peaks correspond to Xe_{129}, $Xe_{131,132}$, Xe_{134} and Xe_{136}. The relative abundances of each isotope agrees with the observed signal. The widths of the isotope peaks correspond to a mass resolution of $m/\Delta m \sim 125$.

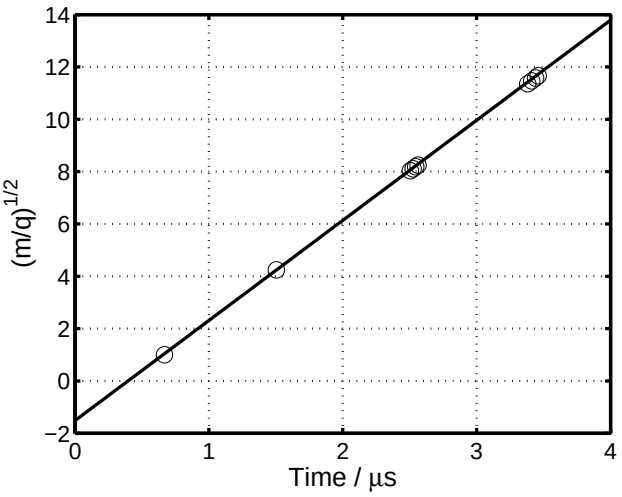

Figure 2.6: Ion calibration graph. Using isotopes of xenon, as well as hydrogen and water, the empirical scaling factor of the spectrometer can be extracted. Noting that the y-axis of this graph has been plotted in natural numbers, the slope is 3.826 x 10^6 with an intercept of -1.5145.

$$\begin{aligned} KE &= eEs \\ KE &= 2.58\,\mathrm{x}\,10^{-16}\,\mathrm{J} \end{aligned} \tag{2.5}$$

The Maxwell-Boltzmann distribution of speeds for particles of mass m, with speed v at temperature T (in Kelvin) is written:

$$f(v) = 4\pi \frac{m}{2\pi kT}^{3/2} v^2 \exp\left[\frac{-mv^2}{2kT}\right] \tag{2.6}$$

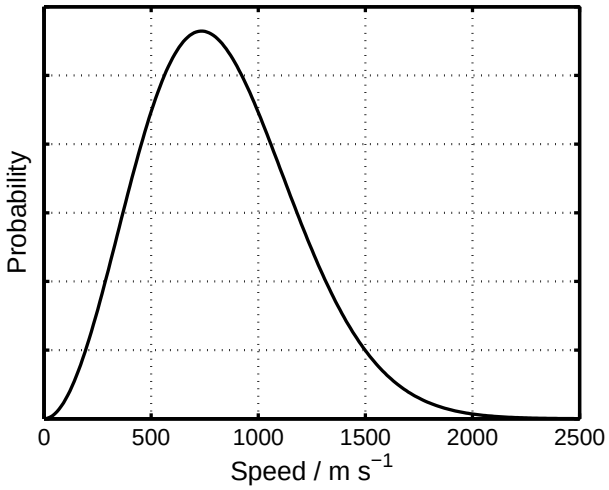

Figure 2.7: Maxwell-Boltzmann distribution for C^+ ions at 25°C. The most probable speed is 735.4 m s^{-1}.

The speed probability is plotted in figure 2.7. The most probable speed at 25°C is 735.4 m s^{-1}. This gives a kinetic energy of:

$$KE = \frac{1}{2}mv^2 \tag{2.7}$$

$$KE = 5.39\,\mathrm{x}\,10^{-21}\,\mathrm{J} \tag{2.8}$$

Thus, the thermal kinetic energy is about four orders of magnitude less than the kinetic energy imparted by the electric field. Furthermore, since the most probable speed decreases with particle mass and the kinetic energy imparted by the electric field increases with charge state, the thermal kinetic energy will become more negligible if we examine larger particles or more highly charged ions.

Another, perhaps more critical comparison, is the momentum of the fragments at the moment of explosion in comparison to the ion energies after extraction. That is, the initial momentum should satisfy, $p_z \ll \sqrt{2mqEs}$ [108]. Using the same ion

as previously described, the initial momentum must be less than $\sim$ 5 x 10^{-21} kg m s^{-1}. Generally, the observed momentum of a C^+ ion is $\sim 10^{-22}$ kg m s^{-2}.

For further reading on the theory for time-of-flight mass spectrometers and their applications, refer to [109].

2.4 Position Sensitive Detector

The position sensitive detector (PSD) in the Coulomb explosion imaging system is composed of three parts. The first part is composed of two microchannel plates (MCPs) in a chevron arrangement. The second component is the multiple backgammon weighted capacitor (MBWC) readout pad. The final part is the resistive film anode.

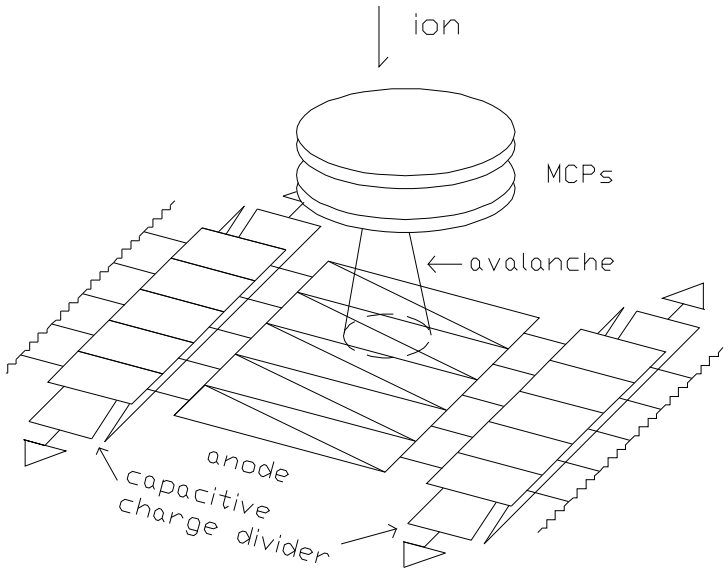

Figure 2.8: Original configuration of position-sensitive detector. The distance between the MCP output surface and the anode surface was $\sim$ 17 mm to achieve good image linearity. Figure adapted from [110].

2.4.1 Microchannel plates

A microchannel plate (MCP) is an electron multiplier usually used for detecting X-rays, ultraviolet radiation and charged particles. The output is a two-dimensional electron image that preserves the spatial resolution of the original input radiation, but with a linear gain of up to 10^3. Two MCPs may be arranged in a chevron configuration to give a high gain of 10^6. Combined with an appropriate position readout technique, the location of particles can be determined.

Each plate consists of an array of tiny glass tubes fused together to form a thin disc. Both faces of the disc are metallized to provide parallel electrical connections to all channels. In a vacuum, and with a potential difference of 800 V $\sim$ 1400 V across the plate, each channel becomes a continuous dynode electron multiplier, operating on the same principle of electron avalanche as the single-channel electron multiplier.

The MCPs (part number G12-46DT/13/E/A, channel diameter 12μm, plate size ϕ 46 mm, aspect ratio 80:1, bias angle 13°, engineering grade, resistance 177 MΩ) for the PSD were purchased from Photonis Imaging Sensors. They are resistance matched.

2.4.2 Modified backgammon technique with weighted capacitors readout pad

To perform position readout measurements, one must use MCPs in conjunction with a position sensitive anode. To date, a number of position sensitive anodes have been developed, including resistive anodes [111], delay lines [112], crossed-wire detectors [28] and wedge-and-strip anodes [113]. The latter three types are used if high temporal resolution is required. The best temporal and positional resolutions attained by the delay-line method are reported to be 0.6 ns and 30 μm, respectively.

In 1992, Mizogawa *et al.* reported a new anode described as the "modified backgammon method with weighted capacitors" (MBWC) anode [27]. The MBWC anode is based on two previous techniques, the weighted coupling capacitors (WCC) method [114, 115] and the backgammon method [116]. Our MBWC anode is based on Mizogawa's design and was acquired from Tokyo Metropolitan University. Commercial anodes are distributed through Optima Corporation.

Backgammon method

The backgammon method is a well-known one-dimensional position-readout technique. The anode of a MCP-based charged-particle detector is divided into two regions by a zigzag insulating line, shown in figure 2.9. The pitch of the zigzag is 2–3 mm, creating two groups of many sharp wedges, the tips of which are pointed left for one group and right for the other. An incoming particle will interact with the MCPs, creating a charge cloud. This charge cloud falls onto the plane and covers several repetitions of the zigzag, separating into two charge fractions (right, or Q_R, and left, or Q_L). The ratio of this geometrical charge separation depends on the position of the charge cloud centroid in a linear fashion. Therefore, the two charge signals provide one-dimensional position information.

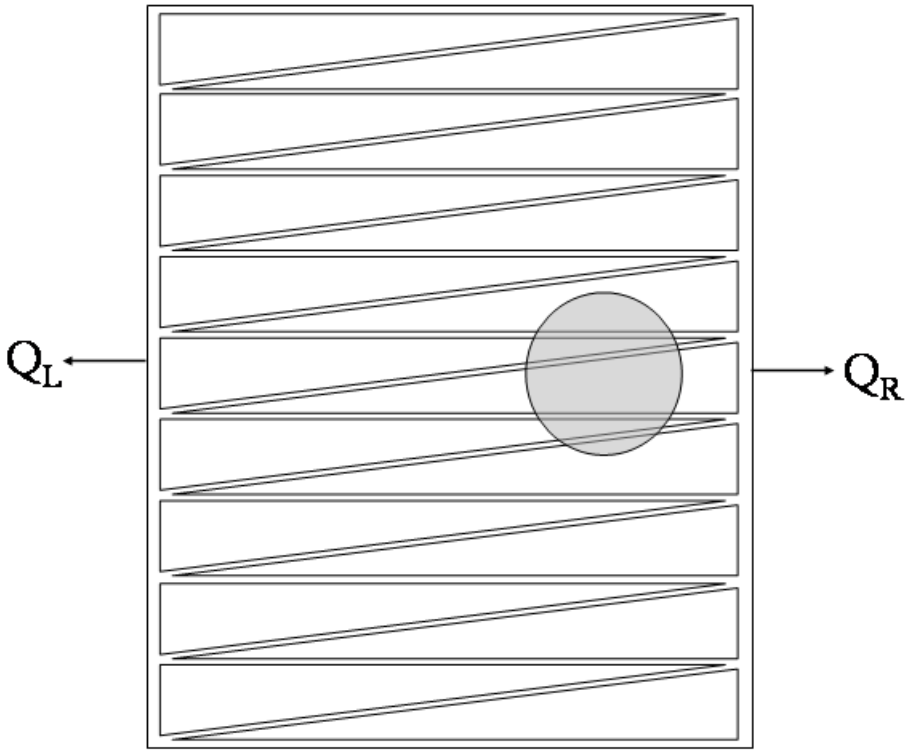

Figure 2.9: Schematic of one-dimensional backgammon method. The electron cloud falls on the zigzag pattern and splits into two, Q_L and Q_R. The position of the centroid of the electron cloud, as measured from the left edge of the anode, would be $Q_R/(Q_R + Q_L)$.

Two-dimensional position readout

The backgammon method can be modified to provide two-dimensional position information. Mizogawa *et al.* [27] adopted the WCC method [114], creating the combined two-dimensional technique the modified backgammon method with weighted coupled capacitors (MBWC), as shown in figure 2.8. The use of appropriate readout electrodes coupled by capacitance allows the pattern printed on the anode to be a simple iteration of the wedges. The result is good imaging linearity and very high positional resolution in most of the active area of the MCP. Under ideal conditions, one can resolve the capillaries of the MCP, providing an unmatched spatial resolution of 10∼15 μm [110] and has been used in a variety of Coulomb explosion experiments [117, 32, 31, 35, 33, 34].

Drawbacks of MBWC method

To achieve high positional resolution, the gap between the MCP output and the MBWC input surface should optimally be 15–17 mm. This gap is necessary because the electron avalanche from the MCP should be expanded to a size such that it hits several wedges. If the electron cloud were smaller than a single wedge, the resolution would not exceed the size of that wedge and a two-dimensional position determination becomes impossible.

Since an electric field is necessary between the MCP output and the MBWC input, the user must ensure that electrostatic lensing does not perturb electron trajectories. Lensing can be minimized by inserting rings or meshes, but this complicates the instrument setup.

Magnetic fields perpendicular to the MCP plane will cause electrons to travel in a cyclotron motion, preventing the cloud from expanding. Furthermore, a magnetic field parallel to the MCP plane substantially distorts and rotates the image. Therefore, the MBWC is unusable in a magnetic field.

Finally, the MBWC anode must be carefully handled at high voltages. In typical electron detection conditions, 2–3 kV is applied to the MCP output and the MBWC anode potential should be even higher. Discharge must therefore be considered during the detector design.

2.4.3 Resistive film anode

The resistive film anode purchased from Optima Corporation is made of ceramic (96% alumina), and the resistive film consists of RuO_{2-}/glass surrounded by a Pd/Ag electrode. The diameter of the film is 73 mm and the resistance is 10 MΩ between the periphery. The mounting holes are separated by 40 mm in the x-direction and 80 mm in the y-direction, identical to the MBWC anode. As reported in [118], optimal performance of anode was achieved when a 3 mm gap separated the film and MCPs, as shown in figure 2.10. In our detector, this optimal distance was achieved by inserting a teflon spacer between the MCP Back electrode and the insulating plate. Under these conditions, Veshapidze *et al.* [118] report a position resolution of ≈ 0.3 mm when using 40 mm MCPs.

The insulator plate is designed to connect to the MWBC anode such that the back side of the insulator plate touches the front of the MBWC surface. An electron avalanche from the MCPs hits the resistive layer and then dissipates through the electrode of the resistive layer. Therefore, electrons never reach the MBWC anode. Instead, the MBWC senses the image charge, induced by the electron avalanche sitting on the resistive film [119].

As noted, the MBWC anode can operate without the resistive film so long as one takes steps to avoid electrostatic lensing and magnetic field interaction. By adding the resistive film plate to the PSD, one can overcome these drawbacks and simultaneously construct a much more compact device.

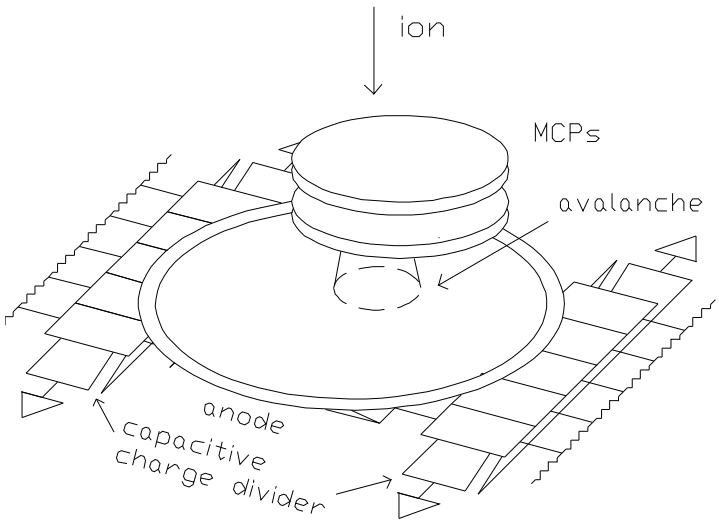

Figure 2.10: Modified configuration of position-sensitive detector. The distance between the MCP output surface and the anode surface was 3 mm to achieve good image linearity.

2.5 Data Capture

The four output signals from the readout pads of the MBWC are connected to BNC connectors on the 8" top flange of the experimental chamber. The output signals are amplified by preamplifiers and fed to the PC oscilloscope cards. Once acquired, the data is stored on the hard disk and analysed by software.

2.5.1 Pre-amplifiers

The pre-amplifiers (Ortec Model 142B) used in the system have two outputs, energy (**E**) and timing (**T**). Only the energy output is used, so the timing output must be terminated in 50 Ω for optimal performance. The energy output signal from the pre-amplifier is a fast-rise-time voltage step with an exponential return to the baseline. The timescale of this return is $\sim$ 1 ms. The polarity of these output pulses is inverted from the signal polarity at the detector output. In our case, the positive bias polarity is used for the detector, thus the **E** output of the preamplifier is positive.

2.5.2 Gage oscilloscope cards

Data capture is performed by the PC oscilloscope cards (Gage CS82G), purchased from Gage Applied Inc. Two cards are linked in a master-slave arrangement such that signals from four channels can be captured simultaneously. Data is acquired

for each shot of the laser system, which has a repetition rate of 1 kHz. Once triggered by the Pockels cell driver, the PC cards will acquire data, 10-bit in time and 8-bit in voltage. Typically, the sampling rate is set to 500 MS/s, giving a total acquisition time of just over 2 μs and a temporal resolution of 2 ns.

Since all raw data is saved for each acquisition, a large amount of storage space is required. In fact, 4 MB of data are generated each second, and a typical 25 minute data run consumes $\sim$ 5 GB. Once data has been acquired, it is filtered and analysed to conserve hard disk space.

2.5.3 Event identification, ion impact time and position

Signals are read from the four outputs of the detector are recorded by the Gage boards as digitized traces with 10 bits of horizontal (time) resolution and 8 bits of vertical (voltage) resolution. The four outputs are described in terms of a Cartesian representation of the detector. The connections between detector outputs and Gage board inputs are given in table **??**.

Output	Board	Channel
I_{xy}	1	A
$I_{x\overline{y}}$	1	B
$I_{\overline{x}y}$	2	A
$I_{\overline{xy}}$	2	B

Table 2.1: Detector outputs and Gage board inputs. Note that for entries in the first column, the notation $\overline{x}$ indicates the output in the negative x-direction.

Figure 2.11 shows a typical signal trace from the four channels of the detector. Ion impacts are indicated by large steps in the detector signal.

Although the total vertical resolution is 8-bits, the signal height of a typical event ranges between 10$\sim$80. For a given event, the position (x_0, y_0) is given by

$$x_0 = \frac{I_{xy} + I_{x\overline{y}}}{\sum I} \tag{2.9}$$

$$y_0 = \frac{I_{xy} + I_{\overline{x}y}}{\sum I} \tag{2.10}$$

where

$$\sum I = I_{xy} + I_{x\overline{y}} + I_{\overline{x}y} + I_{\overline{xy}} \tag{2.11}$$

Equations 2.9 and 2.10 will give the position of an ion in arbitrary units. That is, the scaling of the voltages will return x_0 and y_0 values in the range of 0 to 1.

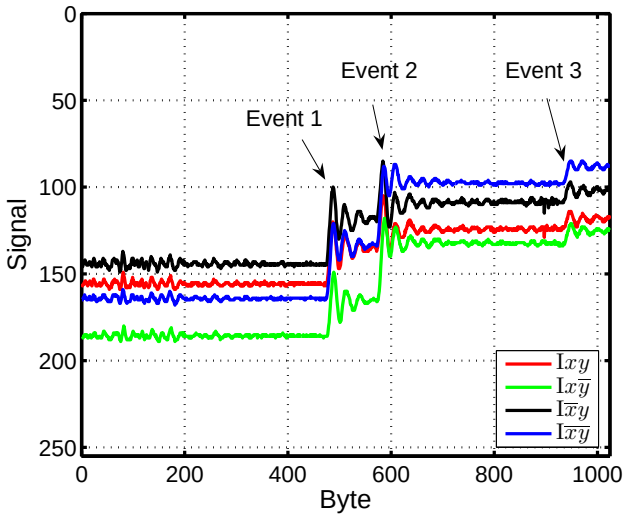

Figure 2.11: Triple event signal. The four channels indicated are: Ixy (red), I$x\overline{y}$ (green), I$\overline{x}y$ (black), and I$\overline{xy}$ (blue). Three events can be seen in the signal, located at byte positions $\sim$ 500, 590 and 925.

The positions corresponding to the events shown in figure 2.11 are shown in figure 2.12. To convert these arbitrary units into physical units, a calibration procedure was performed.

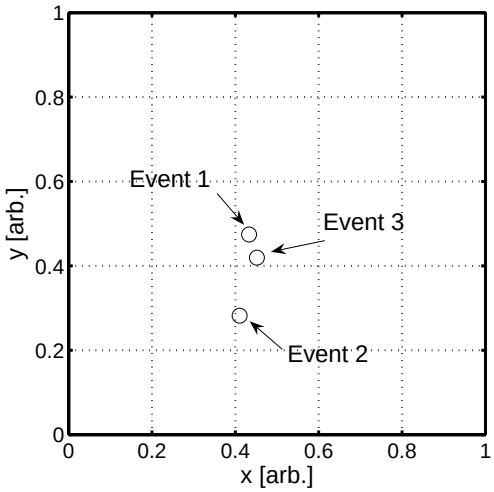

Figure 2.12: Recovered ion positions. These positions are calculated in arbitrary units by equations 2.9, 2.10 and 2.11. To convert the arbitrary positions into real units, a conversion factor must be used.

2.5.4 Detector calibration

Once the detector was installed, calibration was performed using a tungsten lamp filament mounted on the bottom plate of the electrode stack. The filament acted as an ion source independent of the laser and gas target.

A stainless steel mask (see figure 2.13) was mounted in front of the MCP input on the detector. The mask consisted of a regular array of ϕ 0.25 mm, ϕ 0.5 mm, and ϕ 1 mm holes. The centres of the holes were separated by 5 mm. The axis of the array is offset from the $x - y$ axis of the detector by 10°.

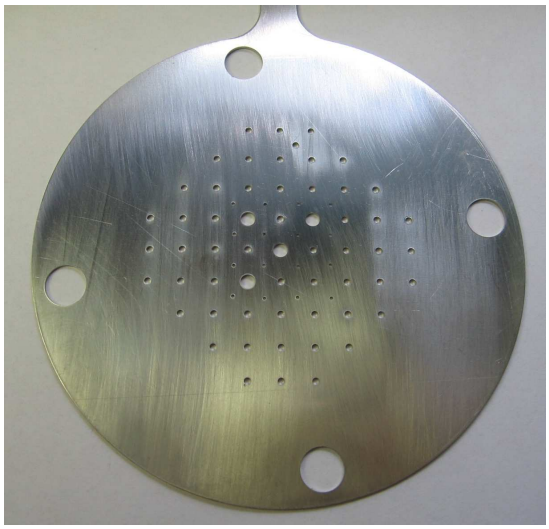

Figure 2.13: Calibration mask. The mask consists of a regular array of ϕ 0.25 mm, ϕ 0.5 mm, and ϕ 1 mm holes. The centres of the holes were separated by 5 mm. The array was offset from the $x - y$ axis of the detector by an angle of 10°. The mask was not four-fold symmetric. One of the holes near the centre of the mask was made smaller than the others to assist with identifying the orientation.

Approximately 10^6 ion events were used to reproduce the mask geometry, shown in figure 2.14. The recovered hole positions were matched to the known mask geometry by employing a series of linear transformations (see following section). The numerical values of the matrix elements used in the stretch and shear matrix were obtained by fitting the two data sets with a least squares fitting routine.

Refer to Appendix A for the algorithm used for geometry correction based on the calibration above.

2.5.5 Frames of reference

Two frames of reference are important in an ultrafast imaging system. The first is the laboratory frame (X, Y, Z) where measurements are made. The second is the molecular frame (x, y, z) where structure and dynamics are viewed.

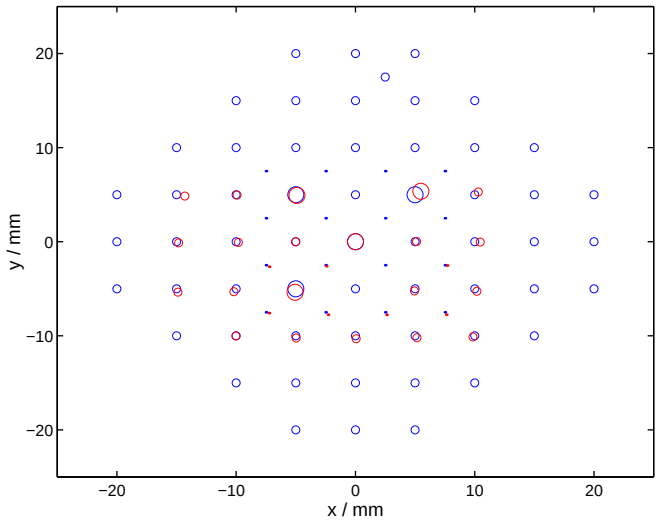

Figure 2.14: Recovered calibration mask. The blue dots and holes correspond to the machined mask geometry. The red dots and mask correspond to the recovered geometry once the calibration factor has been included. A micromesh, accompanied by a more complicated algorithm could also be used to calibrate a detector.

The laboratory axes correspond to the natural axes of the spectrometer and detector. The detector has an $x-$ and $y-$axis, as indicated in the proceeding section. These are the X- and Y-axes in the laboratory frame. The Z-axis is the flight axis of the spectrometer. The origin of the laboratory frame is directly below the geometric centre of the detector, level with the laser focus. While convenient, it is not necessary for the laser focus to be located beneath the centre of the detector. The X- and Y-coordinates of the laser focus can be determined by singly ionizing a background gas within the chamber. The centre of the ion impact distribution corresponds to the coordinates of the laser focus. The measurement was performed using nitrogen gas (N_2^+) and, as indicated by figure 2.15, show the focal coordinates at (-2.4 mm,-4.9 mm).

In order to calculate momentum values in the molecular frame, the spatial origins (X_0,Y_0) must be determined for each applicable species of ion. A robust algorithm was employed to make precise determination of the spatial origins. Using figure 2.15 as an example, the number of ion impacts are histogrammed as a function of the X- and Y-coordinates to produce $H(X)$ and $H(Y)$. A nonlinear fitness function is evaluated for each coordinate using the histogram. The fitness function is:

$$A(X) = \sum_{\delta=-20}^{20} H(X+\delta)H(X-\delta) \tag{2.12}$$

The functions $H(X)$, $A(X)$, $H(Y)$ and $A(Y)$ are plotted in figure 2.16. Note that $A(X)$ and $A(Y)$ are not designed to recreate the width of $H(X)$ or $H(Y)$,

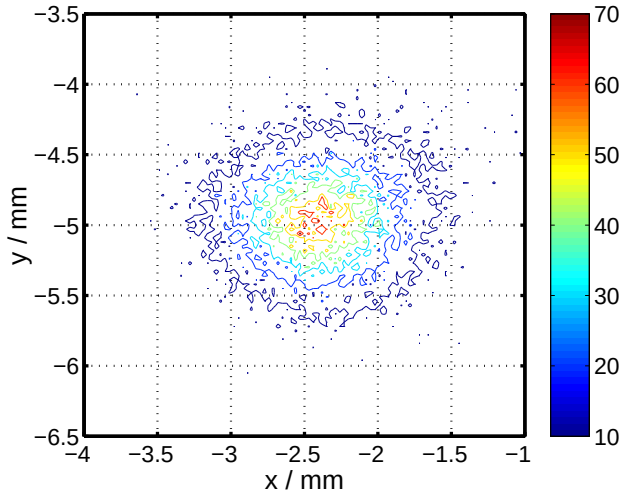

Figure 2.15: Spatial origin of nitrogen gas. The ion impact distribution resulting from N_2^+ is shown. Since the mean velocity of the background gas is zero, the centre of the distribution (-2.4 mm,-4.9 mm) is located above the laser focus.

but will simply find the peak value. This example used simple histograms, but the algorithm in equation 2.12 will also find the maximum value for double-peaked histograms, which would result from using linearly polarized light with its polarization vector parallel to the detector plane.

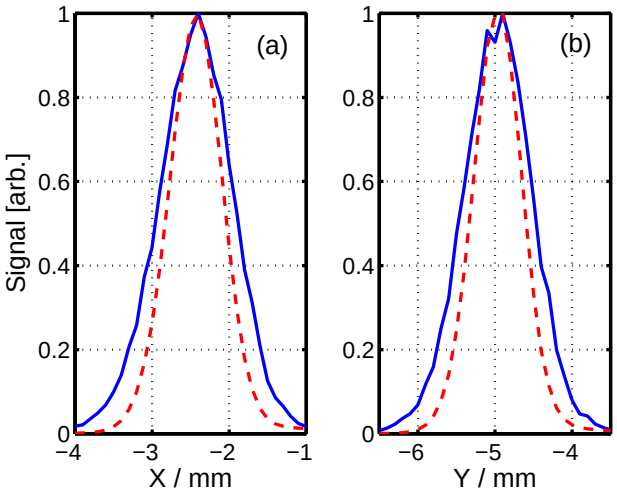

Figure 2.16: Spatial origin determination. Histograms of the $X-$ and $Y-$positions for N_2^+ ions are shown in (a) and (b) respectively (blue, solid line) along with the calculated $A(X)$ and $A(Y)$ (red, broken line). The spatial origin (-2.4 mm, -4.9 mm) corresponds to the peak positions of $A(X)$ and $A(Y)$.

2.5.6 Three-dimensional momentum determination

The ability to determine three-dimensional fragment momenta is essential for ultrafast imaging. Measured in the laboratory frame, (X, Y, Z), the ion momentum components immediately following ionization are given by:

$$\begin{aligned} p_X &= m\frac{(X - X_0)}{t} \\ p_Y &= m\frac{(Y - Y_0)}{t} \\ p_Z &= \frac{qE}{2}\frac{(t_0^2 - t^2)}{t} \end{aligned} \tag{2.13}$$

In equations 2.13, m is the fragment mass, (X, Y) is the ion impact position in the laboratory frame, (X_0, Y_0) is the ion-dependent spatial origin, t is the flight time, E is the electric field, q is the charge and t_0 is the arrival time for a zero-kinetic energy ion with the same m/q ratio determined via mass calibration of the time-of-flight spectrum.

Fragment momentum calibration

To establish the uniformity of the electric field, nitrogen gas was multiply ionized using linearly polarized laser pulses. Since the nitrogen molecules were not aligned prior to ionization, only molecules that were initially aligned with the electric field of the laser would ionize. The linearly polarized beam was rotated with a half-wave plate in 10° increments. At each position, approximately 10^6 uncorrelated ion impacts were recorded and their momentum was calculated according to 2.13. We can define a new coordinate system, (X', Y', Z), where the laser beam propagation axis was in the $Y'-$direction, while the polarization was rotated in the $X'-Z$ plane. Recalling that X and Y are defined as the axes of the detector, the angle between the X and X' axis is θ, while the angle between Y and Y' is ϕ. Two-dimensional histograms of the fragment momenta were computed, normalized and summed to produce figure 2.17. The general shape of the plots is as expected. If $\theta = \phi = 0°$, the p_X vs. p_Y plots should be a horizontal line, while the p_X vs. p_Z plots should be a circle and the plots of p_Y vs. p_Z should be a vertical line. From the shape of figure 2.17(g), the angle θ is approximately 14°, while from figure 2.17, the angle ϕ is approximately 3°.

2.6 Data Processing and Analysis

This section outlines data analysis algorithms common to all experiments with the apparatus. These algorithms include (a) identifying triple coincidences, (b)

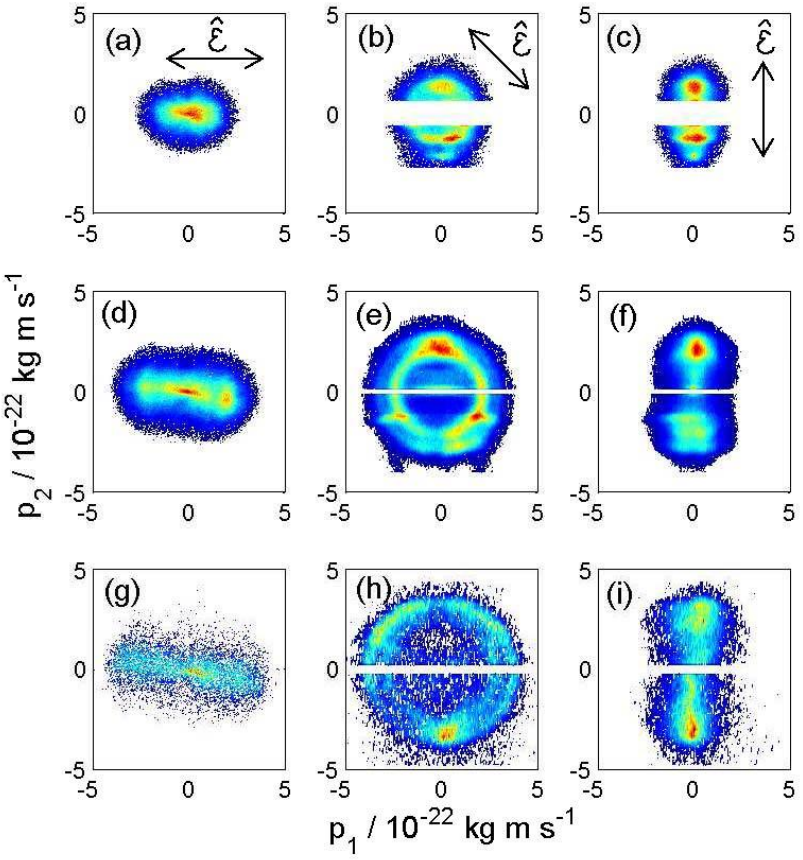

Figure 2.17: Nitrogen momentum component distribution. Different charge states and momentum components are plotted in each figure. N^+ is plotted in (a)–(c), with p_Y vs. p_X in (a), p_Z vs. p_X in (b) and p_Z vs. p_Y in (c). Similarly, (d)–(f) plots the momentum components of N^{2+} fragments while the momentum components of the N^{3+} fragments are plotted in (g)–(i). The 14° tilt that is evident in the p_Y vs. p_X plots is due to the rotation of the laser-mirror axis with respect to the $X-Y$ axis of the detector. The 3° tilt in the p_Z vs. p_Y plots is due to the laser not being perfectly parallel with the plane of the detector. These tilts can be removed with software during processing. Horizontal white areas in the plots cannot be measured in coincidence due to the dead time of the detector.

identifying ion mass and charge, (c) transforming ion impact data into the three-dimensional momentum information. Specialized software has been developed to facilitate the collection and analysis of all data from the instrument.

2.6.1 Correlated ion events

Correlated events are those in which two or more events are detected for a single laser shot. In the case of triatomic molecules, three events must be detected to reconstruct the geometry. Given the ultimate detector efficiency of 50% per event, the probability of collecting all fragments from the Coulomb explosion of a triatomic molecule is, at best, 12.5%. Uncorrelated ion events, which may arise from metastable ions, impurities such as water, and Coulomb explosions where not all fragments are detected are ignored at this stage. Approximately 5% of all laser shots produce a triple coincidence event.

Locating correlated ion events

The raw data from the Gage cards is recorded onto the PC hard disk in the proprietary .SIG file format using the "gagescan" program. Once a 30-minute data run is completed, the raw data must be filtered to locate the time of ion impacts. "FindEvent" program was written to perform high-speed filtering and analysis of the raw data files. The algorithm used for filtering data is given in Appendix A.

2.6.2 Fragmentation channel and momentum

Once correlated triple events have been identified, it is necessary to determine the fragmentation channel and the momentum of each of the fragments.

Determining fragmentation channel

For a given correlated triple event, the fragmentation channel can be deduced from the arrival times of the three fragment ions. If the arrival times of the fragment ions are well separated ($\sim$100 ns, the dead time that arises from post-event ripples in the voltage signal), the fragmentation channel can be deduced directly. However, for highly charged ions with large kinetic energy, it is common for the arrival times of several species to be quite close to one another. In the time-of-flight spectrum, this produces peaks which will partially overlap. Therefore, a general technique was developed to account for ambiguous correlated triple events.

For each arrival time in the triple event, fragments ions that could arrive at that time are identified. Permutations of possible fragments are created and any nonphysical permutations are removed. For example, if the molecule CS_2 was under investigation, there must be exactly one carbon fragment and two sulphur fragments

for a permutation to be physical. If the molecule is aligned along the axis of the time-of-flight spectrometer, a further constraint can be imposed. When a linear molecule such as CS_2 explodes, one of the sulphur fragments will be pointing in the direction of the detector while the other will point in the opposite direction. If both sulphur ions have the same charge, one will arrive first and this is known as the "forwards" ion. The other sulphur ion must be turned around by the DC electric field and will arrive later. Therefore, the second sulphur ion is known as the "backwards" ion. We make use of this "forwards-backwards" condition to set a further constraint to the identification algorithm. That is, each triple event must consist of exactly one carbon ion, one forwards sulphur ion and one backwards sulphur ion.

This algorithm will typically produce one or two physical fragmentation channels for each triple event. If more than one possibility is generated, false events will be eliminated once the fragment momentum is calculated.

Calculating momentum vector components

With the fragmentation channel determined, the masses, m_i, and charges, q_i, of each ion are known. The flight times, t_i, and positions, (x_i, y_i), are known directly from the detector. Combined with the flight time, t_0, and position, (x_0, y_0), of an ion with zero initial kinetic energy, the initial momenta for the ith fragment can be calculated according to:

$$p_{xi} = m_i \frac{(x_i - x_{0i})}{t_i} \tag{2.14}$$

$$p_{yi} = m_i \frac{(y_i - y_{0i})}{t_i} \tag{2.15}$$

$$p_{zi} = \frac{qE}{2} \frac{(t_{0i}^2 - t_i^2)}{t_i} \tag{2.16}$$

Note that just like t_0, (x_0, y_0) are ion-specific. Refer to the earlier calibration section for details.

2.6.3 Geometry reconstruction

Once the asymptotic momentum vectors have been identified for a particular explosion channel, the molecular geometry just after the Coulomb explosion can be calculated. In this case, we refer to the molecule's internal geometry and no longer consider the orientation of the molecule with respect to the laboratory frame. In practice, the laser polarization points along the Z-axis, and randomly oriented molecules that are aligned with the laser field will preferentially ionize. The general procedure for geometry reconstruction is described by the following steps:

1. Assume an initial geometry. Usually, this will be the equilibrium geometry of the neutral parent molecule.

2. Assume a potential energy surface for the fragment ions to evolve on. In this work, a Coulomb potential is used exclusively. Other groups have computed *ab initio* potential energy surfaces, which, they asserted, usually have greater accuracy for lower charge states [102].

3. Allow the system to evolve in time using classical dynamics. This will involve using an ordinary differential equation (ODE) solver to compute the trajectories of the charged fragments according to the Hamiltonian of the system.

4. Compare the final computed momenta with the measured momenta. The nearness of this comparison will act as a fitness parameter for the initial geometry.

5. Repeat this process for four more guess geometries. The set of five guess geometries will form a basis for a simplex algorithm. The simplex algorithm explores the solution space defined by the guess geometries until the optimum geometry is computed. The simplex algorithm is described in more detail in a later chapter.

Once the final geometry has been calculated, relevant information such as mean bond lengths and bend angles can be extracted.

Chapter 3

Molecular Geometry Reconstruction

3.1 Introduction

Once fragment momenta have been recorded and the fragmentation channel has been determined, one has, in principle all the necessary information to reconstruct the molecular geometry at the moment of the Coulomb explosion provided the molecule's initial momentum is zero. To achieve good statistical data, a viable ultrafast imaging system must be able to perform this reconstruction procedure quickly. Ideally, "on-the-fly" reconstructions should be possible.

This chapter is composed of two sections. The first section describes the classical model of molecular fragmentation used throughout this work. The second section introduces the concept of nonlinear optimization and the simplex algorithm. The third section describes the development of the simplex algorithm that was used to quickly derive initial molecular geometries from measured fragment momenta. The final section outlines some limits of applicability one must consider when applying the algorithm to experimental results.

3.2 Molecular Fragmentation Model

This section describes the model used to approximate molecular fragmentation dynamics. To good approximation, the dynamics involved in a Coulomb explosion can be described classically. This provides the double benefit of producing a completely tractable problem while retaining the ability to observe interesting physics.

3.2.1 Approximations

Several important approximations were included in the model of molecular dynamics. To a large extent, these approximations were included to improve the

tractability of a complex, nonlinear problem.

- Molecules are quantum systems, where dynamics are best described by wave packets and probabilities. However, fully quantum mechanical descriptions, particularly in the case of molecular systems are computationally demanding and are accompanied by another series of approximations such as the Strong Field Approximation (SFA) and Single Active Electron (SAE) which must be employed to produce equations which can be computed numerically. However, the adoption of a classical treatment produces a problem that is computable. Ions are treated as infinitesimally small charged particles which will evolve according to a well-defined interaction potential.

- A molecule hit by laser pulse will be ionized multiple times on the rising edge of the pulse, so long as the intensity of the pulse is sufficiently large. Assuming that the intensity profile of the pulse has a Gaussian profile in time, the timescale of these ionization events is determined by the pulse duration and peak pulse intensity. For a laser pulse that has a duration of 50 fs, the time between successive ionization events may be 5 fs or less. Rather than keep track of the dynamics of the molecule during ionization, simulations proceed directly to the final ionization state.

- The nuclei are considered to be fixed at their equilibrium positions until the final ionization. The ions gain no momentum as a result of their interaction potential or from the laser field. By demanding that the initial momentum be zero for all particles, the reconstruction procedure is greatly simplified. This approximation is significant; an attempt to correct for this approximation is made for CO_2.

- In the time-of-flight spectrometer, a DC electric field is used to accelerate the ions toward a position-sensitive detector. The ions will gain momentum as they move through the electric field. However, while the total flight time of the ions is on the order of μs, the fragmentation process we model will take place in 10 ps. Over the time period of the fragmentation, the ions will gain negligible momentum from the electric field.

- During the ionization process, several electrons will be stripped from the molecule due to the influence of the intense laser pulse. The momentum of these electrons is $\sim$1% of the momentum of the ions and is neglected.

3.2.2 Interaction potential

The interaction between the three positively charged particles is described by a Coulomb potential. While more sophisticated *ab initio* potential surfaces can be computed using commercial software such as Gaussian, the validity of these *ab initio* potentials is unclear for highly charged molecular species. Although at least

one group has used *ab initio* potential energy surfaces to analyze their Coulomb explosion data [102], most previous work has been done by assuming a Coulombic interaction. Also, it has been shown for highly charged ion experiments on CS_2^{q+} (q=3–10) [34], that a simple Coulomb model accurately predicts the kinetic energy released by the explosion fragments. Finally, the Coulomb interaction provides an analytic description for the potential energy surface of the ionic molecule and therefore allows fast computation of the ordinary differential equations of the system.

3.2.3 System Hamiltonian

For the remainder of this chapter, all geometric notation refers to the molecular frame. Although the laser polarization vector is aligned with the TOF axis, and we verify that molecules preferentially fragment along the laser polarization direction, we will ignore the laboratory frame until later in the chapter.

Consider the system shown in figure 3.1. Particles 1, 2 and 3 are described by position vectors $\mathbf{r}_1$, $\mathbf{r}_2$ and $\mathbf{r}_3$ and momentum vectors $\mathbf{p}_1$, $\mathbf{p}_2$ and $\mathbf{p}_3$. The position and momentum vectors are defined in terms of some arbitrary origin, which is usually taken to be the centre of mass of the molecule.

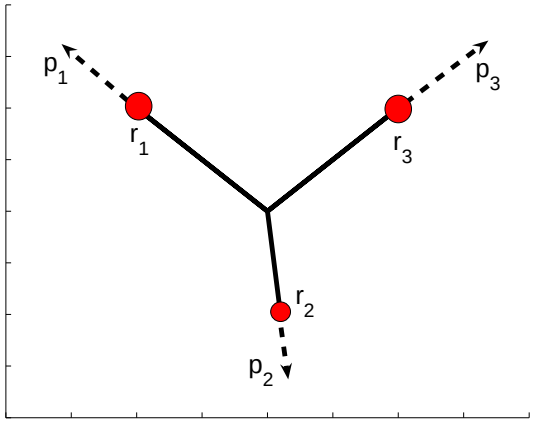

Figure 3.1: A simple system of three particles. The origin is located at the centre of mass of the system.

The Hamiltonian of the system is the sum of all energies in the system. In this case, we have the kinetic energies of each of the particles and the Coulomb potential from each of the ions. The total Hamiltonian is described by equation (3.1):

$$H = \frac{1}{2m_1}\left|\mathbf{p}_1^2\right| + \frac{1}{2m_2}\left|\mathbf{p}_2^2\right| + \frac{1}{2m_3}\left|\mathbf{p}_3^2\right| + k\left[\frac{q_1q_2}{|\mathbf{r}_1-\mathbf{r}_2|} + \frac{q_1q_3}{|\mathbf{r}_1-\mathbf{r}_3|} + \frac{q_2q_3}{|\mathbf{r}_2-\mathbf{r}_3|}\right] \quad (3.1)$$

The change in position with respect to time is given by the gradient of the Hamiltonian with respect to momentum. Therefore for the ith particle:

$$\dot{\mathbf{r}}_i = \nabla_{\mathbf{p}_i} H = \frac{\mathbf{p}_i}{m_i} \tag{3.2}$$

The change in momentum with respect to time is given by the gradient of the Hamiltonian with respect to position. Some care must be taken with the derivative of the position, since we must consider the difference in the position between particles.

$$f(\mathbf{r}_1) = \frac{1}{|\mathbf{r}_1 - \mathbf{r}_2|} \tag{3.3}$$

$$-\nabla_{\mathbf{r}_i} f(\mathbf{r}_1) = -\frac{\mathbf{r}_1 - \mathbf{r}_2}{|\mathbf{r}_1 - \mathbf{r}_2|^3} \tag{3.4}$$

Using equations (3.3) and (3.4), we get for the derivative of particle 1's momentum vector:

$$\dot{\mathbf{p}}_1 = -\nabla_{\mathbf{r}_1} H = -k\left[\frac{q_1 q_2 (\mathbf{r}_1 - \mathbf{r}_2)}{|\mathbf{r}_1 - \mathbf{r}_2|^3} + \frac{q_1 q_3 (\mathbf{r}_1 - \mathbf{r}_3)}{|\mathbf{r}_1 - \mathbf{r}_3|^3}\right] \tag{3.5}$$

This is given more generally in equation (3.6):

$$\dot{\mathbf{p}}_i = -\nabla_{\mathbf{r}_i} H = -\sum_{j \neq i} k \frac{q_i q_j (\mathbf{r}_i - \mathbf{r}_j)}{|\mathbf{r}_i - \mathbf{r}_j|^3} \tag{3.6}$$

3.2.4 Simulated time evolution of a linear system

Once the Hamiltonian of the system is described by 3.1, it is a straightforward procedure to simulate the evolution of the system over time. Consider a carbon dioxide molecule in its equilibrium geometry of $r_{12} = 1.16$ Å, $r_{23} = 1.16$ Å, $\theta = 180°$, $m_1 = 16$ amu, $m_2 = 12$ amu, $m_3 = 16$ amu. Now assume the molecule is ionized to the CO_2^{3+} state, and that each ion carries a charge of +1. The carbon ion is located at the origin. The MATLAB function `ode23`, a third-order Runge-Kutta ordinary differential equation solver is used to perform the calculation by numerically solving equations 3.2 and 3.6. During the calculation, the time between successive steps begins at 1 attosecond (10^{-18} s) and increases as the system approaches the asymptotic momentum condition. Since the molecular ion is initially placed in a linear geometry, the repulsive Coulomb force will accelerate the oxygen ions in either the positive or negative x-direction. The carbon ion, which experiences an identical force from left and right, will not experience a change in momentum and will not move. The early stages of this motion can be seen in figure 3.2.

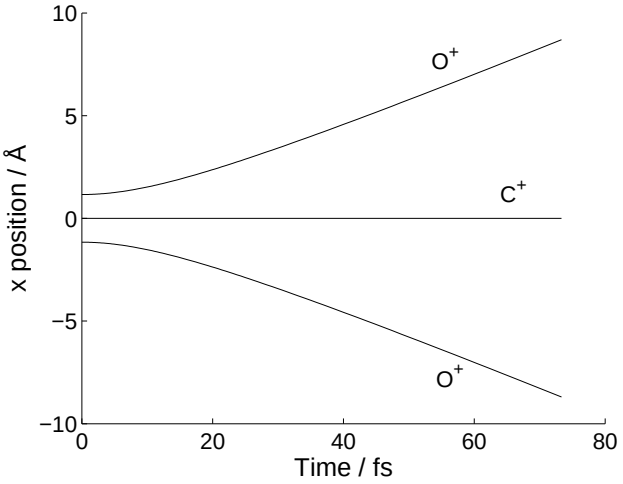

Figure 3.2: Time evolution of the linear system. The carbon ion starts at the position $x = 0$, while the two oxygen ions start at $x = \pm 1.16$ Å. The motion of the ions is computed for 10 ps.

The momentum of the system is computed in a similar fashion. As stated above, the initial momentum of the system is taken to be zero. As seen in figure 3.3, the oxygen ions are accelerated in opposite directions until they reach the point where the Coulomb interaction is no longer experienced. The carbon ion, located between the oxygen ions, never experiences an unbalanced force and does not move from its initial position.

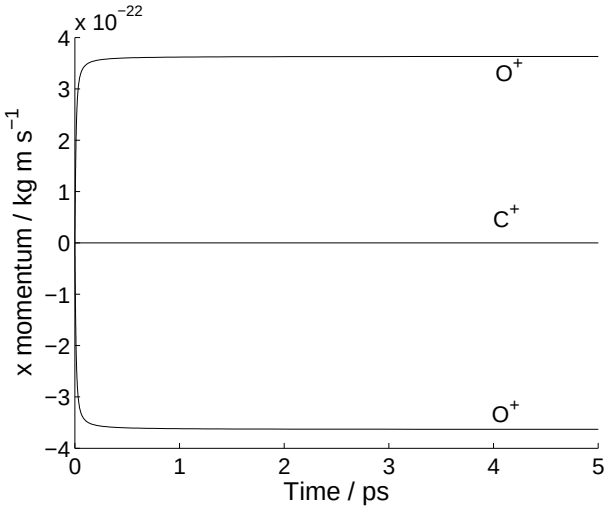

Figure 3.3: Time evolution of the particle momentum. The ions will have almost reached their asymptotic momentum after 1 ps, when the ionic separations are approximately 100 times larger than the equilibrium bond lengths. The ODE solver continues the calculation until 10 ps have elapsed, after which the asymptotic momentum is observed.

These results are illustrative of a typical Coulomb repulsion scenario. The ions will achieve their asymptotic momentum vectors within several ps of the Coulomb explosion. Typically, the ODE solver will compute 10 ps of motion, at which point the asymptotic condition is satisfied in general.

3.2.5 Solving for the initial molecular structure

In determining the initial structure of the molecule prior to Coulomb explosion, the asymptotic momenta for all the particles must match the value determined by measurement in the lab. Solving this system of equations is a highly nonlinear problem. Since the amount of data is quite large, an efficient system for finding local minima is required.

3.3 Nonlinear Optimization

Given the final positions and momenta of all fragments in a Coulomb explosion and a Hamiltonian for the system, one is in principle able to determine the initial molecular structure. However, this is a highly nonlinear problem where small perturbations in the initial bond lengths and bend angle will result in large changes in the final momenta. Furthermore, as the ordinary differential equations (and their first derivatives, depending upon the solution method) must be solved, the process is computationally intensive. For this work, a nonlinear optimization algorithm was developed to determine the initial bond lengths and bend angles from triatomic molecular fragmentation. Several nonlinear methods were examined to determine the most suitable algorithm.

3.3.1 Least squares

The least squares method minimizes the sum of the residuals to determine the values of unknown quantities in a statistical model. Least squares is widely employed in statistics to determine the behaviour of linear systems.

To employ least squares, one must have a data set containing n points $(y_i, \mathbf{x}_i)$ with $i = 1, 2, ..., n$. Here, y is the dependent variable while $\mathbf{x}$ are the independent variables. A model function is constructed such that $y = f(\mathbf{x}, \mathbf{a})$ where $\mathbf{a}$ are the adjustable parameters to be optimized. The sum square error S,

$$S = \sum_{i=1}^{n} \left(y_i - f(\mathbf{x}_i, \mathbf{a})\right)^2 \tag{3.7}$$

is minimized with respect to the parameters $\mathbf{a}$ [120].

Weaknesses of least squares

The least squares technique is best suited for solving linear systems. However, a non-linear system can be solved using a least squares algorithm by dividing the problem into linear and non-linear problem. The linear problem has a closed form solution. The general, non-linear, unconstrained problem does not possess a closed form solution and supplementary, recursive techniques must be employed to determine a suitable solution. Due to these additional complications, the least squares technique was abandoned as the solution algorithm.

3.3.2 Gradient descent

The gradient descent or method of steepest descent is an optimization algorithm used to find the local minimum of a function. At each iteration of the algorithm, one takes a step proportional to the negative of the gradient of the function at the current point.

Given a real-valued function f that is defined and differentiable in the neighborhood of the point $\mathbf{a}$, $f(\mathbf{x})$ will decrease fastest if one goes from $\mathbf{a}$ in the direction of $-\nabla f(\mathbf{a})$. If

$$\mathbf{b} = \mathbf{a} - \gamma \nabla f(\mathbf{a}) \tag{3.8}$$

for $\gamma > 0$ and small, then

$$f(\mathbf{a}) \geq f(\mathbf{b}) \tag{3.9}$$

By starting with a guess for the local minimum, $\mathbf{x}_0$, it should be possible to form a sequence of guesses $\mathbf{x}_0, \mathbf{x}_1, \mathbf{x}_2, \ldots$ such that

$$\mathbf{x}_{n+1} = \mathbf{x}_n - \gamma_n \nabla f(\mathbf{x}_n), n \geq 0 \tag{3.10}$$

By equation 3.9 and allowing γ_n to vary at each step, it follows that

$$f(\mathbf{x}_0) \geq f(\mathbf{x}_1) \geq f(\mathbf{x}_2) \geq \ldots \tag{3.11}$$

so that a local minimum is reached [121]. Ideally, several runs should be performed on the surface to verify that the local minimum is a global minimum.

Weaknesses of gradient descent

The gradient descent algorithm has several weaknesses. The first weakness is that the algorithm can take many iterations to converge on a local minimum, particularly

in the case where the curvature is very different in different directions. The second weakness of the algorithm is that the step-size, γ should be optimized at each step of the algorithm. This can be a very time-consuming operation. Using a fixed γ is not advisable as it can lead to poor results in finding the true local minimum. The final weakness stems from the necessity to calculate $\nabla f(\mathbf{x}_n)$ at each point of the minimization. This is also a time-consuming operation and would be particularly unfavourable in systems with many independent variables.

3.3.3 Simplex method

The simplex method for unconstrained non-linear optimization has been in the literature for more than 40 years. Suggested by Spendley et al. [122], the algorithm can be applied to problems of minimizing $f(\mathbf{x}), \mathbf{x} \in R^n$, where f is a function of the decision variables $\mathbf{x} = (x_1, x_2, ...x_n)$. It has been successfully applied to a wide variety of real, physical systems such as chemical processes which can be difficult to describe analytically [123].

A simplex is a convex hull of $n + 1$ points, $x_1, x_2, x_3, ..., x_{n+1}$ in R^n such that $\{x_2 - x_1, x_3 - x_1, ..., x_{n+1} - x_1\}$ is a linearly independent set. A convex hull is a mathematical construction that is most easily visualized for points in a plane. For a group of points, the convex hull may be visualized by an elastic band stretched to encompass all the points. When the elastic is released, it assumes the shape of the convex hull. For three linearly independent points in a plane, the convex hull is simply a triangle. Higher dimension convex hulls are more difficult to visualize. A number of different solutions that form a simplex are maintained and used to generate a new and better solution. This better solution will replace one of the current solutions in a new simplex on the next iteration.

Consider a case where there are N parameters to be set. Let $x_1, x_2, ...x_{N+1}$ be the points in R^N that form the current simplex. The algorithm will replace the worst point x_W (the point having the highest function value) among the $N + 1$ points with a new and better point. The replacement of the point involves three types of operations: reflection, expansion, and contraction. Each of these operations seeks to explore the phase space of the parameters in the most optimal way. The operations require a reflection coefficient $\alpha > 0$, an expansion coefficient $\beta > 1$, and a contraction coefficient $\gamma < -1$. The complete algorithm is stated in Appendix B.

Benefits of the simplex method

There are a number of reasons for choosing the simplex method over, for instance, an algorithm based on the steepest descent of the function or a random, shotgun approach. Using the simplex algorithm, only function values need to be evaluated. There is no need to compute derivatives. Furthermore, only $n + 1$ linearly independent points are required to make the simplex. Finally, each iteration of the

algorithm only generates one new point. Taken together, these characteristics allow for efficient solving of the molecular geometry.

3.4 Simplex Test Scenarios

In the simple charged particle model, each particle has three unconstrained degrees of freedom, giving nine independent variables that must be determined. While a 10-dimensional simplex could solve such a problem, the computational time required scales according to the dimensionality. It is therefore beneficial to place constraints on the system that will lower the dimensionality while still producing physically meaningful calculations.

Constraints will be placed on the system in several test scenarios. These test scenarios will provide concrete examples to illustrate the operation of the simplex algorithm.

3.4.1 Linear molecule test case

Using our classical model, the asymptotic fragment momenta for a three-body system can be calculated for an arbitrary geometry. For a simple yet illustrative test case, the breakup dynamics of the CO_2^{3+} molecular ion into three charged fragments are investigated by placing the fragment ions at the equilibrium geometry. As previously mentioned, this sets $r_{12} = 1.16$ Å, $r_{23} = 1.16$ Å, $\theta = 180°$, $m_1 = 16$ amu, $m_2 = 12$ amu, and $m_3 = 16$ amu. For simplicity, all ions were placed on the x-axis, with the carbon ion at the origin. With the Hamiltonian defined according to Equation 3.1, the system was allowed to evolve for 10 ps. The computed asymptotic momentum vectors were $\mathbf{p} = \pm$ 3.633 x 10^{-22} kg m s^{-1} for the oxygen fragments and zero for the carbon fragment. Ideally, these are the values we will reproduce by assuming guess geometries and allowing the simplex to evolve an optimal geometry.

With the carbon ion fixed at the origin, there are only two independent variables in the system, r_{12} and r_{23}. Therefore, three linearly independent guess solutions are required to initialize the simplex algorithm. Furthermore, these initial guess solutions should span a large part of the phase space [121]. The guess solution geometries are given in Table 3.1.

The fitness of the jth solution, F_j, is defined according to a least-squares condition

$$F_j = \sum_{i=1}^{2} \left(\mathbf{p}_i - \mathbf{f}(\mathbf{x}_j)\right)^2 \tag{3.12}$$

where $\mathbf{f}$ is the function that numerically produces the asymptotic momentum values. A particular geometry $\mathbf{x}_p$, will approach the true geometry as $F_p \to 0$. A graphical

Solution	r_{12}	r_{23}
1	0.5 Å	0.5 Å
2	8 Å	0.5 Å
3	0.5 Å	8 Å

Table 3.1: Guess solutions used for simplex algorithm. The bond lengths in each solution have not been chosen individually for physical likelihood. Rather, the solution set has been chosen to collectively span a large range of physically likely bond length values.

representation of how quickly the algorithm converges is shown in figure 3.4. In idealized situations, convergence is typically achieved in less than 100 iterations.

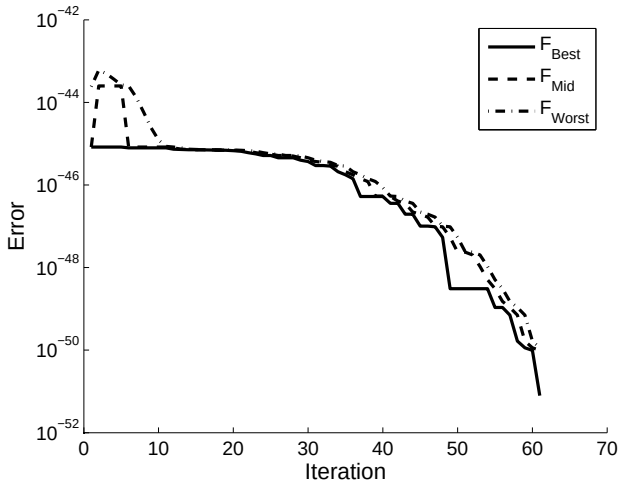

Figure 3.4: Solution error as a function of algorithm iteration. The error associated with the best (solid line), middle (dashed line), and worst (dot-dashed line) solutions is calculated according to Equation 3.12. Typically, the algorithm stops when an error of 10^{-51} or less is achieved.

The test case can also be used to illustrate the progress of the algorithm as it explores the two-dimensional phase space. Figure 3.5 demonstrates how the simplex rapidly collapses until the final geometry is obtained. Some effort may be taken to optimize the coefficients that govern the evolution of the simplex and thereby reduce the number of iterations. However, this process can be tedious and non-intuitive. In this particular case, the reflection coefficient, $\alpha = 1$, the expansion coefficient, $\beta = 2$, and the contraction coefficient, γ = -0.5.

3.4.2 Bent molecule test case

In the previous section, the simplex algorithm was demonstrated to recover the geometry of simple triatomic molecules where explosion dynamics are constrained

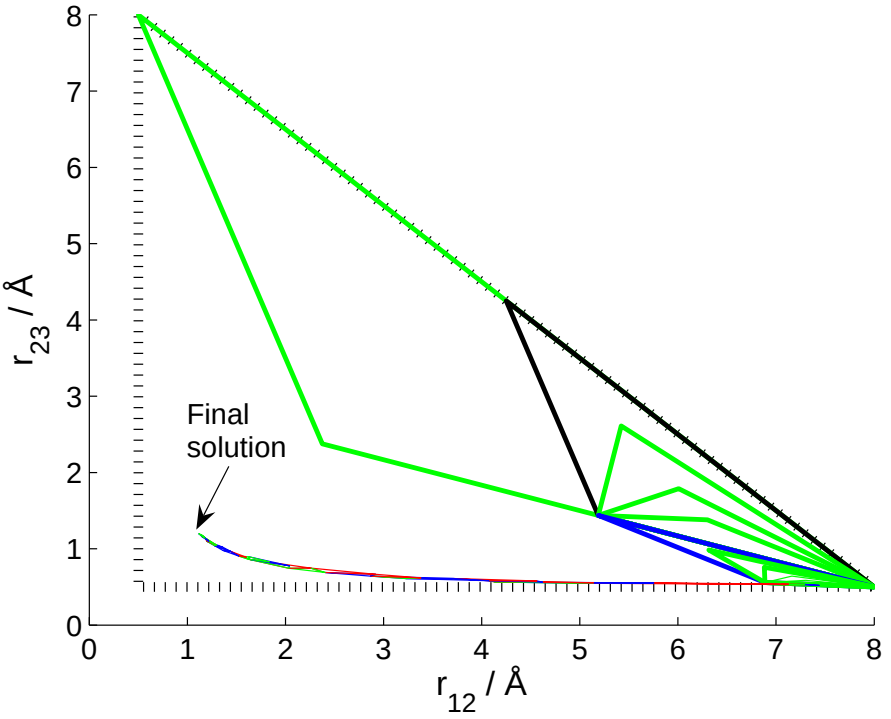

Figure 3.5: Progress of simplex algorithm towards final (best) geometry. The initial simplex, consisting of the guess geometries is shown dotted in black. Subsequent operations are indicated by colour-coded triangles. Expansions are shown in red, reflections in blue, contractions in green and compression operations are in black. As can be seen, most early operations are contractions while operations near the final geometry are largely expansions and reflections.

along the molecular axis. In effect, this motion is equivalent to a stretch along the molecular axis. The next test is to examine whether the algorithm can accommodate bent geometries. The challenge is that this will introduce new variables that the simplex must solve.

As before, the position of the carbon ion was fixed at the origin. The oxygen ions were placed at positions in the $x - y$ plane that correspond to the equilibrium geometry of the CO_2 molecule. That is, $r_{12} = 1.16$ Å, $r_{23} = 1.16$ Å, and $\theta = 174°$. The x- and y-coordinates of the oxygen ions were used as the independent variables. The guess geometries used are given in Table 3.2. Experimentally, it has been observed that molecules tend to bend as they stretch [90] and this was considered when choosing the guess geometries.

Once again, the simplex algorithm was able to deduce the correct geometry in fewer than 100 iterations, as shown in figure 3.6. This is remarkable given that the algorithm had four variables to solve. This test was successfully repeated for a variety of bond lengths and bend angles. Note that the stretch in the bond lengths was always symmetric.

Solution	r_{12}	r_{23}	θ
1	0.5 Å	0.5 Å	180°
2	1 Å	1 Å	170°
3	3 Å	3 Å	160°
4	5 Å	5 Å	150°
5	10 Å	10 Å	140°

Table 3.2: Guess solutions used for simplex algorithm in bent molecule test. We have used the physically observed relation that as molecules bend, they also stretch symmetrically [90].

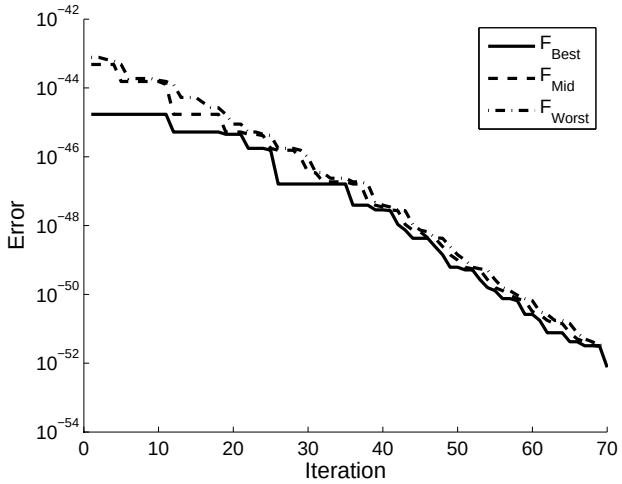

Figure 3.6: Solution error as a function of algorithm iteration for bent geometry. The plotted lines styles are the same as in figure 3.4.

3.4.3 Asymmetrically stretched, bent molecule

The ultimate test of the algorithm is to recover the geometry of a triatomic molecule that is bent and has different bond lengths. While the number of independent variables is the same as the bent, symmetric molecule, the guess geometries must be chosen with somewhat more care. In the previous test, all of the guess geometries had symmetric bond lengths. If this solution set is used for an asymmetric molecule, the simplex algorithm will return a symmetric geometry with bond lengths equal to the average of the true bond lengths.

An alternative approach to generating a trial solution set is to individually adjust a single variable from one trial to another. This has the benefit of guaranteeing that each solution in the set is linearly independent. Once again, the x- and y-coordinates of the oxygen ions were used as the independent variables while the carbon was fixed at the origin.

To verify that the trial solution set in Table 3.3 is applicable for a large number of geometries, a variety of test cases were assembled. The results are shown in

Solution	x_{O_1}	y_{O_1}	x_{O_2}	y_{O_2}
1	0.9986 Å	0.0523 Å	-0.9986 Å	0.0523 Å
2	4.9931 Å	0.0523 Å	-0.9986 Å	0.0523 Å
3	0.9986 Å	0.2617 Å	-0.9986 Å	0.0523 Å
4	0.9986 Å	0.0523 Å	-4.9931 Å	0.0523 Å
5	0.9986 Å	0.0523 Å	-0.9986 Å	0.2617 Å

Table 3.3: Guess solutions used for simplex algorithm in asymmetric, bent molecule test. The first solution is the equilibrium geometry for CO_2, with slightly shortened bond lengths (r_{12} = 1 Å, r_{23} = 1 Å, θ = 174°). The second solution replaces x_{O_1} with $5x_{O_1}$. This procedure is repeated for the other trial solutions.

Table 3.4. As can be seen, the simplex algorithm was able to successfully recover all of the test case geometries, although at the cost of longer computation times.

Trial	r_{12}	r_{23}	θ	Iterations
1	1.16 Å	1.16 Å	174°	91
2	1.16 Å	2.32 Å	174°	107
3	1.16 Å	1.16 Å	160°	152
4	1.16 Å	1.16 Å	140°	256
5	2.32 Å	1.16 Å	140°	160
6	3.48 Å	1.16 Å	140°	267
7	5.80 Å	1.16 Å	140°	241

Table 3.4: Asymmetric, bent test geometries. Based on these test results, the maximum number of iterations allowed for experimental data sets was set to 300.

3.5 Experimental Data Processing

Recall that for a given Coulomb explosion where all fragments are detected, the ultrafast imaging apparatus determines the charge state and asymptotic momentum of each fragment. Ideally, this information is all that is required for the simplex algorithm to produce the correct molecular structure. In reality, a small amount of preprocessing is necessary before the algorithm can be employed.

In general, real molecules are randomly oriented in space. Given an isotropic distribution, any preference in alignment will be determined by the polarization of the electric field of the laser. Circularly polarized light will isotropically ionize an ensemble of gas phase molecules that are in a plane normal to the laser's **k** vector. By contrast, if linearly polarized light is used to initiate a Coulomb explosion,

molecules aligned parallel to the laser field will ionize much more readily than molecules that are not aligned.

In either polarization case, fragment momentum vectors will be measured with components in the X-, Y-, and Z-directions which correspond to the laboratory frame. A simplex could be constructed to solve for a molecule's geometry from measurements taken in the laboratory frame. However, this would require solving for 9 variables or using a ten-dimensional simplex. As was just demonstrated with the generated test data, the number of algorithm iterations scales as the number of variables in the simplex. Therefore, a geometric operation is performed to reduce the dimensionality of the random momentum vectors.

3.5.1 Geometric operations to rotate explosion plane

To reduce computation time, measured momentum vectors in the laboratory frame are rotated geometrically into an arbitrary molecular frame. Since there are only three momentum vectors, these will form a plane if

$$\det \begin{vmatrix} p_{X_1} & p_{Y_1} & p_{Z_1} \\ p_{X_2} & p_{Y_2} & p_{Z_2} \\ p_{X_3} & p_{Y_3} & p_{Z_3} \end{vmatrix} = 0 \tag{3.13}$$

Assuming this condition is satisfied, the normal of the plane is calculated by

$$\hat{\mathbf{n}} = \frac{\mathbf{p_1} \times \mathbf{p_2}}{|\mathbf{p_1}||\mathbf{p_2}|} \tag{3.14}$$

By construction, this newly defined plane, P, passes through the origin. The momentum vectors are then rotated by the dihedral angle, δ, which is the angle between $\hat{\mathbf{n}}$ and $\hat{\mathbf{K}}$, the normal of the XY plane, around the intersection line defined by $\hat{\mathbf{n}} \times \hat{\mathbf{K}}$. At the conclusion of this operation, the three momentum vectors lie in the XY plane. This operation is shown graphically in figure 3.7.

The momentum vectors are rotated again such that θ_v, the angle between the oxygen fragments (in the case of CO_2), is subtended by the X-axis. This operation ensures that $\hat{\mathbf{p}}_{O_1}$ points into the first quadrant, $\hat{\mathbf{p}}_{O_2}$ points into the fourth quadrant and $\hat{\mathbf{p}}_C$ points into either the second or third quadrant. With the momentum vectors redefined, trial solutions for the simplex similar to those in the previous section can be used. In all trial solutions, the carbon ion is fixed at the origin while the oxygen ions are given starting positions in the appropriate quadrants.

3.5.2 Computation efficiency

The test version of the simplex algorithm was coded in MATLAB. On a typical desktop PC, one triple event took $10 \sim 20$ seconds to compute. While this was

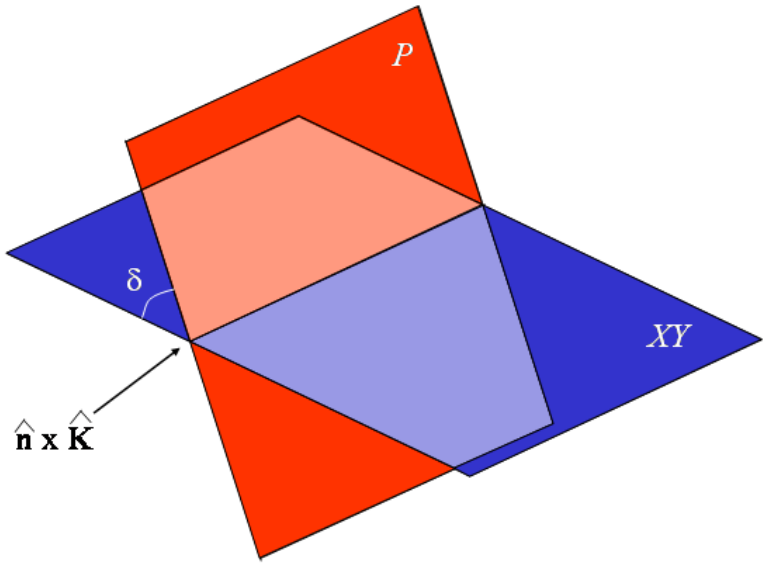

Figure 3.7: Rotation of momentum plane through dihedral angle. The plane, P, is defined by the determinant of the momentum vectors in equation 3.13. The original momentum vectors are rotated through the dihedral angle, δ, so they lie in the XY plane.

sufficient for test purposes, a large data set from an experiment would take days, even when the calculations were distributed over several workstations. The working code was reproduced in C, using some routines from the GNU Scientific Library. This resulted in much faster analysis times and large data sets could be completed in two hours instead of days.

3.6 Limitations

As shown in previous sections, the algorithm has proven to be an excellent tool for solving for geometric structures. Nevertheless, some issues remain. These remaining issues stem from the semi-chaotic nature of the 3-body problem. That is, small changes in the initial structure can lead to large changes in the asymptotic momenta. During testing, the simplex algorithm did not accurately recover the geometry of extremely bent molecules. When the bend angle was less than $\sim 100°$, the algorithm became confused and did not converge. Also, the algorithm failed to converge when the fragment masses were too large, approximately 100 amu. The algorithm was perfectly capable of deducing the geometry of small, linear molecules. Having assessed what the algorithm can and cannot do, we focus

our attention on light, linear molecules as the geometry of these molecules should be readily recoverable.

Chapter 4

Ultrafast Imaging of Multielectronic Dissociative Ionization of CO_2 in an Intense Laser Field

This chapter is adapted from an article that was printed in *J. Phys. B: At. Mol. Opt. Phys.*, 40:117-129, 2007, produced in collaboration with Stephen J. Walker, Robin Helsten and Joseph H. Sanderson.

4.1 Introduction

Studies on polyatomic molecules have shown that interaction with an intense ($\sim 10^{14}$-10^{16} W cm^{-2}) laser field leads to substantial geometric deformation that occurs on the timescale of ultrafast laser pulses [49, 51, 52, 77, 78, 81, 82, 124, 80]. While several triatomic systems have been investigated, CO_2 has remained a target of special interest [47, 125, 77, 82, 84, 126].

It is well established when laser pulse durations are on the order of 50-100 fs, the kinetic energy released in multi-electron dissociative ionization the observed explosion energies are considerably lower than would be expected from a Coulomb explosion of the molecule from its equilibrium geometry. The observed explosion energies are consistent with separations $R_C \simeq 2R_{eq}$ – $3R_{eq}$, where R_C is the so-called critical distance and R_{eq} is the equilibrium bond length. If reconstruction of the equilibrium geometry is the ultimate goal, recent work by Légaré *et al* [95] has shown that bond length distributions less than R_C can be recovered if $7 \sim 8$ fs laser pulses are employed. The mechanism that gives rise to R_C is described by enhanced ionization which has been explained using both classical [54] and quantum mechanical models [56, 55]. Previous long pulse measurements of CO_2 have reported an R_C value somewhat lower than the calculated value of 3.5 Å[77].

In this work, we exploit the ability of the complete momentum coincidence imaging technique to make the first complete momentum coincidence imaging measurements of fragment ions produced from CO_2 in an intense laser field. This allows us to make the first unambiguous measurement of the structure of CO_2 and reveal significant differences to previous incomplete methods, in terms of the most likely geometry and the extent of molecular deformation in a laser pulse.

4.2 Experimental

The experimental apparatus has been described in a previous chapter. Unique to this experiment, a laser intensity $\sim 10^{15}$ W cm^{-2} was used. This intensity was verified by examining the time-of-flight signal from multiply ionized xenon. The voltages applied to the first (3020 V) and sixteenth (20 V) rings are adjusted to give a field strength of approximately 260 V cm^{-1}. This field strength ensures all fragment ions are collected within $\sim$1.5 μs.

With a MCP diameter of 40 mm ϕ, we are able to detect O^+ ions with a momentum perpendicular to the TOF axis of $\sim$5 x 10^{-22} kg m s^{-1} and C^+ ions with a momentum perpendicular to the TOF axis of $\sim$4.3 x 10^{-22} kg m s^{-1}. Since our laser polarization was parallel to the TOF axis, and CO_2 molecules will align with the laser polarization, it is the perpendicular momentum of the C^+ ions which will limit the detection efficiency. The DC field in the TOF is therefore set to ensure 100% collection efficiency of perpendicularly ejected fragments.

The four signals from the anode are amplified (Ortec 142B) then recorded by two PC oscilloscope cards (Gage Applied Dual Compuscope CS82G, time resolution 1 ns) at a rate of 1000 laser shots per second. We are therefore able to take full advantage of our kHz amplifier by recording ion fragment information from each laser shot. Events are discriminated after data collection using software, and more than 10 fragments per laser shot can be detected. In practice, we only analyze triple coincidence data, that is, where exactly three ions are detected from the same laser shot. By capturing and analyzing data in parallel, event discrimination is performed in real-time. For the purposes of this experiment, we set a 40 ns interval between successive events.

To ensure all fragment ions originate from a single parent ion, the chamber pressure must be held low enough so that the number of molecules in the laser focus is less than one. The main chamber is pumped to a base pressure as low as 7 x 10^{-10} Torr. Room temperature CO_2 gas is introduced effusively through a leak valve and typical experimental pressures are 5 x 10^{-8} Torr. At this temperature, over 90% of the CO_2 molecules will be in the ground vibrational level (000), with the remainder in the lowest bending mode (010) [127]. Although we only consider the bend angle distribution of the (000) vibrational level, we postulate that we may observe slightly more bent geometries.

The data presented in this chapter consists of ∼2 x 10^4 triple coincidence events, generated using ∼10^6 laser shots.

4.3 Data Reduction

For each fragment ion, the position is determined as described in [128]. With the position and time information, the momentum vector $\mathbf{p} = (p_X, p_Y, p_Z)$ of a single fragment is calculated according to [91]. Briefly, for a fragment of mass m, and charge q, the momentum components along the X-, Y- and Z-axes in the laboratory frame are given by

$$p_X = m\frac{(X - X_0)}{t},\ p_Y = m\frac{(Y - Y_0)}{t},\ p_Z = \frac{qE}{2}\frac{(t_0^2 - t^2)}{t} \tag{4.1}$$

where t is the measured arrival time, X and Y are the displacements of the fragment with respect to an ion with $p_X = p_Y = 0$, E is the constant electric field in the time-of-flight tube, and t_0 is the flight time of a fragment with $p_Z = 0$. We have calibrated our energy measurements with other molecular targets.

Channel-resolved coincidence imaging maps are produced by collecting the events in which all fragment ions are detected. For example, ions created via the (2,2,2) Coulomb explosion pathway, $CO_2^{6+} \rightarrow O^{2+}$+$C^{2+}$+$O^{2+}$, are identified by events where two O^{2+} ions and one C^{2+} ion hit the detector after a single laser shot. False coincidences, which can result from the presence of more than one target molecule in the laser focus, noise or background gases, are suppressed by filtering events according to the momentum sum of the Coulomb explosion. An event is interpreted as a false coincidence if the sum $\sum \mathbf{p}_i'$ of the observed momenta is greater than 5 x 10^{-23} kg m s^{-1}. 95% of events are positive coincidences.

4.4 Results

4.4.1 Coulomb explosion of CO_2

Figure 4.1 shows a two dimensional representation of the triple coincidence map for CO_2. At the present laser intensity, ∼ 10^{15} W cm^{-2}, charge states up to CO_2^{6+} can be obtained. As can been clearly seen, three O^+ peaks are apparent. The O_f^+ and O_b^+ peaks correspond to oxygen fragments coming from the (1,1,1) Coulomb explosion channel. The O_m^+ peak comes from other dissociative processes. The forward-backward peak pattern is also evident in the higher charge state.

The coincidence imaging technique is a direct method to identify all fragments from a single Coulomb explosion event with a specific charge number. The most prominent explosion pathways are:

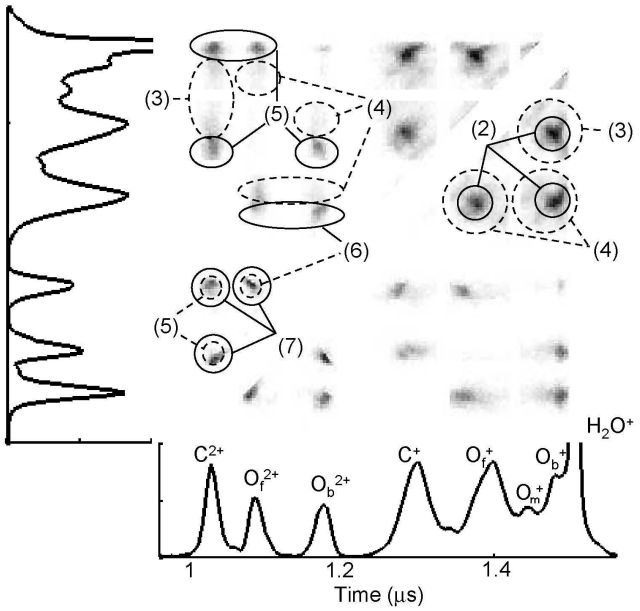

Figure 4.1: 2D representation of triple coincidence map. Each symmetric process produces six points, while each asymmetric process produces twelve points. The numbered correlated regions correspond to the appropriate explosion pathways (see text). The large number of overlapping islands make it difficult to determine the explosion channel solely from this information. However, channel identification becomes straight-forward when momentum conservation is considered.

$$CO_2^{3+} \rightarrow O^+ + C^+ + O^+ \text{ , (1,1,1)} \tag{4.2}$$

$$CO_2^{4+} \rightarrow O^+ + C^{2+} + O^+ \text{ , (1,2,1)} \tag{4.3}$$

$$CO_2^{4+} \rightarrow O^+ + C^+ + O^{2+} \text{ , (1,1,2)} \tag{4.4}$$

$$CO_2^{5+} \rightarrow O^+ + C^{2+} + O^{2+} \text{ , (1,2,2)} \tag{4.5}$$

$$CO_2^{5+} \rightarrow O^{2+} + C^+ + O^{2+} \text{ , (2,1,2)} \tag{4.6}$$

$$CO_2^{6+} \rightarrow O^{2+} + C^{2+} + O^{2+} \text{ , (2,2,2)} \tag{4.7}$$

Of these six pathways, (4.2), (4.3), (4.6) and (4.7) will be described as symmetric processes while (4.4) and (4.5) are asymmetric processes.

Since the momenta of all the fragment ions $\{\mathbf{p}_i\}$ is known, the total kinetic energy released can be readily calculated by $E_{kin} = \sum |\mathbf{p}_i|^2 / (2m_i)$ where m_i is the mass of the ith fragment ion. The energy distributions for the six explosion pathways are shown in figure 4.2. These kinetic energy release (KER) distributions can be compared with the results of Bryan *et al* [82] and the calculated kinetic energy release (CKE) which assumes the initial geometry is that of the ground state neutral molecule. Our results compare well with Bryan *et al* for those explosion channels where the carbon fragment has been singly ionized. Of particular interest, we note definite structure within the energy distributions, such as a low energy shoulder in the (1,1,1) signal, a high energy shoulder in the (1,2,1) signal and in the case of the (2,2,2) signal we observe a low energy feature close to the noise level. We have good statistics for the (1,1,1) and (1,2,1) channels, but the statistics are somewhat worse for the (2,2,2) channel so the low energy feature seen there may be exaggerated.

In those channels with doubly charged carbon fragments, the detected KER is somewhat lower than reported by Bryan *et al.* It is clear from our results that the measured KER increases substantially when an oxygen fragment is doubly ionized, for example as with (1,1,1) $\rightarrow$ (1,1,2), but not nearly as much when a carbon is doubly ionized, as with (1,1,1) $\rightarrow$ (1,2,1). As expected, the CKE values are substantially larger than the measured KER values, due to the assumption of equilibrium bond lengths and pure Coulombic dissociation.

4.4.2 Molecular geometry reconstruction

With the three-dimensional momentum vectors of the fragments now determined, it is straightforward to reconstruct the apparent molecular geometry just before the Coulomb explosion. The momentum of the ion fragments is then calculated by numerically solving the classical equations of motion in the Coulomb field for some initial set of guesses at the molecular structure, assuming the initial momentum is zero. A more accurate but computationally demanding approach utilizes an *ab initio* potential energy surface [95], but here we use the simpler Coulomb approximation to better compare with previous results. The parameter space defined by this set of guesses for the molecular structure is explored using a simplex algorithm [122] until the observed asymptotic momentum vectors are reproduced.

The distributions of the molecular structures of the six explosion channels are shown in figure 4.3. As far as we are aware, this the first time channel resolved molecular structures have been derived from an experiment of laser initiated Coulomb explosions. As seen in (c) and (e) of figure 4.3, the explosion channels (1,1,2) and (2,1,2) have average bond lengths much closer to the equilibrium bond length than the other channels. Also, the variation in bond length and bend angle does not appear to be smoothly changing with charge state. Furthermore,

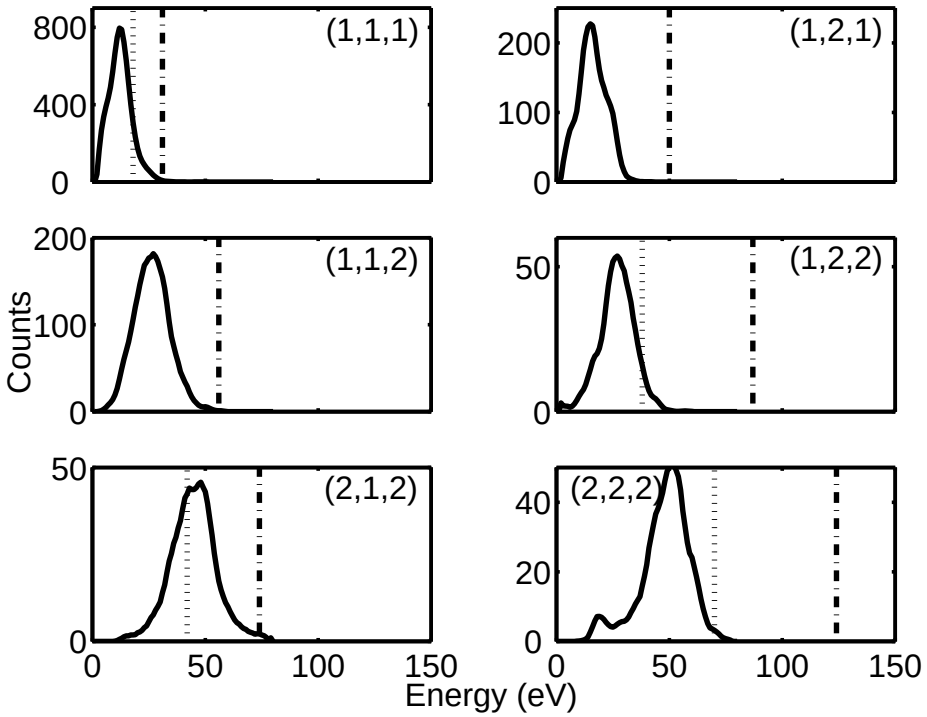

Figure 4.2: Released kinetic energy distributions for the (1,1,1), (1,2,1), (1,1,2), (1,2,2), (2,1,2) and (2,2,2) Coulomb explosion pathways. Experimental data has been smoothed using a three-point triangle filter. Included for comparison are the kinetic energy release values from [82] (dotted), as well as theoretical kinetic energies assuming fragmentation proceeds from the equilibrium geometry (dot-dash).

the (1,2,1) channel shows evidence of a localization in the distribution around 2.5 Å. Based on figure 4.2 and figure 4.3, we can say that substantial changes in the energy spectrum follow from double ionization of the oxygen fragments, while the geometric distributions can be qualitatively grouped according to the charge of the carbon fragment. For a more quantitative analysis of the geometric data, bend angle and bond length distributions are examined independently.

Figure 4.4 shows in detail the bend angle distributions from other long-pulse experiments [51, 77, 82]. The results of Bryan *et al* are similar to ours while the data reported by Cornaggia and Hishikawa *et al* have a somewhat wider bend angle distribution than was measured in this work. Furthermore, Bryan *et al* closely agrees with our value of ∼171°, while Cornaggia and Hishikawa *et al* report a peak bend angle of 180°. The ground state bend angle distribution as calculated by [129] is also included for comparison. The ground state distribution, which accounts for all normal modes of vibration, has a width (∼13°) and peak (∼174°) similar to our results.

Figure 4.5 plots the channel dependence of the bend angle distribution. We see unambiguously the narrowing of the bend angle distribution with increasing charge state and the peak of the distribution approaching the ground state equilibrium

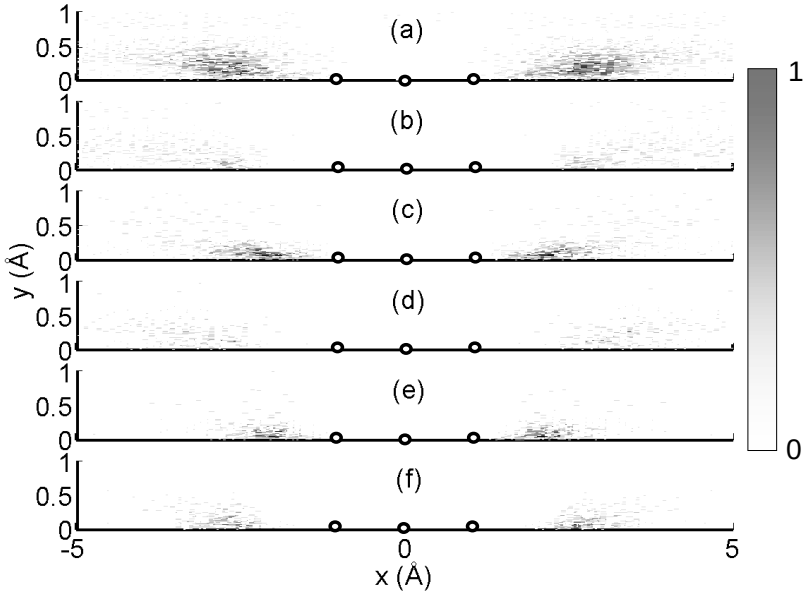

Figure 4.3: Recovered molecular geometry mapped directly from observed coincidence momentum imaging. The channels shown are (a) (1,1,1), (b) (1,2,1), (c) (1,1,2), (d) (1,2,2), (e) (2,1,2), (f) (2,2,2). In each plot, the carbon fragment is at the origin, while the higher charged oxygen fragment lies along the positive x-axis. The equilibrium geometry has been included for comparison (open circles). Note that these are density plots, each comprising ∼1000 triple events.

value of 174°, beginning at 170° for the (1,1,1) channel and ending at about 177° for the (2,2,2) channel. This narrowing trend agrees qualitatively with Hishikawa *et al* [77], whose results indicated that multiply charged parent ions have a half maximum deviation from the linear geometry, σ, determined to be $\sigma = 45 - 35°$ for CO_2^{z+} charge states of $z = 4 - 6$.

The bond length distribution for the six explosion channels is shown in figure 4.6. The distributions peak $\sim 2R_{eq}$ – $3R_{eq}$, but there is no clear relationship between bond length and charge state. The recovered bond length distributions have good agreement with the distributions of Bryan *et al* [82] and Cornaggia [51], particularly for the singly charged carbon channels. There is somewhat variable agreement with the results of Hishikawa *et al* [77], who reports shorter bond lengths than were seen in other experiments. We observe additional structure not previously visible because all previous techniques rely on fitting a triangular or Gaussian curve to describe their data. While this observed structure may be due to somewhat low statistics (particularly for the (1,2,2) channel which has $\sim 10^3$ events), the current technique should be more sensitive because in other techniques the structure is drowned out by the contribution of other channels. In particular, the shape of the

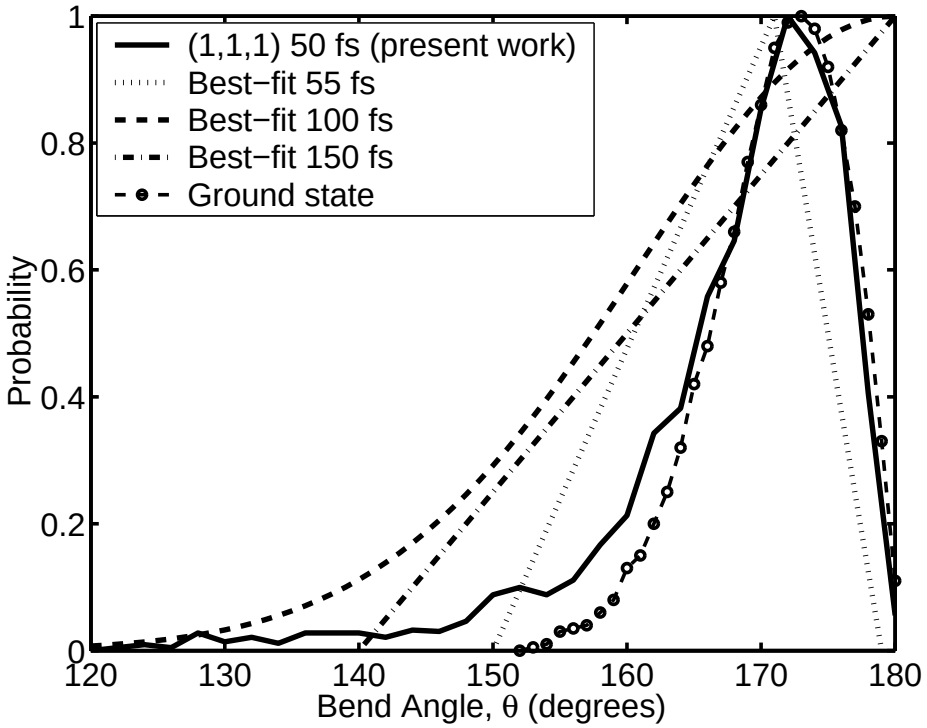

Figure 4.4: Bend-angle (θ) distribution (degrees) obtained from (1,1,1) explosion channel (solid line). For comparison, the θ distribution from [82] is also included where the laser pulse was 55 fs (dotted). Also included for comparison are results from [77] (100 fs, dashed) and [51] (150 fs, dot-dash). Finally, the ground state bond angle distribution is included [129] (dashed with circles). Adapted from [82].

(1,2,1) distribution is interesting as it shows a double-peak structure.

4.5 Discussion

We begin by examining the discrepancy in bend angle distributions determined by our experiment with those reported previously. Previous techniques relied upon incomplete momentum [51] or measurement of the momentum distribution from an ensemble [77]. In the latter case, correction for the momentum-dependent detector efficiency is crucial. This is because low momentum ions such as the carbon fragments from CO_2 can appear to have near zero momentum, indicating a 180° bend, if they are not ejected exactly along the detection axis. Although the method of [51] can resolve peak bend distributions less than 180° [52], the resolution clearly was not good enough to distinguish a peak in the angular distribution close to but not at 180°. Additionally, the requirement of all previous experiments to use a fitting procedure to simultaneously account for bend angle, bond length and molecular alignment will have made bend angle accuracy low close to 180°. The

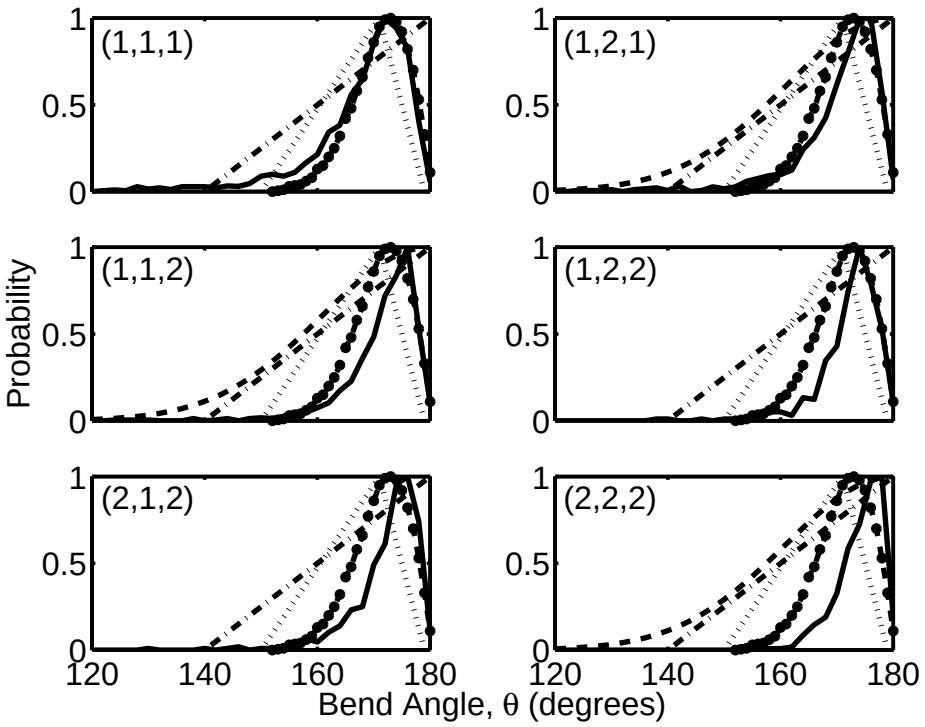

Figure 4.5: Bend-angle (θ) distribution (degrees) obtained from the six explosion channels. The results of this work are shown with a solid line. For comparison, the θ distribution from [82] is included (dotted line) as well as the distribution from [51] (dash-dotted line) and from [77] (dashed line). The ground state distribution is also included on each plot [129] (dashed with circles).

corrected momentum mapping technique of Bryan *et al* [82], which does attempt to account for the detection efficiency, records a peak in angular distribution close to ours in the case of the (1,1,1) channel. However, the technique of [82] does underestimate the bend angle for higher charge states and ensemble fitting is again the most likely cause of discrepancy.

Previous work with sub-7 fs pulses has shown the tendency for molecular geometry to be more accurately recovered from higher charge states due to these states's potential energy surfaces closely resembling a purely Coulombic repulsion [95]. We might expect this would also hold for our long pulse experiment but this would neglect the molecular dynamics during dissociation of the molecule. Assuming that the final ionization takes place at the peak of the laser pulse, for each channel, the molecule from the (1,1,1) channel will spend the most time in a bound ionization state, either CO_2^{2+} or CO^{2+} [130]. The theoretical work of Kono *et al* [93] suggests that structural deformation occurs in charge states as low as CO_2^{2+}, and that elongation of the C-O bond is accompanied by bending of the molecular skeleton. Evidence for this interesting phenomenon has been experimentally observed [84]. This tendency for the molecule to bend in these low states may be countered by the inclination of it to straighten as it undergoes linear dissociation on the (1,1,1) and

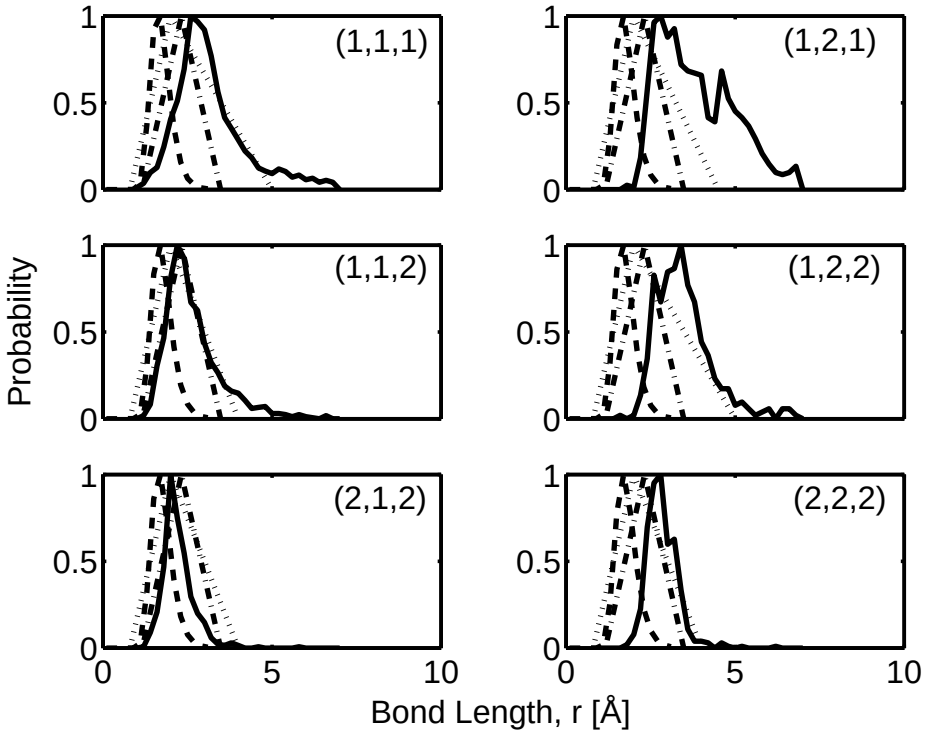

Figure 4.6: Bond length (r) distribution (Å) obtained from the six explosion channels. The results of the present work are shown with solid lines while results from Bryan *et al* [82] (dotted), Cornaggia [51] (dash-dotted) and Hishikawa *et al* [77] (dashed) are shown for comparison.

higher repulsive potentials. Higher charge states which spend less time in doubly or singly ionized levels will therefore appear straightened.

The recovered geometric structures in this work were generated by making the static Coulomb approximation. That is, fragment ions are assumed to have picked up no additional momentum during the multiple ionization process. A refinement to the calculation [131] attempts to account for this additional momentum using a two-step calculation. In the first step, the geometry is calculated using the static Coulomb approximation. Then, assuming a 50 fs interaction time, we account for the momentum picked up during the observed deformation. This momentum is subtracted from the initial measurements and the corrected geometry is calculated. This typically small correction is then used to recalculate the explosion geometry, and leads to bond lengths only slightly longer than observed and bend angles slightly smaller than those recovered using the static Coulomb approximation. The bend angle result of this calculation for the (2,2,2) channel is shown in figure 4.7. The implication is that where we use the static Coulomb approximation, we underestimate the amount of bending. In all observed channels above (1,1,1), this correction should shift the observed distribution closer to that of the ground state.

Our triple coincidence measurements have allowed us to resolve variation in kinetic energy release as a function of channel. We have also seen structure in

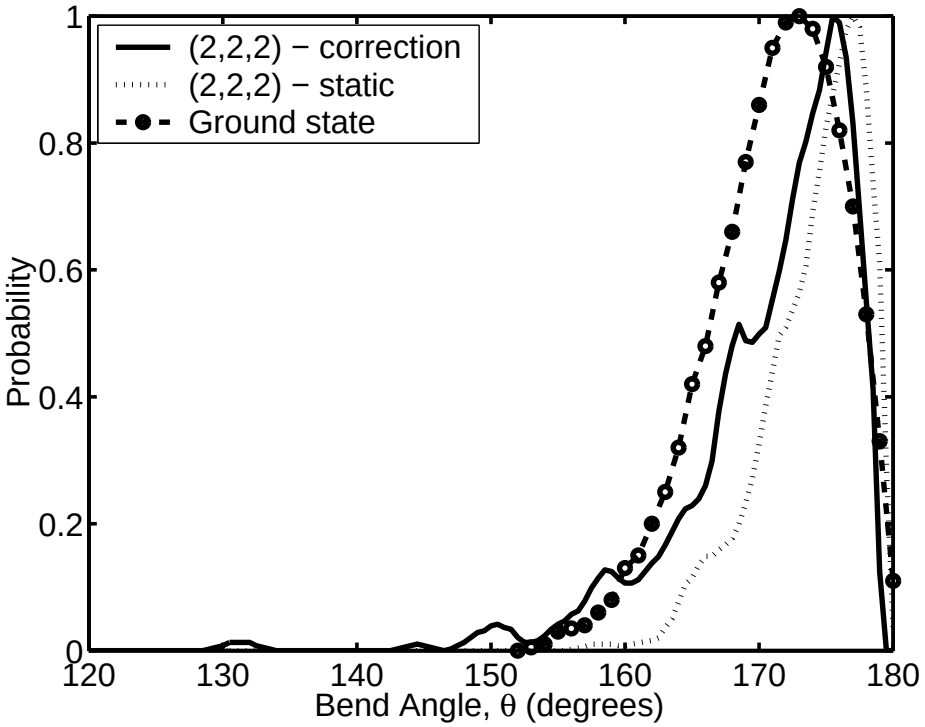

Figure 4.7: Bend-angle (θ) distribution (degrees) obtained from the (2,2,2) explosion channel. The results of this work using the static Coulomb approximation are shown with a dotted line while the corrected results are shown with a solid line. The ground state distribution [129] is shown with a dashed line with circles.

the kinetic energy distribution not previously observed. The underlying pattern suggests that kinetic energy increases more with oxygen ionization than with carbon ionization. This is manifested as a decrease in bond length when oxygen doubly ionizes. However, when carbon doubly ionizes there is almost no change in bond length. In addition, we must account for the appearance of structure in the energy spectrum of channels such as (1,1,1) and (1,2,1). We will now examine these phenomena in terms of a classical enhanced ionization picture [54] and the recent discovery of the importance of excited atomic ions derived from laser induced Coulomb explosion of small molecules [132, 133, 134].

As in the case of OCS [131, 135] and CO_2 [136] we modify the diatomic code of Posthumus *et al* [54] to model a heteronuclear triatomic molecule in a DC field. Rather than averaging the molecular charge we set the core charges equal to the post-dissociative fragments of the channel under investigation. Figure 4.8 shows the result of these calculations, with the difference in critical distance for successive curves tabulated. The absolute magnitude of the critical distance is larger than observed in our experiment and has a general trend toward lower bond length for higher charge state, as observed for OCS [131]. Recently, it has been shown that systematic modifications to the ionic charge values used for the calculation can

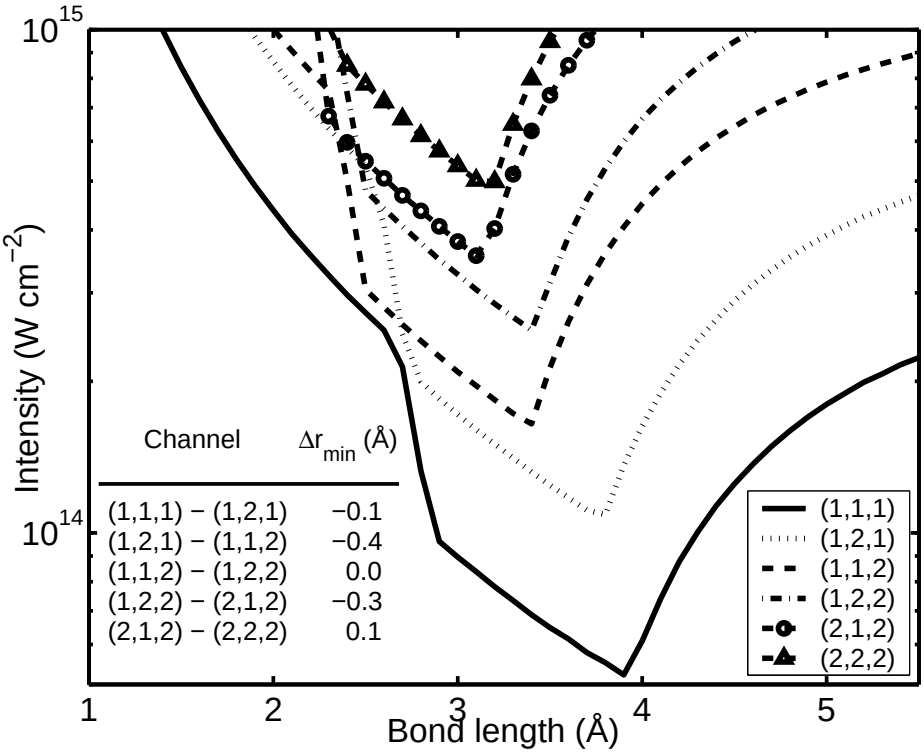

Figure 4.8: Ionization laser intensity as a function of bond length for the six channels under investigation, modeled using the classical enhanced ionization theory of [54]. In order of increasing intensity, the channels are: (1,1,1), solid line; (1,2,1), dotted line; (1,1,2), dashed line; (1,2,2), dash-dotted line; (2,1,2), dashed line with circles; (2,2,2), dashed line with triangles. The inset table shows the bond length difference at the minimum of each channel.

reproduce the experimentally observed trend [135] in the case of OCS. This reduction in charge is physical as it mimics the effect of deviation from pure Coulombic of the ion interaction potentials for low charge states [137]. Beyond this general trend to shorter bond lengths, there is a startling qualitative correlation between the way R_C changes depending on whether a carbon or an oxygen is ionized further. It should be noted that these transitions are not indicative of sequential states of ionization. Rather, it is the change from the (1,2,1) to the (1,1,2) and from the (1,2,2) to the (2,1,2) channels that gives rise to a much larger reduction in R_C than any other transitions. All other steps are either close to zero or slightly positive as observed experimentally. We therefore attribute these observations to effect of enhanced ionization.

While theoretical work has been done on the fragmentation pathways of CO_2^{2+} [138, 139, 140], little information is available for the potential energy surfaces of higher charge states. However, for the lower charge states, there are several pathways that can lead to dissociation, each of which lead to ionic fragments in different excited states. This multi-path dissociation should follow for higher charge states

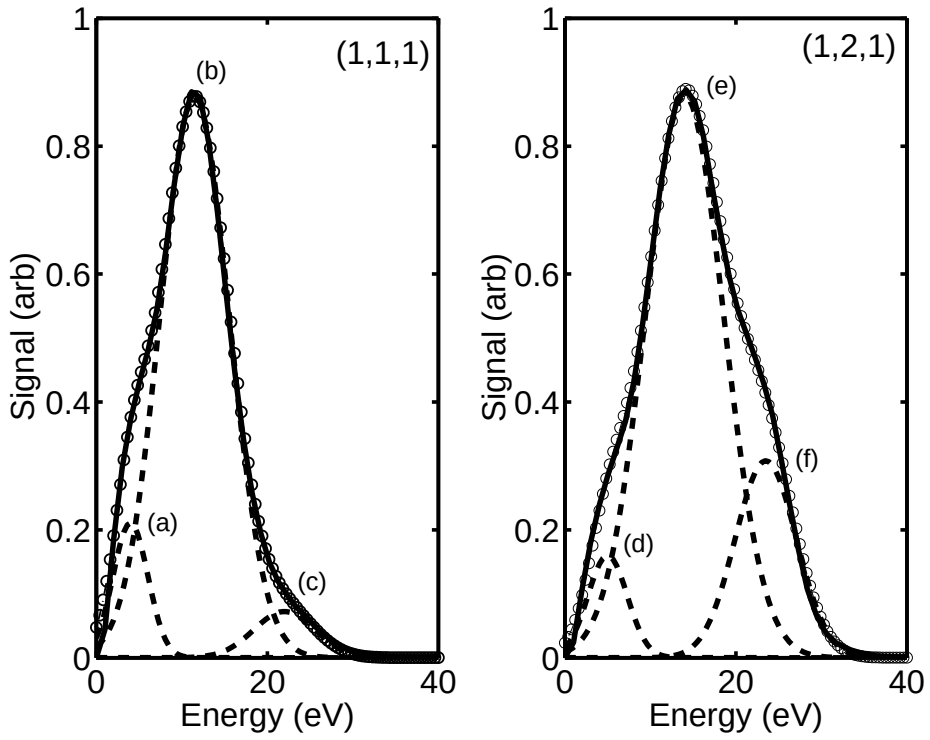

Figure 4.9: Kinetic energy spectra for the (1,1,1) and (1,2,1) channels, shown with solid lines, smoothed using a three-point triangle filter. Each spectrum has been deconvolved into three Gaussian peaks (dashed), the sum of which is shown with circles. The energy values for the six peaks are: (a) 4 eV; (b) 11.5 eV; (c) 22 eV; (d) 5 eV; (e) 14 eV; (f) 23.5 eV.

as well. Therefore, the structure in the kinetic energy spectra may be explained by considering the molecular ions dissociating into one or more excited atomic ions as was previously done for N_2 and O_2 [57, 132].

If we consider the kinetic energy spectra of the (1,1,1) and (1,2,1) channels, each spectrum can be deconvolved using three Gaussian peaks. Since excited fragments have less kinetic energy than fragments in the ground state, we can make reasonable guesses as to the identity of spectra peaks. In particular, we look for atomic transitions that will sum to the observed energy differences, giving preference to transitions that are of lower energy. For the (1,1,1) channel, the high energy peak, labeled (c), corresponds to each ion's ground state, $O^+(^4S)$ + $C^+(^2P)$ + $O^+(^4S)$. The next lowest peak, labeled (b), corresponds to ejection of two 5.02 eV oxygen ions in the (^{2}P) state or to ejection of two 3.32 eV oxygen ions in the (^{2}D) state with a 5.33 eV carbon ion in the (^{4}P) state. Finally, the lowest energy peak (a), corresponds to ejection of two (^{2}P) oxygen ions as in (b), as well as a 9.28 eV carbon ion in the (^{2}D) state. A similar analysis can be performed with the peaks in the (1,2,1) spectrum. If we again identify the highest energy peak (f) as the ground state, $O^+(^4S)$ + $C^{2+}(^1S)$ + $O^+(^4S)$, the middle peak (e) once

again corresponds to ejection of two 5.02 eV oxygen ions in the (^{2}P) state or to ejection of two 3.32 eV oxygen ions in the (^{2}D) state with a 6.49 eV carbon ion in the (^{3}P) state. The lowest energy peak (d), corresponds to ejection of two (^{2}P) oxygen ions and a 6.48 eV (^{3}P) carbon ion. Although the kinetic energy spectra of the higher channels show interesting structure, the statistics are inadequate to permit this analysis. While the exact identification of the final excited states is unclear, the excited state fragmentation model [141, 142] adequately describes our experimental results.

4.6 Conclusion

A triple coincidence imaging technique has been used to investigate dynamics of molecules as they interact with intense laser fields. The channel-resolved kinetic energy distributions show a step-wise KER increase and the resultant change in bond length can be interpreted using the classical enhanced ionization model. However, we observe structure in the kinetic energy distributions which we attribute to the presence of excited states in the fragment ions. The successful application of these two individual models suggests the possibility to combine the theories of excited state fragmentation and enhanced ionization into a single, simple model that can predict the behaviour of multielectronic molecules dissociated in ultrashort pulses.

Chapter 5

Concerted and Sequential Multielectronic Dissociative Ionization of CS_2 in an Intense Laser Field

5.1 Introduction

Carbon disulfide (CS_2) is a linear, triatomic molecule of much interest [143, 34, 87, 88, 144, 145]. In the ground electronic state, $X^1\Sigma_g$, the equilibrium C–S bond length is 1.55 Å with a bending-mode frequency of 397 cm^{-1}. The electronic configuration of the ground electronic state is $(core)^{22}(5\sigma_g)^2(4\sigma_u)^2(6\sigma_g)^2(5\sigma_u)^2(2\pi_u)^4(2\pi_g)^4$. During a laser-molecule interaction, it is expected that the CS_2 molecules will have the carbon atom displaced from its equilibrium geometry by the bending-mode vibrational motion, the lowest energy mode. The most probable value of the bend angle in the $v = 0$ level is 175.2°. Since our experiment was conducted at room temperature, where approximately 23% of the population will be in the $v = 1$ vibrational level with a most probable bend angle of 171.7° [34], we expect to measure a mean bend angle somewhere near 174°. Highly charged ion studies [34] have shown that the measured kinetic energy release (KER) values in higher charge states are approximately the same as those predicted by a pure Coulomb explosion. However, these same studies showed that the bend angle is shifted towards smaller values, that is, the molecular skeleton is bent, possibly due to excitation in the bending mode of the precursor molecular ion. Furthermore, the degree of bending depends upon the ionization channel achieved. For symmetric channels, where the sulfur ions have the same charge, the recovered bend angle was reported to be $\sim 170°$. In the case of asymmetric channels, the mean bend angle was typically $\sim 165°$. Non-coincident laser-initiated Coulomb explosion studies of low charge states [87] have shown substantial deformation occurs along the bending mode. While momentum imaging of higher charge states has shown that substantial bending can

be initiated in the neutral by pumping the parent molecule with a non-resonant, linearly polarized pulse (1064 nm, 7 ns, 414 mJ) before probing with an intense, circularly polarized pulse (795 nm, 100 fs, 0.3 mJ) [80]. Molecules that were probed without the ns pulse did not exhibit a strongly bent character. Throughout this paper, we will discuss ionization channels according to the convention $SCS^{(m+n+p)+} \rightarrow S^{m+}+C^{n+}+S^{p+}$, and refer to this as the (m, n, p) channel.

5.2 Experimental

The experimental apparatus has been described in greater detail in a previous chapter. The spectrometer extraction field was set to 180 V cm^{-1}. CS_2 vapor enters the chamber effusively through a leak valve and the experimental pressure is set to 1.5 x 10^{-8} Torr. Software is used to discriminate events after collection and only explosion events where three ions hit the detector in coincidence are retained. The data is filtered again to suppress false coincidences, defined as when the sum of the observed momenta, $\sum \mathbf{p}$, exceeds 10^{-22} kg m s^{-1}.

5.3 Results

5.3.1 Coulomb explosion of CS_2

At the present laser intensity, charge states up to CS_2^{13+} can be achieved. We focus attention on the formation and fragmentation of the highly charged CS_2^{z+} molecular ions by monitoring channels that result in three fragment ions. Several explosion channels were recorded with $10^3 \sim 10^4$ triple coincidence events in each channel. A useful parameter for correlating fragment ions is the χ angle, defined as the angle between the momentum vector of the carbon ion and the difference of the momentum vectors of the two sulphur ions. The χ angle is calculated according to

$$cos\chi = \frac{\mathbf{p_C} \cdot (\mathbf{p_{S_1}} - \mathbf{p_{S_2}})}{|\mathbf{p_C}||\mathbf{p_{S_1}} - \mathbf{p_{S_2}}|} \tag{5.1}$$

Physically, the angle χ indicates the direction of the outgoing carbon ion with respect to the line joining the S–S nuclei. In a symmetric fragmentation channel, where each sulphur ion has the same charge, the angle χ is indicative of whether or the not the dissociation process is sequential or concerted. In the event of a perfectly concerted Coulomb explosion, $\mathbf{p_{S_1}} = \mathbf{p_{S_2}}$ and $\chi = 90°$. However, if the bond lengths are unequal, or the sulphur ions have unequal momenta, $\chi \neq 90°$. The experimental χ distribution of the (3,2,3) channel is shown in figure 5.1(a), and while the most probable value is 90°, the standard deviation is $\sigma = 30°$, indicating some mixture of concerted and sequential processes. During asymmetric processes, the most probable value of χ should not be 90° due to the differing recoil velocities

of the fragment ions. In [34], the most probable values of χ were reported to be 95°–110°. Adopting the same definition, the χ distribution for the (2,2,3) is plotted in figure 5.1(b). As can be seen, the most probable value for χ is approximately 100°. Using a classical model, the χ angle of the (3,2,3) and (2,2,3) channels can be predicted by assuming a variety of initial bend angles, θ, and bond lengths, $r_{1,2}$. We assume that the Coulomb explosion proceeds by instantaneous multiple ionization, with all fragment ions initially at rest. The effect of sequential ionization is built into the model by allowing the bond lengths r_1 and r_2 to be different. The results of this calculation are shown in figure 5.2. For the (3,2,3) channel, for bend angles near to the zero-point bend angle $\theta_0 = 175.2°$, we expect to see $\chi \sim 70°$–$110°$ (due to symmetry about $\chi = 90°$), depending upon the degree of sequential ionization. In the case of the (2,2,3) channel, for bend angles near to the zero-point bend angle $\theta_0 = 175.2°$, we expect to see $\chi \sim 60°$–$120°$, once again depending upon the degree of sequential ionization. Thus, we have good agreement with the most probable value of the observed χ distribution. Moreover, we expect to see strong sequential character in the recovered molecular geometries.

Once the explosion channel and momentum of each fragment are known, the KER for each Coulomb explosion can be calculated by summing the kinetic energy of each fragment according to $\sum \mathbf{p}_i^2/2m_i$. Table 5.1 lists the mean KER for each of the measured channels and comparison with previous highly charged ion results [34] and ultrafast laser Coulomb explosion results [87, 80]. Our results are lower than [87] but compare well with [80]. Figure 5.3 plots the ratios of HCI KER from [34] and from this work for a series of fragmentation channels. As a consequence of the short interaction time, HCI experiments produce KER values similar to those predicted by Coulomb repulsion of the ionic fragments from their equilibrium geometry. By contrast, CEI experiments performed with laser pulses in the the 10–100 fs regime produce KER values indicating bond lengths 2–3 times larger than equilibrium due to enhanced ionization. Since KER is inversely proportional to the bond length, we expect to measure $\mathrm{KER}_{HCI}/\mathrm{KER}_{CEI} \sim 2$–3. Almost all of the observed channels fall into the expected range.

Figure 5.4 shows the likelihood of a molecular ion in a particular charge state to fragment into a symmetric or asymmetric channel. Symmetric channels are those where the charge on the sulphur ions is the same, such as (2,3,2). Asymmetric channels are those where the charge on the sulphur ions is different, such as (2,1,4). As discussed in the HCI experiment [34], the energy involved in the fragmentation plays a large role in determining the branching ratio of a channel. For $q \leq 10$, our data in figure 5.4 can be directly compared with data from [34] which has been rescaled onto the same scale. For $q \leq 8$, the agreement is excellent, despite the differing method of initiating Coulomb explosions. For higher values of q, the statistics of [34] are somewhat low and comparison becomes problematic.

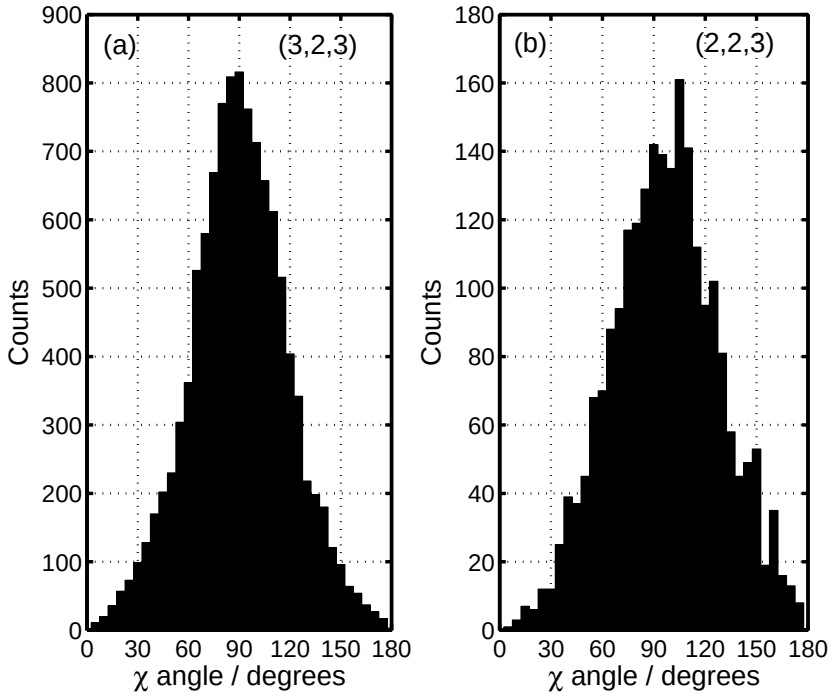

Figure 5.1: Histogram of the reconstructed χ angle distribution for the (a) (3,2,3) and (b) (2,2,3) Coulomb explosion channels of CS_2. For the (3,2,3) channel, the most probable value of χ is $\sim 90°$, indicating some degree of concerted fragmentation. Given that the standard deviation is $\sigma \sim 30°$, the distribution is somewhat wider than was reported in highly charged ion experiments [34], where $\sigma \sim 15°$ in the (2,2,2) channel. The (2,2,3) channel has the χ distribution peaked $\sim 100°$, with a wide distribution indicating sequential fragmentation processes.

5.3.2 Molecular geometry reconstruction

With the three-dimensional momentum vectors of the fragments determined, reconstruction of the molecular geometry just prior to Coulomb explosion is straightforward. The momentum of the ion fragments is calculated by numerically solving the classical equations of motion in the Coulomb field for some initial set of guesses at the molecular structure. Here it is assumed that the initial momentum of the molecular fragments is zero. The parameter space defined by this set of guesses is explored by a simplex algorithm [122] until the observed asymptotic momentum vectors are reproduced. A more computationally demanding approach utilizes an *ab initio* potential energy surface [95]. We use the Coulomb approximation to better compare with previous results [87, 34] and because for highly charged fragmentation, theoretical calculations utilizing the Coulomb approximation reproduce the experimental result quite well [34], though are probably of limited use for intermediate ionization events.

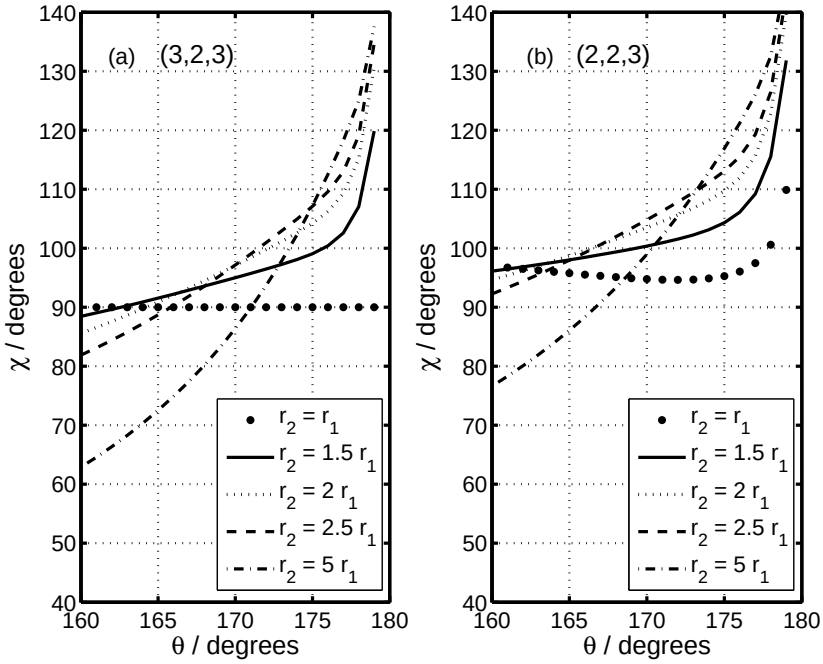

Figure 5.2: Theoretical χ angle for a given bend angle θ for the (a) (3,2,3) and (b) (2,2,3) channel. For the determination of χ, we are concerned only with the relative values of the two bond lengths. The case where $r_2 = r_1$ is plotted with large dots. Sequential ionization is investigated for the cases where $r_2 = 1.5\ r_1$ (solid line), $r_2 = 2\ r_1$ (dotted line), $r_2 = 2.5\ r_1$ (dashed line), and $r_2 = 5\ r_1$ (dash-dotted line). Note that in the case of the (2,2,3) channel, the S^{2+}–C^{2+} bond length is defined as r_1, while the C^{2+}–S^{3+} bond length is defined as r_2.

Channel-resolved histograms of mean bond length and bend angle are shown in figure 5.5 and the bend angle distributions are compared with theoretical zero-point calculations from [34] and, in the case of (3,2,3), the recovered distribution of [80]. The peak of the mean bond length distribution for each channel is in the range of 3 – 4.5 Å($\sim 2.2R_{eq}$ –3 R_{eq}), a reasonable result given our laser pulse length is where EI dominates. Hasegawa *et al.* [87] report a mean bond length of only $r = 2.5$ Å for CS_2^{3+}, using laser pulses similar to ours. By contrast, Iwasaki *et al.* reported a bond length of 3.1 Å for the (3,2,3) fragmentation channel, which, while shorter than our result, is still within the range predicted by EI.

The most probable bend angle from the recovered geometries is $\theta = 175° - 179°$. The (2,2,2) and (3,3,3) fragmentation channels each have a bend angle distribution similar to that of the neutral molecule's $X^1\Sigma_g$ ground state. There is a general trend towards straightening of the molecule as charge state increases, particularly in the case of the (4,1,4) channel. As a general trend, we observe that explosion channels with a carbon charge that is lower that the sulfur charges appear straighter

Fragmentation Channel	KER (eV)	100 fs (eV)	60 fsF (eV)	HCI (eV)
(1,1,1)	9.3		15.3	19.0
(1,1,2)	11		22.4	37.1
(1,2,1)	20			
(1,2,2)	21			59.6
(2,1,2)	23			56.6
(2,1,3)	39			73.9
(1,2,3)	23			93.4
(2,2,2)	41	44		90.7
(3,1,3)				90.5
(2,1,4)	41			108
(2,2,3)	44	53		118
(2,3,2)	50			125
(3,1,4)				113
(2,2,4)	60	63		134
(2,3,3)	50			139
(3,2,3)	63	67		153
(4,1,4)	95			140
(3,2,4)	62			146
(3,3,3)	80			180
(3,3,4)	99			165
(4,2,4)	88			180
(3,4,3)	92			
(5,1,5)	86			
(3,4,4)	97			
(4,3,4)	120			
(4,3,5)	85			
(4,4,4)	154			
(4,4,5)	92			

Table 5.1: Mean kinetic energy released (KER) in eV, measured upon fragmentation of CS_2^{q+} molecular ions. Included for comparison are other ultrafast results (100 fs [80], 60 fs [87] and HCI results [34]. Note that the technique used in [80] is not channel resolved and the listed KER have been computed from the appropriate fragment momenta.

with a bend angle distribution narrower than predicted by theory. These results are somewhat different than were reported in the HCI experiments [34], which measured slightly more bent geometries with a wider distribution for the (2,2,2) and (3,1,2) fragmentation channels. Furthermore, for the fragmentation of CS_2^{3+}, Hasegawa *et al.* [87] reported a much more distorted molecular skeleton, with a mean bend angle of $\theta = 145°$ and a standard deviation of $\sigma = 27°$. In studies of CS_2^{8+}, Iwasaki *et al.* [80] reported a most probable bend angle of 180° with a half-width of $\sim 9°$ in the absence of a ns pump pulse. Although we do not measure a most probable angle of 180° for our (3,2,3) channel, our half maximum bend angle value is $\sim 171°$, giving an angular range similar to that seen in [80].

An interesting observation is made by comparing the results of figure 5.1 and figure 5.5 with those of figure 5.2. Since the recovered bend angle distribution gives a range of $\theta \sim 170 - 179.5°$, we might infer from the χ distribution in figure 5.1

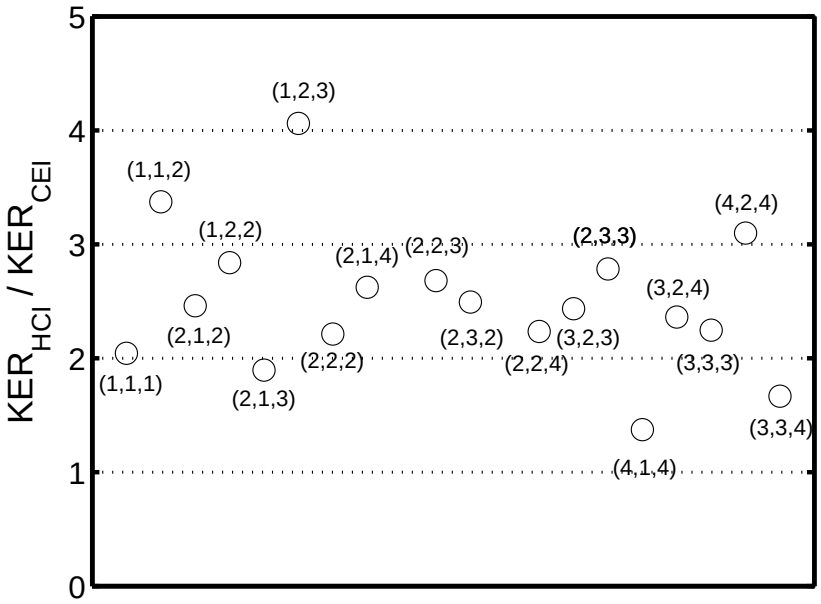

Figure 5.3: Ratio of KER measured in previous HCI experiment [34] to this work for indicated channels. Assuming enhanced ionization adequately describes molecular fragmentation from our $\sim$ 50 fs laser pulses, we expect a ratio of 2–3.

and bond lengths given in figure 5.2 that (3,2,3) fragmentation proceeded from not only concerted processes where $r_1 = r_2$, but also sequential processes where $r_1 < r_2$ (or vice versa). However, as figure 5.6 clearly shows, sequential processes dominate the recovered geometries from the (3,2,3) channel, suggesting two extreme breakup scenarios. In the first extreme case, both C–S bonds symmetrically stretch to 2–4 Å before fragmentation. The second scenario is sequential breakup where one C–S bond stretches to as large as 15 Å. Approximately 17% of all events are concerted.

Figure 5.7 plots the bend angle versus the mean bond length for the (3,2,3) channel. Two plots are made according to the ratio of $\frac{r_1}{r_2}$. Figure 5.7(a) plots geometries where $\frac{3}{4} \leq \frac{r_1}{r_2} \leq \frac{4}{3}$. In this case, the bending amplitude is as large as 162°. Figure 5.7(b) plots geometries where $\frac{r_{1,2}}{r_{2,1}} \geq 3$. In this more likely case, one of the bonds will be much larger than the other, and the molecular skeleton will be almost straight.

5.4 Discussion

We begin by examining the discrepancies in our measured bond lengths and bend angles with previously reported results. With regard to the bend angle, theoretical studies by Kono *et al.* [93] on CO_2 in intense laser fields indicates that structural

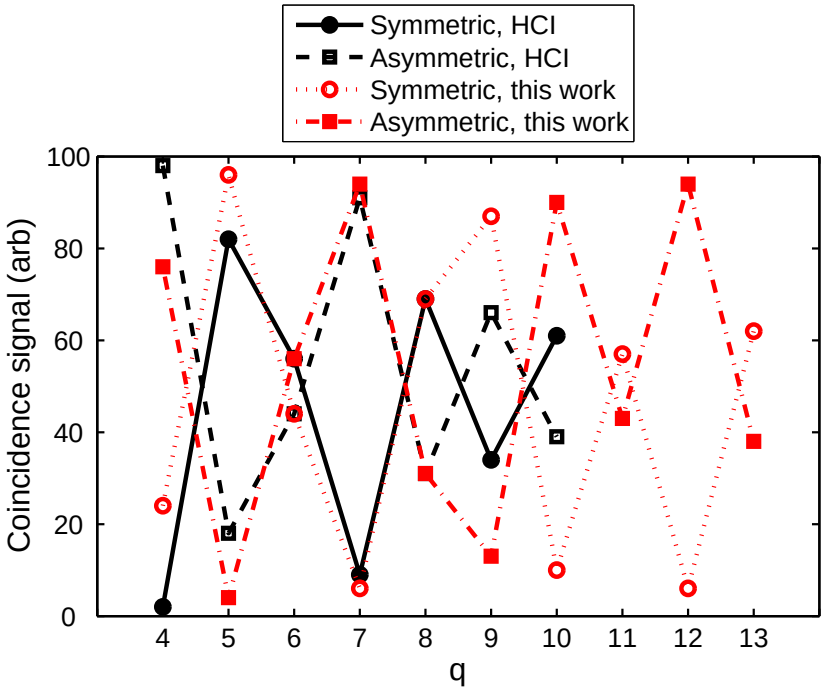

Figure 5.4: Previously reported [34] likelihood for fragmentation into symmetric (black filled circles with solid lines) and asymmetric channels (black open squares with dotted lines) for different molecular charge states q in HCI experiment. The results of [34] have been rescaled so that each molecular charge state (CS_2^{q+}) has been normalized. The results of this work are shown in red (symmetric are open circles with dotted lines, asymmetric are filled squares with dash-dotted lines). Symmetric channels are those where the sulphur ions have identical charge. Conversely, the sulphur ions have different charges in asymmetric channels.

deformation occurs primarily in the doubly charged state CO_2^{2+} where elongation of the molecular bond is accompanied by bending. Indeed, studies of CS_2^{3+} [87] and N_2O^{3+} [90] have reported this to be the case. Based on figure 5.7(a), we see some evidence of geometries that are bend and stretched in (3,2,3) fragmentation channel. While the degree of bending is not as large as reported in HCI experiments [34], it is clear that bending has occurred. Furthermore, the bond lengths are nearly symmetrically stretched to between 2–4 Å, within the range predicted by EI. The physical reason is inferred from [93]. Assuming that the final ionization takes place at the peak of the laser pulse, the lower channels, that is, (1,1,1) will spend the most time in a bound ionization state, such as CS_2^{2+}, where bending is energetically favourable. When these molecular ions fragment, they do so in a concerted process. The early onset of sequential dissociation of molecular ions that fragment into (3,2,3) for instance does not permit coupling of the bending mode with the laser field. Therefore, highly charged channels appear straightened. This also explains the linear geometry previously seen by Iwasaki *et al.* [80] in the study

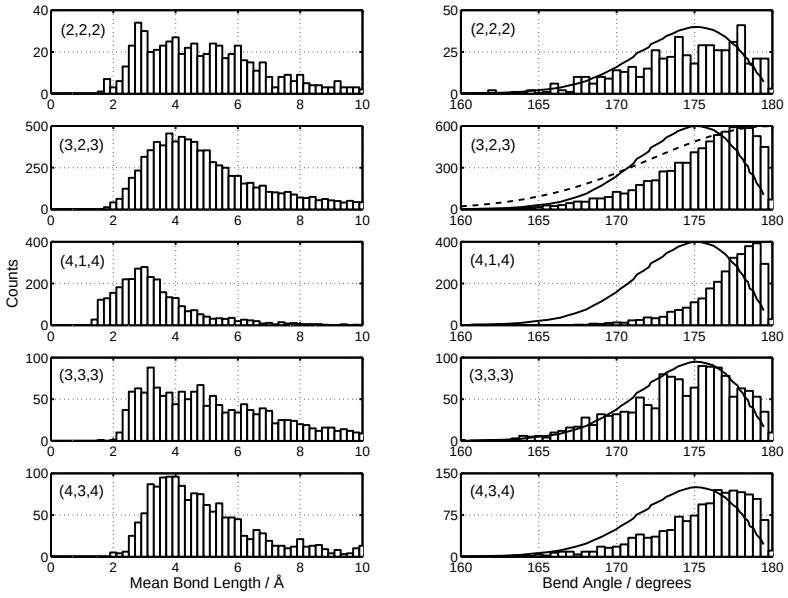

Figure 5.5: Channel-resolved mean bond length and bend angle distributions. The bend angle distributions on the right include the zero-point distribution of the neutral CS_2 molecule computed in [34] (solid line). The (3,2,3) channel also includes the recovered bend angle distribution from [80] (dashed line).

of CS_2^{q+}, q= 6–8.

The temporal shape of the laser pulse suggests another explanation. A temporal pulse with significant wings (as measured in our interferometric autocorrelations) can initiate ionization and single dissociation before the peak of the pulse further ionizes and dissociates the fragments. Unlike CO_2, CS_2 has a low single ionization potential and is more likely to be ionized by a pre-pulse. This would explain the discrepancies in the other experimental results as being due to pulse shape and pulse length effects. The straight molecules observed by Iwasaki *et al.* [80] were most likely the result of wings on their pulse, but their ensemble type of measurement did not allow this to be identified as due to sequential dissociation. Notably, Hasegawa *et al.* [87] reported observing bent low charged CS_2 molecules. These bent molecules could originate from regions of the focus where the peak intensity is not particularly high. Consequently, the energy in the wings of the pulse would not be high enough to initiate sequential processes early on.

The two distinct regimes evident in figure 5.7(a) and (b) suggest two fragmentation processes. Approximately 17% of the total population can be described as concerted, with $r_1 \sim r_2$, while the remainder are sequential. Referring to figure 5.4, it is interesting to note that in the $q = 4$ case, approximately 25% of the population will fragment into the (1,2,1) channel while the remainder will fragment into the asymmetric (1,1,2) channel. The two regimes observed in the (3,2,3)

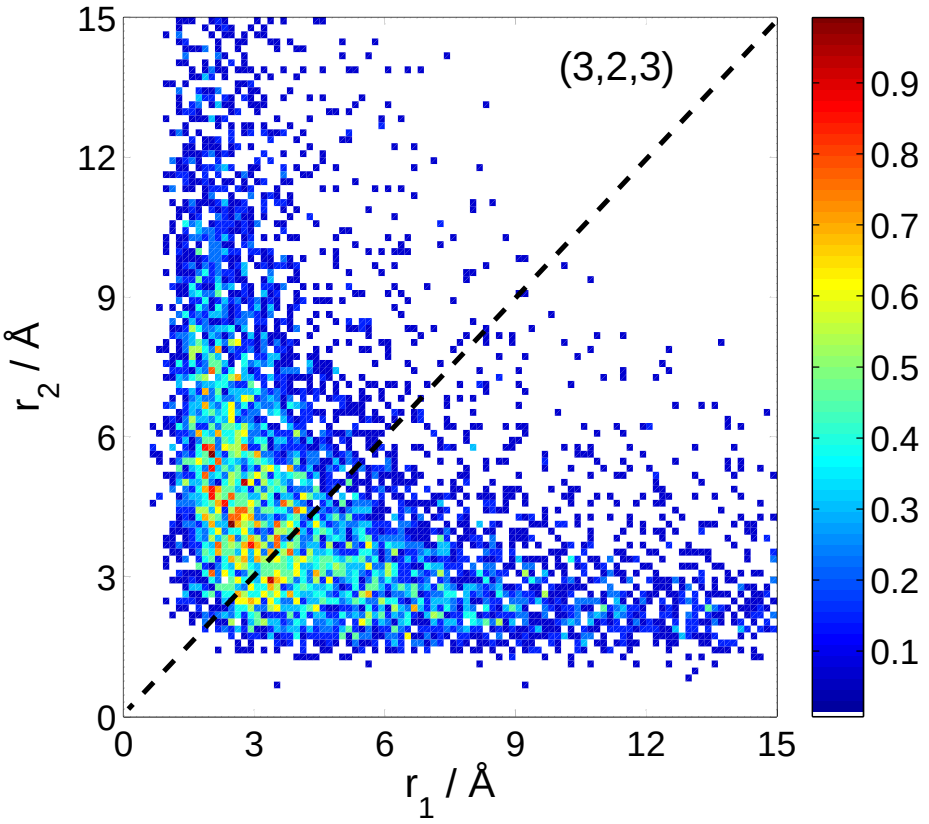

Figure 5.6: Point plot of r_1 versus r_2 from the recovered geometries of the (3,2,3) fragmentation channel. The concerted condition of $r_1 = r_2$ is indicated with a dashed line. The fragmentation of the (3,2,3) channel is dominated by sequential fragmentation processes although there is some concerted stretch character in the range of 2∼4 Å.

channel suggest that the precursor molecular ion formed during multiple ionization may strongly affect the final fragmentation channel. As previously stated, [58] have concluded that multiple ionization to high charge states in diatomic molecules should occur by asymmetric ionization and that signal from symmetric channels should be small. In the case of diatomics, highly charged molecular ions are produced by strong coupling of the laser field with the excited electronic state of the parent molecular ion. Furthermore, as the excited state can be correlated to the asymmetric dissociation channel of the parent molecule, ionization is considered to proceed preferentially through asymmetric processes. If the results of [58] can be extended to triatomic molecules, the additional freedom of the bending coordinate might provide an explanation for fragmentation via symmetric pathways.

Since we consider the geometric deformation of the CS_2 molecules to be the result of EI, we attempt to analyze these changes in bond length using a classical EI model [54]. As in the case of CO_2, we modify the code of Posthumus *et al.* [54] to model the concerted fragmentation of a linear triatomic molecule in a DC field.

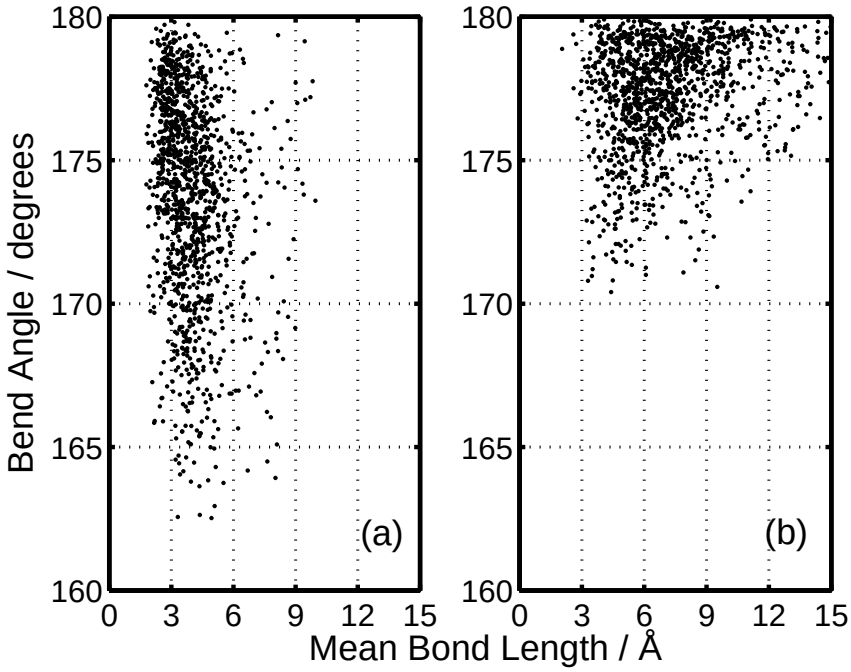

Figure 5.7: Bend angle versus mean bond length for the (3,2,3) channel. According to (a), bent geometries are usually produced when the bond lengths are short and ionization is concerted. Conversely, as in (b), when ionization proceeds sequentially, the geometry is almost linear.

This is a reasonable approximation since the model assumes a linear geometry and, as can be seen from the bend angle distributions, bending is slight. Furthermore, we expect that as more electrons are removed, the validity of the model should increase. We set the core charges equal to the post-dissociative fragments of the channels under investigation and allow the C–S bonds to stretch symmetrically. Figure 5.8 shows the result of these calculations. We see that for the (2,2,2), (3,2,3), (3,3,3) and (4,3,4) channels, there is some quantitative agreement between the observed most-probable bond length in figure 5.5 and the bond length predicted by the EI model.

5.5 Conclusion

We have used an ultrafast laser ion coincidence imaging technique to investigate the dynamics of molecules as they interact with intense laser fields. The χ angle distribution for both symmetric and asymmetric fragmentation channels suggests that a combination of concerted and sequential fragmentation occur. Based on the relative population of the concerted and sequential geometries in the (3,2,3) channel, we postulate the tendency for a molecular ion to fragment in a concerted

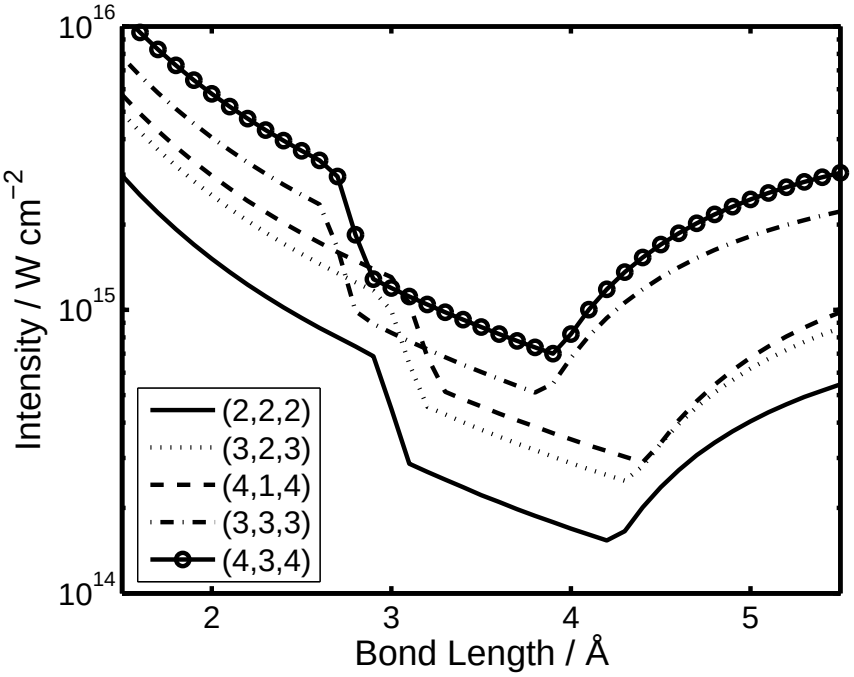

Figure 5.8: Ionization laser intensity as a function of bond length for the five channels under investigation, modeled using the classical enhanced ionization theory of [54]. In order of increasing intensity, the channels are: (2,2,2), solid line; (3,2,3), dotted line; (4,1,4), dashed line; (3,3,3), dash-dotted line; (4,3,4), dashed line with open circles.

fashion is influenced by the coupling of the laser field with the bending motion of the molecular ion at the beginning of the multiple ionization process. KER values were found to be significantly less than predicted from a Coulomb explosion from the neutral geometry, indicating molecular dynamics on the time scale of the laser pulse. However, the ratio of measured KER values to previous HCI results was in the range predicted by EI, indicating that a theoretical treatment of HCI may be compatible with the theory of field ionization.

Chapter 6

Comparison of ADK Ionization Rates as a Diagnostic for Selective Vibrational Level Population Measurement

This chapter is adapted from an article that was printed in *J. Phys. B: At. Mol. Opt. Phys.*, 39:3769-3779, 2006, produced in collaboration with Wing-Ki Liu, Asif A. Zaidi, Alexandre Trottier and Joseph H. Sanderson.

6.1 Introduction

The ready availability of femtosecond laser systems and the ability to control and manipulate the phase of their pulses has led to an increasing effort to use them as tools to control matter. One obvious property that might change with vibrational excitation is the ionization rate of a molecule. This dependence on vibrational level would be a consequence of the dependence of ionization rate on bond length. Recent work on H_2^+ [146, 147, 72] provides convincing evidence for strong bond length dependence on ionization rate, leading to a non-Franck-Condon distribution of product ions, although the observed deviation from a Franck-Condon distribution can also be explained by taking into account the intensity distribution of the ionization laser pulses [148]. Also, the phenomenon of enhanced ionization of molecular ions [55, 54] is now well established.

A previous attempt has been made to use ionization rate to diagnose vibrational excitation [149] using a simple over-the-barrier ionization (OBI) model, also known as the barrier suppression model [62, 150, 151]. Here we examine three molecular systems using a method based on the popular Ammosov-Delone-Krainov (ADK) tunneling approximation [59] for describing the ionization process. As Hanson [152] remarked, the tunneling rate is critically dependent upon the difference in the

neutral and ion electronic potentials, which varies as a function of the internuclear bond length R. This method, proposed by Saenz [146], calculates the ionization rate by averaging the ADK R-dependent rate over the probability amplitude of the vibrational state of the molecule.

The quantity that can be used as diagnostic for vibrational excitation of a molecule is the enhancement ratio of the ionization signal of the molecule in the vibrational state v to that in the ground vibrational state. Such ratios can be computed using the OBI in conjunction with focal volume considerations [62, 150, 149, 151]. We compare the enhancement ratios obtained by the ADK and the OBI methods for the H_2 molecule, and discuss the analysis for N_2 and CO_2.

6.2 Molecular Systems

Simple diatomic molecules are the most appropriate systems to study as their vibration is in only one dimension. H_2 and N_2 represent diatomic molecules whose ionization potentials vary substantially (H_2) or very little (N_2) with internuclear distance. For triatomic molecules, the additional degrees of freedom greatly complicate the situation. Here we have considered the symmetric stretch of CO_2 and consider only this normal mode, ignoring other vibrational degrees of freedom. This was done for two reasons. First, by considering only the symmetric stretch mode, the vibration of CO_2 can be treated in the same way as a diatomic system. Second, in previous work [149], it was the symmetric stretch mode which was believed to be preferentially excited. For the diatomic systems, the potential energy curves of the neutral and ion species were obtained from the literature [153, 154]. For CO_2 and CO_2^+, potential energy surfaces (PES) for nuclear motion were calculated from the variational data of Zuniga et al. [155] and Brommer et al. [156]. Cuts were then taken through these PES along the symmetric stretching coordinate ($R_{CO_1} = R_{CO_2}$). Thus we ignore any anharmonic coupling to other normal modes of vibration. The potential energy curves for N_2 and CO_2 are shown in figures 6.1 and 6.2.

In the presence of an intense laser field, the electric field of the laser will couple with the electric dipole of the molecule and can modify the potential energy curves. This laser-induced bond softening has the effect of reducing the potential energy gap between the neutral energy level and the ground electronic state of the ion at large R values. The case of H_2^+ is well-known [150, 151, 157]: the ground and excited state potential curves will distort according to

$$V_{1,2} = \frac{1}{2}(V_g + V_e) \mp \frac{1}{2}\sqrt{(V_e - V_g)^2 + 4V_{eg}^2} \tag{6.1}$$

where V_g is the potential energy of the $1s\sigma_g$ ground state, and V_e is the potential energy of the $2p\sigma_u$ repulsive excited state. V_{eg} is the dipole coupling between the ground and excited states, and for large R, $V_{eg} \approx \frac{1}{2}RF$ where F is the electric field

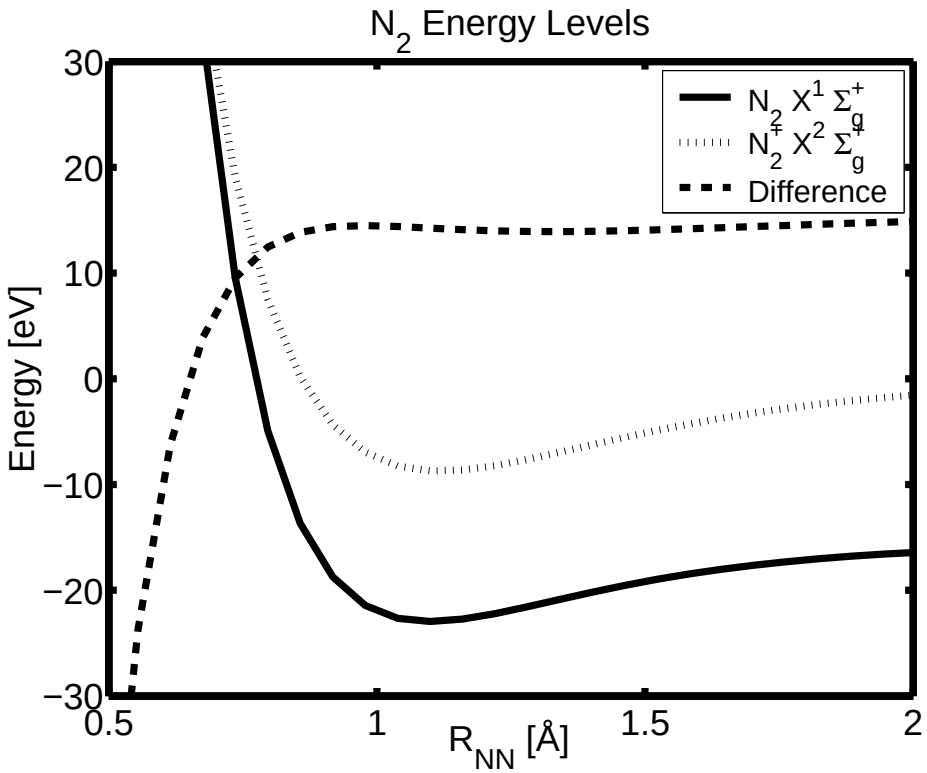

Figure 6.1: Ground-state potential energy curves of N_2 ($X^1\Sigma_g^+$, solid) and N_2^+ ($X^1\Sigma_g^+$, dotted). These curves were calculated based on [154]. Over the range of the vibrational levels of interest, the difference (dashed) in the potential energy curves is almost independent of vibrational level.

amplitude. V_1 will be the new lower potential energy curve and V_2 will be the new upper potential energy curve. Under the influence of the static field, the V_1 potential energy curve will not have as many bound vibrational levels as the V_g potential energy curve. As a result, vibrationally excited molecules will dissociate much more easily on V_1. This process is known as bond-softening. Recently, Saenz [158] presented three-dimensional *ab initio* calculation of the ionization rates and energy shifts of a H_2 molecule in a static electric field oriented parallel to the molecular axis, and demonstrated similar bond-softening effect for the neutral molecule. Unlike the H_2^+ case where the ground and excited states (the charge resonance states) become degenerate as $R \to \infty$, for the neutral molecule it is the energetically higher excited states with ionic characters and having the same symmetry as the ground state ($^1\Sigma$) that would couple by the electric field to the ground state, giving rise to curve crossings and the bond-softening effect. The incorporation of this effect is essential to successfully explain the results of recent observation on the vibrational excitation of H_2^+ in strong field ionization experiments of H_2 [146, 147, 72]. The bond-softening effect observed by Saenz [158] appears at a higher field intensity ($\geq 10^{14}$ W cm^{-2}) for the neutral H_2 molecule than the molecular ion ($\geq 10^{13}$ W cm^{-2}) [147]. In this paper we are concerned with laser intensities 10^{13} W cm^{-2} $< I < 10^{14}$ W cm^{-2},

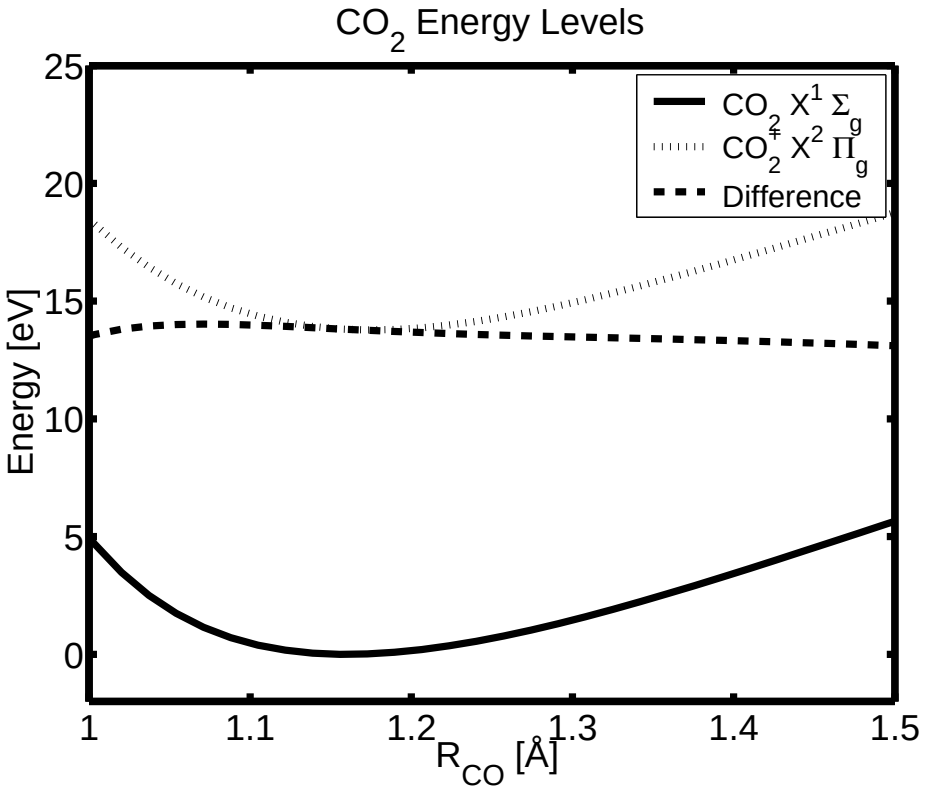

Figure 6.2: Ground-state potential energy curves of CO_2 (solid) and CO_2^+ (dotted) based on the data of [155] and [156] respectively. Here we have selected cuts along the symmetric stretch coordinate ($R_{CO_2} = R_{CO_2}$) of the potential energy surfaces. As with N_2, the difference (dashed) in the potential energy curves is largely constant over the range of interest.

and we ignore the bond-softening effect for the neutral molecules. For nitrogen and carbon dioxide, no *ab initio* calculation of bond-softening effect in the presence of a strong electric field exists to the best of our knowledge. However, the field-free potential curves for N_2^+ [159] indicate that the bond-softening effect will only become important at nuclear separations which are beyond the range of vibrational levels of interest here. For CO_2^+, the excited electronic states are separated from the ground state by several eV [160], and bond-softening effect is expected to become significant only at higher laser intensities [158]. Hence we ignore the effect of bond-softening for N_2 and CO_2 in this study. It will be desirable to have *ab initio* studies of bond-softening for these systems.

6.3 ADK Tunneling Ionization

Recall from a previous chapter that the ADK tunnel ionization rate, w_{ADK}, is given in atomic units by [59]:

$$w_{ADK}(R,I) = \left(\frac{3\mathrm{e}}{\pi}\right)^{3/2} \frac{Z^2}{n^{*9/2}} \left(\frac{4\mathrm{e}Z^3}{n^{*4}F}\right)^{2n^*-3/2} \exp\left(-\frac{2Z^3}{3n^{*3}F}\right), \tag{6.2}$$

where $\mathrm{e} = 2.718\ldots$, Z is the ionic charge, and $I = (c/8\pi)F^2$ is the laser intensity. The effective quantum number, n^*, is related to I_p, the ionization potential of the system, by

$$n^* = Z/\sqrt{2I_p(R)}. \tag{6.3}$$

Crucially, I_p varies with the internuclear separation R and we can calculate this using the technique described in [146, 147, 72], by computing the energy gap between the ground state neutral electronic level and the first ionization state. The difference in the potential curves in figures 6.1 and 6.2 gives the ionization energy as a function of bond length R for N_2 and CO_2. These ionization energy values were then inserted into the ADK formula to produce the ionization rate as a function of bond length.

Since we are interested in a technique that will act as a diagnostic for ionization as a function of neutral vibrational level population, we recast the above calculation to determine the ionization rate as a function of vibrational level in the neutral molecule.

A satisfactory method to calculate the vibrational dependence of the ionization rate is to average the R-dependent rate over the probability distribution of the molecule in R [146]. This is equivalent to calculating the expectation value of the ADK rate for a given vibrational state v described by the nuclear wave function $\Psi_v(R)$. For each vibrational level, $\Psi_v(R)$ was calculated using the computer program LEVEL [161]. In this case, the vibrationally averaged (VA) ionization rate becomes [146, 147]

$$w(v,I) = \int \mathrm{d}R |\Psi_v(R)|^2 w_{ADK}(R,I) \tag{6.4}$$

where $w_{ADK}(R,I)$ is given by equation (6.2).

We wish to compare results of the OBI model with the ADK calculations. In the OBI model [54, 150, 151], the multi-well potential experienced by the outer electron at $\boldsymbol{r}$ of a molecule in the presence of a static electric field $\boldsymbol{F}$ can be modeled by [54, 131]

$$U(r) = -\sum_{i=1}^{n_a} \frac{\overline{Z}}{|\boldsymbol{r} - \boldsymbol{R}_i|} - \boldsymbol{F}\cdot\boldsymbol{r}, \tag{6.5}$$

where n_a is the number of atomic ions of the molecule, R_i is the position vector of the ith atomic ion, and $\overline{Z}$ is the average nuclear charge of the atomic ions. The delocalized energy level of this electron is approximated by

$$\varepsilon_L = -\frac{1}{n_a}\sum_{i=1}^{n_a}\left[I_{pi} + \sum_{j\neq i}^{n_a}\frac{Z_i}{|R_i - R_j|}\right], \tag{6.6}$$

where Z_i and I_{pi} are the charge and ionization potential of the ith atomic ion, respectively. Thus, ε_L is the sum of the average ionization potential of the atomic ions and the average potential due to the Coulomb attraction of the neighbouring atomic ions. If any of the inner barriers within the well of $U(\boldsymbol{r})$ rises above ε_L, ε_L will be replaced by the Stark-shifted atomic level. Table 6.1 shows the ionization potentials ($-\varepsilon_L$) for several diatomic molecules (n_a=2) and CO_2 (n_a=3), in their equilibrium configurations, predicted by equation (6.6). The agreement is reasonable for diatomics and adequate for CO_2, given the simplicity of the model.

Molecule	Calculated $-\varepsilon_L$	Accepted $-\varepsilon_L$	Per cent difference
H_2	16.37	15.43	+6.26
O_2	12.75	12.07	+5.63
N_2	13.74	15.58	-11.9
CO	12.57	14.01	-10.4
I_2	7.93	9.31	-14.8
Hg_2	7.91	9.10	-13.1
CO_2	11.54	13.78	-16.3

Table 6.1: Ionization potentials in eV for diatomics and CO_2. Accepted values are taken from [162].

The appearance intensity is determined by finding the electric field for which the outer potential barrier of $U(\boldsymbol{r})$ just falls below ε_L, so that the electron is free from the Coulomb attraction and the molecule is ionized. This way, we can determine the appearance intensity $I_A(v)$ for a given vibrational level v by substituting R_v, the bond length at the outer turning point, into equations (6.5) and (6.6). Assuming that the laser beam has a Gaussian spatial distribution with peak intensity I_0, beam waist w_0 and wavelength λ, the focal volume with intensity between $I_A(v)$ and I_0 is given by [62, 65, 150]

$$V(I_A(v), I_0) = \frac{V_0}{3}\left(2c + \frac{c^3}{3} - 2\,\tan^{-1}c\right), \tag{6.7}$$

where $V_0 = 2\pi^2 w_0^4/\lambda$ and $c = \sqrt{(I_0/I_A(v)) - 1}$. Assuming that the molecules would not ionize until they experience a laser intensity $I \geq I_A(v)$, after which all of them will ionize, the measured signal enhancement between the ground vibrational level and an excited vibrational level v will be given by

$$S_{OBI}(v) = V(I_A(v), I_0)/V(I_A(0), I_0). \tag{6.8}$$

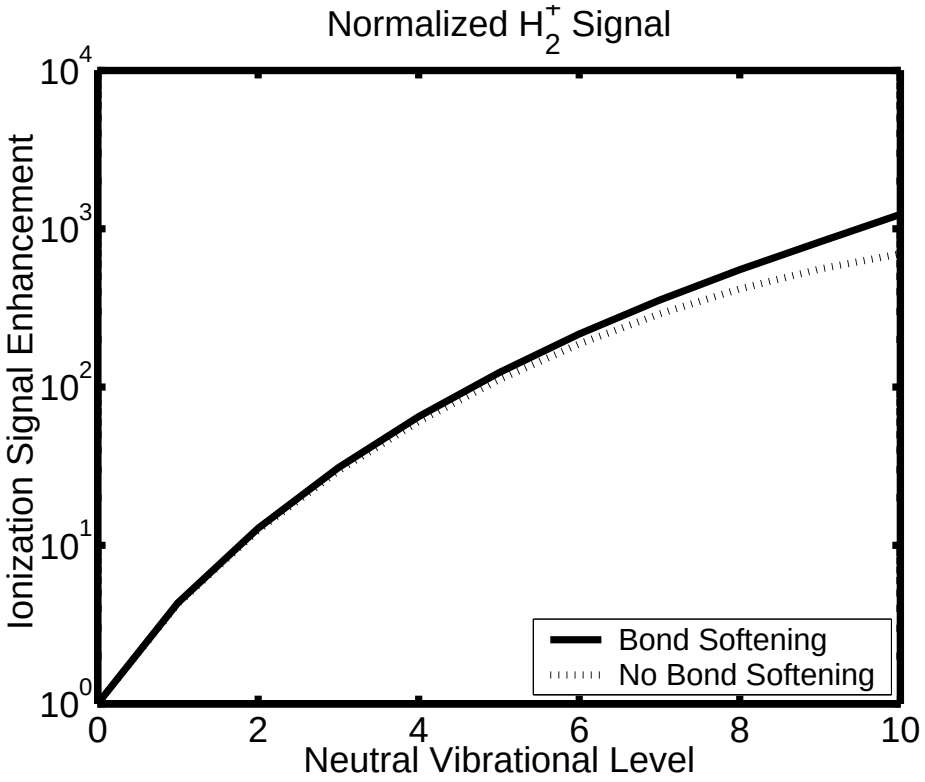

Figure 6.3: Normalized H_2 ionization signal enhancement ratios showing the effect of bond softening. A peak laser intensity of $I_0 = 4.3$ x 10^{13} W cm^{-2} has been used in this calculation. Equally, these represent limiting cases where the molecule is aligned parallel to the electric field (maximum bond softening, solid) or perpendicular to the electric field (no bond softening, dotted).

To compare the above ADK calculations with this OBI focal volume method, we must average the ADK rates (equation (6.4)) over this intensity distribution [63]:

$$\overline{w}(v, I_0) = \int_0^{I_0} D(I, I_0) w(v, I)\ \mathrm{d}I, \tag{6.9}$$

where

$$D(I, I_0) = V_0 \frac{1}{3I} \sqrt{\frac{(I_0 - I)}{I}} \left(1 + \frac{I_0}{2I}\right). \tag{6.10}$$

The volume expression in equation (6.7) is related to $D(I, I_0)$ by

$$V(I, I_0) = \int_I^{I_0} D(I', I_0)\ \mathrm{d}I' \quad \text{or} \quad D(I, I_0) = -\frac{\mathrm{d}V(I, I_0)}{\mathrm{d}I} \tag{6.11}$$

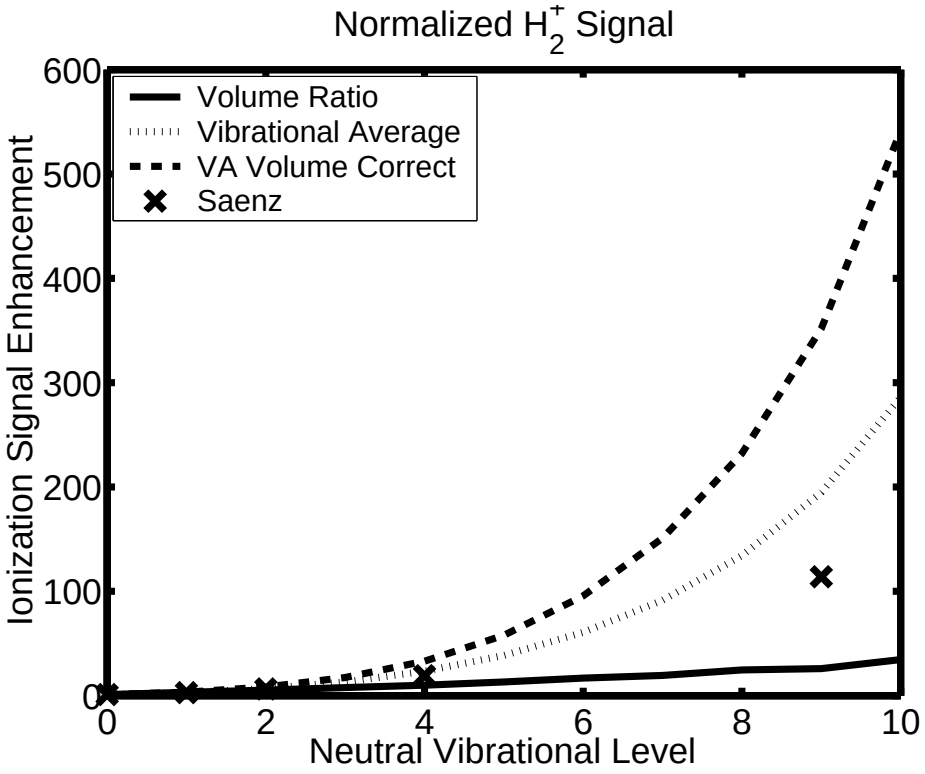

Figure 6.4: Ionization enhancement ratios for H_2 using the volume ratio method (solid) and the ADK vibrational averaging (dotted) method. The effect of volume correction on the vibrational average is shown with a dashed line. The *ab initio* results from [158] are included for comparison (crosses). In each case, the peak laser intensity is assumed to be $I_0 = 8$ x 10^{13} W cm^{-2}

6.4 Results

We first study the ionization of the hydrogen molecule. In figure 6.3, the ionization enhancement of H_2 as a function of vibrational level is plotted at intensity $I = 4.3$ x 10^{13} W cm^{-2}. The ionization rate increases rapidly with the vibrational level v since the ionization potential I_p decreases with v. Also shown is the effect of bond softening on the enhancement ratio. It is clear that bond softening affects the higher vibrational levels more that the lower vibrational levels, since the molecular bond length is larger for higher vibrational states and bond softening is more pronounced at large R.

In figure 6.4, we compare the enhancement ratio predicted by the simple OBI procedure with ADK calculations for H_2. The enhancement ratios are monotonic increasing functions of v, showing that they can be used to estimate the extent of vibrational excitations in experiments for this molecule. We observe that the focal volume corrected ratios $\overline{S}(V_0, I_0) = \overline{w}(v, I_0)/\overline{w}(0, I_0)$, are higher than the corresponding ratios $S(v, I_0) = w(v, I_0)/v(0, I_0)$ assuming a constant intensity profile, since the averaging in equation (6.9) affects the upper vibrational levels with lower

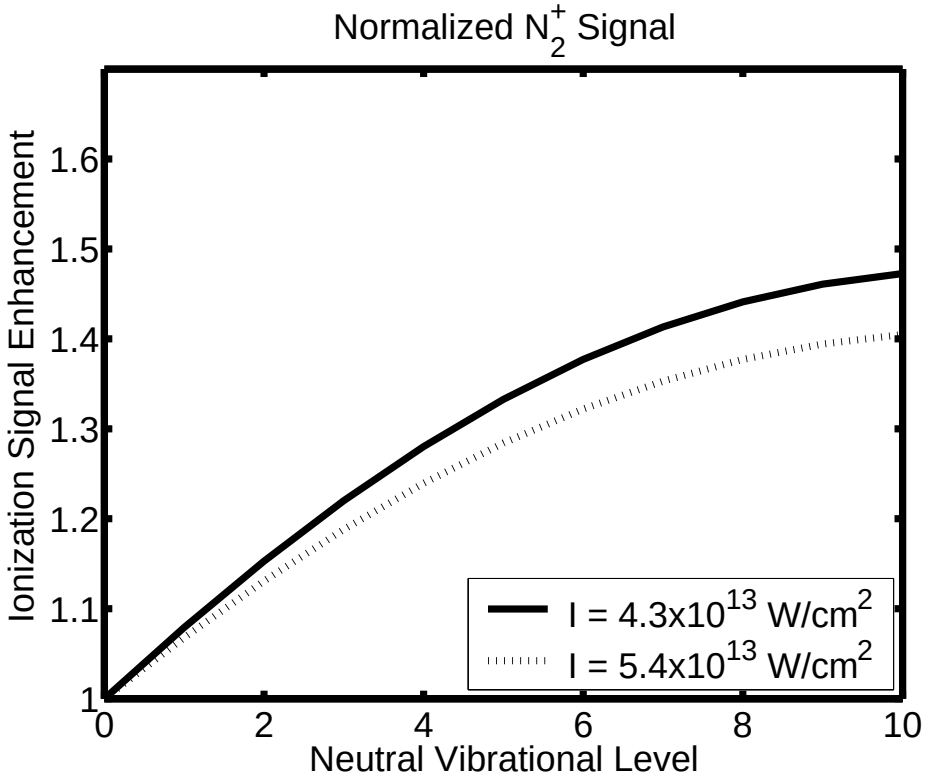

Figure 6.5: N_2 ionization signal enhancement ratios, assuming laser peak intensities of $I_0 = 4.3$ x 10^{13} W cm^{-2} (solid) and $I_0 = 5.4$ x 10^{13} W cm^{-2} (dotted). Note that when normalized signal enhancements are considered, higher laser intensities produce lower signal enhancements.

ionization potentials more than the vibrational ground level. We have also included the *ab initio* results [68] of Saenz (at a slightly higher intensity of 10^{14} W cm^{-2}) and the agreement with our $S(v, I_0)$ result is satisfactory, taking into account that the enhancement ratio decreases with increasing laser intensity [68]. However, the simple OBI results are consistently lower than the ADK results, and thus prediction using the OBI procedure tends to over-estimate the vibrational excitation for this system.

The enhancement ratios as a function of vibrational level are plotted for N_2 in figure 6.5 and for CO_2 in figure 6.6. The increase in ionization rates, and thus enhancement, for these systems is much less than that in H_2 since their ionization potential decreases with R much more slowly. For both N_2 and CO_2, the ionization rate changes so slowly that even if it were possible to coherently transfer 100% of the vibrational population from $v = 0$ to $v = 10$, the ionization signal would only increase by at most 50%. For CO_2, such small increase would not be able to account for the experimentally observed enhancements [149] realistically. Since the potential curves used for CO_2 and CO_2^+ are determined from different sources, it is a useful exercise to determine how much change in the ionization signal would occur if the ion potential were shifted slightly while its shape remained unaltered [146]. The

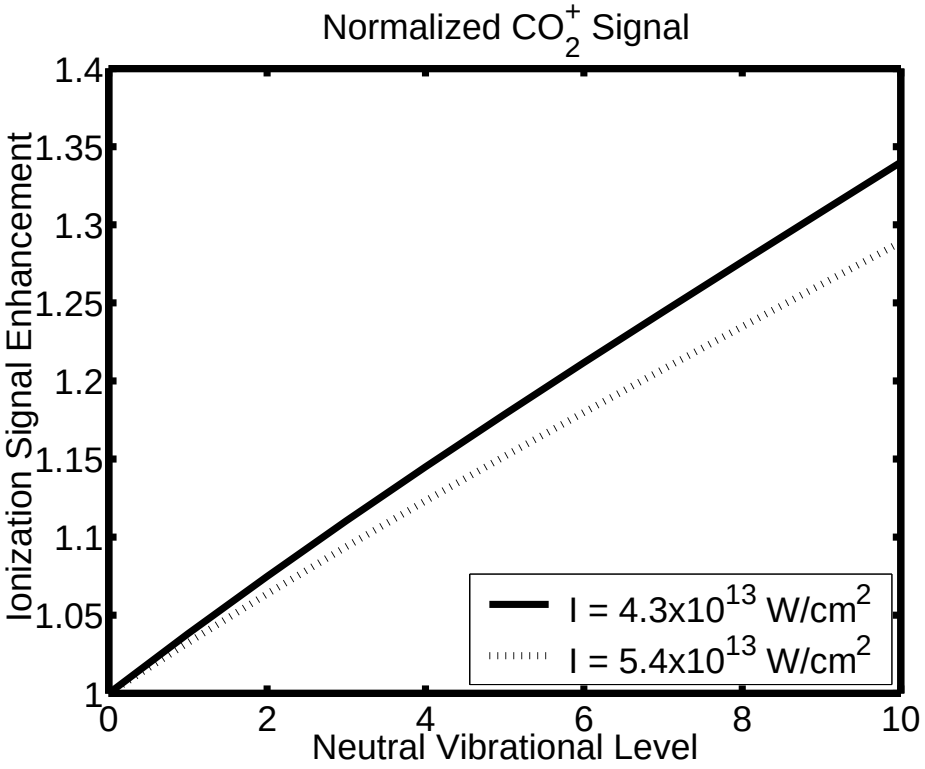

Figure 6.6: CO_2 ionization signal enhancement ratios, assuming laser peak intensities of $I_0 = 4.3$ x 10^{13} W cm^{-2} (solid) and $I_0 = 5.4$ x 10^{13} W cm^{-2} (dotted). Again, the tendency for higher laser intensities to produce lower signal enhancements is apparent.

results are striking. As figure 6.7 shows, when the equilibrium bond length in CO_2^+ is increased by 0.04 Å (3.5 %), the ionization signal enhancement grows by a factor of about 5, which would fall into the range observed experimentally. It should be emphasized again that we consider the symmetric stretch of CO_2 only and ignore any anharmonic coupling to other normal modes, thus allowing us to use the simple consideration as in the case of a diatomic molecule. For highly excited vibrational states, anharmonic effect becomes important and a more sophisticated treatment of the vibrational motion is necessary. Finally, in figure 6.8 we show the enhancement ratios for CO_2, using the potentials of figure 6.2, calculated from the simple OBI consideration for a Gaussian laser pulse, as well as from ADK methods. In contrast to the case of H_2 in figure 6.4, the OBI enhancement ratios are consistently higher than those obtained from the ADK procedures.

6.5 Conclusion

We have studied the dependence on the vibrational level of the ionization rate, and more importantly as a diagnostic tool the enhancement ratio, based on the ADK tunneling ionization theory suitably adapted to molecules. For molecules

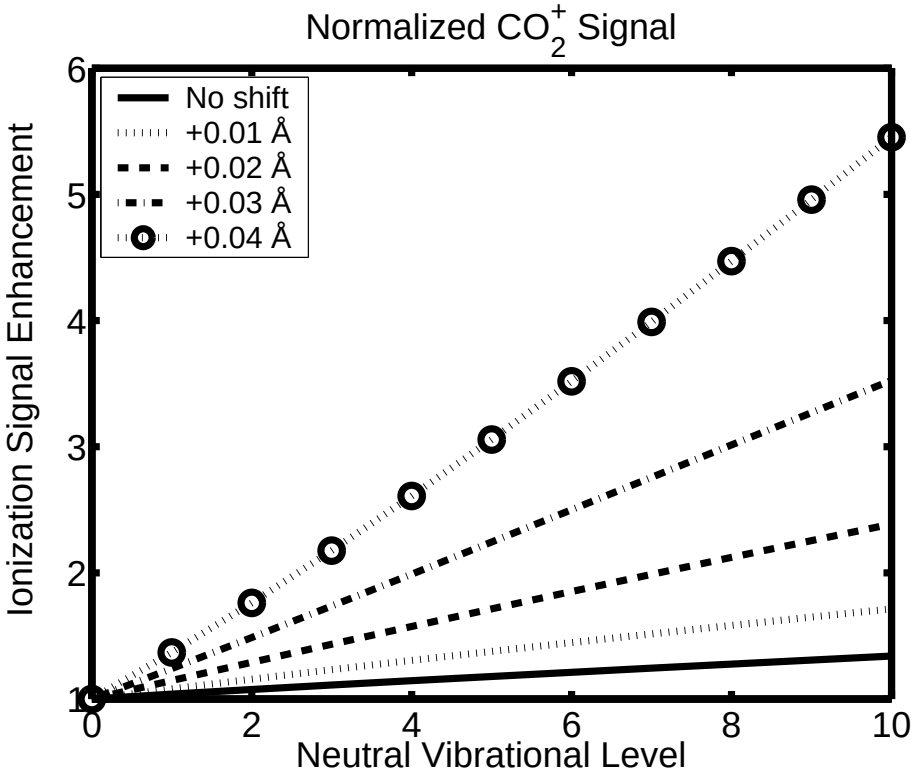

Figure 6.7: CO_2 ionization enhancement ratios after shifting the CO_2^+ curve by the indicated amount (no shift: solid; +0.01 Å: dotted; +0.02 Å: dashed; +0.03 Å: dot-dashed; +0.04 Å: dotted with circle). Peak laser intensity is held constant at $I_0 = 4.3$ x 10^{13} W cm^{-2}.

such as H_2, in which the change in the ionization potential is relatively large due in part to the effect of bond-softening, we see that over the first ten vibrationally excited levels there is an increase of ionization signal of several orders of magnitude. Thus, it is reasonable that the ionization enhancement signal could be used as a diagnostic to measure the amount of vibrational excitation. For N_2 and CO_2, the ionization potential computed from the neutral and ionic potentials currently available decreases only moderately over the first ten vibrationally excited levels, and the ionization enhancement signal would increase by at most 50%. In this case it would be difficult to resolve such a small increase in ionization rate under laboratory conditions. Clearly, using ionization rate as a vibrational excitation diagnostic is unsuitable for molecules like N_2 where there is only a slight difference in the neutral and ionic potential energy curves. However, the enhancement signal was found to be very sensitive to the relative position of the potential minimum of the neutral and ionic potential, and a small increase in the equilibrium bond length of the molecular ion would increase the ionization rate drastically. We have also compared the ionization signal enhancement calculated from the simple over-the-barrier ionization model together with focal volume consideration for a Gaussian beam with the corresponding focal volume corrected ADK calculations. For the H_2 molecule, both the OBI and ADK enhancement increases with the vibrational

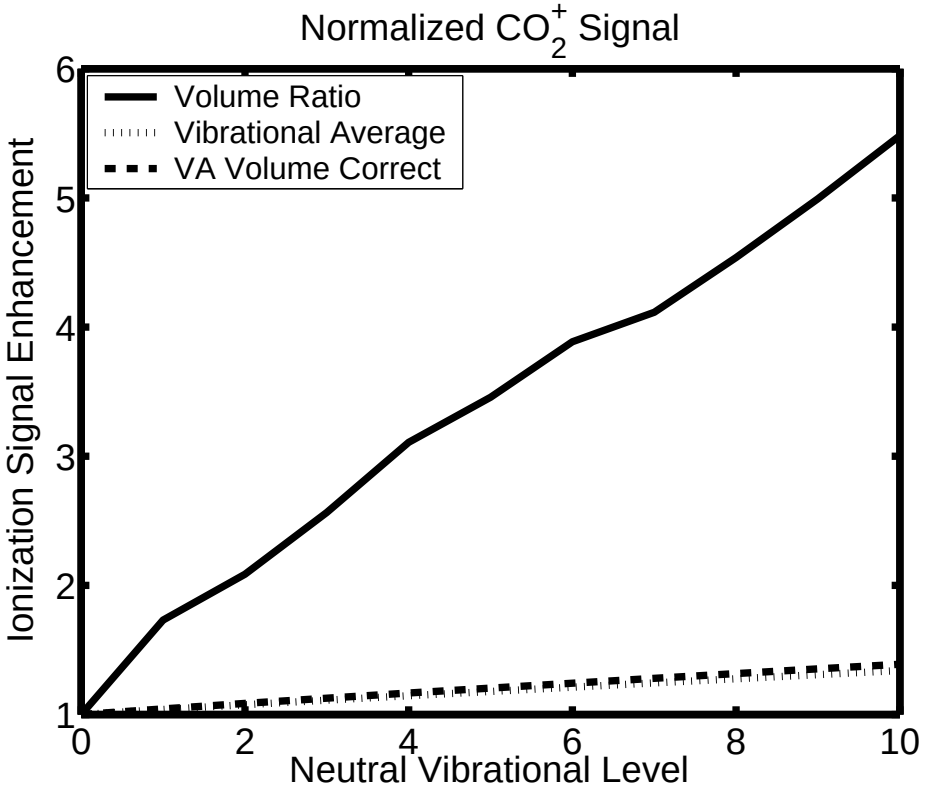

Figure 6.8: Ionization enhancement ratios for CO_2, comparing the volume ratio (OBI model, solid) with the vibrational averaging (ADK model, dotted) and the volume corrected vibrational averaging (dashed). Peak laser intensity is held constant at $I_0 = 4.3$ x 10^{13} W cm^{-2}.

level v. However, the OBI result is consistently below the ADK enhancement ratio, and the simple OBI procedure would over-estimate the vibrational excitation for this system. For the CO_2 molecule, the OBI and ADK enhancement both increase with vibrational level v, but the OBI result is consistently greater than the ADK enhancement ratio. Thus, it appears that the OBI calculations which gave good results for atoms [62, 150, 151] would not be adequate for a *quantitative* determination of the vibrational excitation of molecules, although it may still be useful for a qualitative estimation. Fortunately, the ADK procedures used in this paper are relatively easy to use, provided accurate potential energy surfaces for the neutral and ionic species are available.

Chapter 7

Summary

A triple coincidence imaging technique has been used to investigate fragmentation dynamics of CO_2 and CS_2 as they interact with intense laser fields.

In the case of CO_2, we have used the triple coincidence Coulomb imaging technique to examine a variety of phenomena as well as make the first-of-its-kind complete molecular geometry measurement for the molecule. The data have revealed important aspects of molecular behavior in the laser field. Firstly, we have seen that the charge state which gives bend angle distribution closest to theory is the lowest Coulomb channel (1,1,1); all other channels show a higher degree of straightening. We interpret this as being a result of competition between bending on the doubly ionized potential [93] and straightening during molecular dissociation. The measurement settles disagreement between the previous experiments of Hishikawa *et al.* [77] and Bryan *et al.* [82]. Higher channels show the dissociation deformation dominates and the molecular skeleton straightens. Also, by measuring the total energy released during fragmentation of each channel, we can clearly see evidence of multiple excitation channels which confirms preliminary observations in OCS [135] and also fits in with interpretations of multiple electronic processes in N_2 [57]. Alternatively, by following the bond length dependence on charge state we can see that there is a good fit with the behavior predicted by a simple over-the-barrier ionization mechanism. Finally, in order to account for the non-zero energy of the molecular fragments before the final ionization takes place, we have implemented a novel iterative technique to measure the molecular geometry at the point of final ionization.

In the case of CS_2, the Coulomb explosion imaging apparatus has made it possible to undertake the most systematic study of multi-electronic dissociative ionization to date. We clearly show that for our relatively long pulse we measure a kinetic energy release predicted by enhanced ionization while the sensitive triple coincidence Coulomb imaging method allows us to see much more details of the laser molecule interaction. Using the χ parameter, we have investigated the propensity of a molecule to dissociate into both concerted and sequential channels in the laser field. We then used the additional information available in the complete mo-

mentum measurements to show quantitatively that molecules undergoing concerted three body dissociation are bending. This confirms the previous observation [77] that bond length increases as bend angle decreases. However, we have shown that this simple trend does not represent a complete description; sequential dissociation processes can coexist alongside the concerted ones. The large degree of bond length asymmetry for high charge channels is attributed to pre-pulses evident in the interferometric autocorrelation. If these pre-pulses were sufficiently energetic, they could initiate a single dissociation before the arrival of the main pulse. The straight molecules observed by Iwasaki *et al.* [80] were most likely the result of wings on their pulse, but their ensemble type of measurement did not allow this to be identified as due to sequential dissociation. Notably, Hasegawa *et al.* [87] reported observing bent low charged CS_2 molecules. These bent molecules could originate from regions of the focus where the peak intensity is not particularly high. Consequently, the energy in the wings of the pulse would not be high enough to initiate sequential processes early on. The ratios of symmetric to asymmetric charge states is interesting because it compares well with HCI experiment [34] even though many of the molecules we are measuring are clearly very dissociated before the final ionization takes place; this is not the case for HCI. Despite the different mechanism for initiating fragmentation, very dissociated molecular ions show the propensity to occupy the lowest energy states, identical with HCI.

We have studied the influence of vibrational level on the rate of ionization based on the ADK tunneling ionization theory suitably adapted to molecules. More importantly, we explored the applicability of ionization rate as a diagnostic tool for vibrational excitation. For molecules such as H_2, in which the change in the ionization potential is relatively large due in part to the effect of bond-softening, we see that over the first ten vibrationally excited levels there is an increase of ionization signal of several orders of magnitude. Thus, it is reasonable that the ionization enhancement signal could be used as a diagnostic to measure the amount of vibrational excitation. Under laboratory conditions, it would be difficult to use this technique for molecules such as N_2 and CO_2, since the ionization potential computed from the neutral and ionic potentials currently available decreases only moderately over the first ten vibrationally excited levels; the ionization enhancement signal would increase by at most 50%. The enhancement signal was found to be very sensitive to the relative position of the potential minimum of the neutral and ionic potential, and a small increase in the equilibrium bond length of the molecular ion would increase the ionization rate drastically. We have also compared the ionization signal enhancement computed from the simple over-the-barrier ionization model together with focal volume consideration for a Gaussian beam with the corresponding focal volume corrected ADK calculations. For the H_2 molecule, both the OBI and ADK enhancement increases with the vibrational level v. However, the OBI result is consistently *below* the ADK enhancement ratio, and the simple OBI procedure would over-estimate the vibrational excitation for this system. For the CO_2 molecule, the OBI and ADK enhancement both increase with vibrational level v, but the OBI result is consistently *greater* than the ADK enhancement ratio. Thus, it appears

that the OBI calculations which gave good results for atoms [62, 150, 151] would not be adequate for a *quantitative* determination of the vibrational excitation of molecules, although it may still be useful for a qualitative estimation. Fortunately, the ADK procedures used in this paper are relatively easy to use, provided accurate potential energy surfaces for the neutral and ionic species are available.

7.1 Future Work

Coulomb explosion imaging is still in its infancy and many technological challenges must be overcome before the complete reconstruction of large molecules can be attempted. Image clarity can be improved by using cold molecules produced from a pulsed valve or supersonic molecular beam. Few-cycle pulses must be available at multi-kHz repetition rates with matching electronic data-grabbing. Experimental facilities presently exist at the Advanced Laser Light Source in Varennes, Quebec that fulfill these requirements. Ideally, reliable diagnostics must exist to measure single-shot autocorrelations in coincidence with explosion data. The deduction of the structure of a large molecule from its fragment momenta is feasible if difficult. The requirement of recording all fragment momenta becomes exponentially more difficult according to the number of fragments. However, the simplex algorithm described in this work is extensible and could be applied to larger molecules of arbitrary symmetry provided that sufficient computational resources are available.

Appendices

Appendix A

Data Acquisition Algorithms

A.1 FindEvent

The program known as `FindEvent` reads raw data from the Gage cards and extracts event information. Each acquisition of the Gage cards corresponds to a single laser shot. For each shot of recorded data, the `FindEvent` algorithm is performed as follows:

1. Add the signals from each of the four channels. Each channel is composed of 1024 bytes of data. The summation will therefore be 1024 integers with a numerical range of 0 to 1020.

$$x_{sum} = \sum_{i}^{4} x_i$$

2. Ion impacts are characterized by large changes in the signal from the detector. To find out if there has been such a change, subtract the smallest value of the summation from the largest value. If this number is larger than a difference threshold, continue the analysis of this laser shot. Otherwise, abort and start the next shot.

$$max(x_{sum}) - min(x_{sum}) > \text{threshold?}$$

3. For the summation, perform an element-by-element differentiation.

$$x_{sumdiff}(n) = x_{sum}(n) - x_{sum}(n-1)$$

4. Once again, large changes in the differentiated signal will correspond to ion impacts. If a second threshold is exceeded, calculate the ion position based on the local values of each of the four channels x_i according to equations 2.9, 2.10 and the calibration transformations in equations A.1–A.4.

$$x_{sumdiff}(n) > \text{differential threshold?}$$

5. A series of six numbers describing the ion impact is stored to a file. These values are: ID, the unique identifier of that experiment; Shot, the unique identifier of the laser shot; Ion, indicating that this ion is the nth ion to hit the detector for that laser shot; t, x and y, corresponding to the temporal and position information for that ion.

$$\text{data set} = (\text{ID}, \text{Shot}, \text{Ion}, t, x, y)$$

6. The data is loaded into a `mySQL` database and is filtered once more so that only correlated sets of triple events are retained. Correlated triple events are those where exactly three ions originating from the same laser shot hit the detector. The `mySQL` algorithm uses the ID, Shot and Ion values to perform the event sorting. Once the sorting is complete, these values are extraneous. Therefore, triple event data is composed only of time and position data. Nine numbers characterize each correlated triple event.

$$\text{data set} = (t_1, x_1, y_1, t_2, x_2, y_2, t_3, x_3, y_3)$$

7. Note that the data set is always ordered such that $t_1 < t_2 < t_3$.

A.2 Detector Geometry Calibration

The following series of translations and matrix transformations are necessary to take the data from the detector in arbitrary units and and map it to physical quantities.

1. Calculate x_0, y_0 according to Equations 2.9 and 2.10.

2. Move the centre of the mask to the origin. To do this, perform the translation

$$\begin{pmatrix} x_1 \\ y_1 \end{pmatrix} = \begin{pmatrix} x_0 \\ y_0 \end{pmatrix} - \begin{pmatrix} 0.480 \\ 0.516 \end{pmatrix} \tag{A.1}$$

3. Multiply by a stretch and shear matrix to orient the mask to the $x-$ and $y-$axes. This transformation will return the position in units of mm.

$$\begin{pmatrix} x_2 \\ y_2 \end{pmatrix} = \begin{pmatrix} 101.85 & -6.362 \\ 18.17 & 43.17 \end{pmatrix} \begin{pmatrix} x_1 \\ y_1 \end{pmatrix} \tag{A.2}$$

4. Rotate the recovered positions by 10°. This is the angle between the axes of the mask and the detector.

$$\begin{pmatrix} x_3 \\ y_3 \end{pmatrix} = \begin{pmatrix} 0.9851 & 0.1719 \\ 0.1719 & 0.9851 \end{pmatrix} \begin{pmatrix} x_2 \\ y_2 \end{pmatrix} \tag{A.3}$$

5. Finally, remove the discrepancy between the centres of the mask and detector. That is, an event with all four channels having equal height must produce a result of (0,0). This final translation corrects the origin.

$$\begin{pmatrix} x_4 \\ y_4 \end{pmatrix} = \begin{pmatrix} x_3 \\ y_3 \end{pmatrix} + \begin{pmatrix} -2.0504 \\ 0.6903 \end{pmatrix} \tag{A.4}$$

Appendix B

Simplex Algorithm and Graphical Representation

B.1 Simplex Algorithm

Mathematically, the simplex procedure can be stated as follows:

1. Choose initial points $\mathbf{x}_1, \mathbf{x}_2, \mathbf{x}_3, ...\mathbf{x}_{N+1}$ to form a simplex in R^N.

2. If a given stopping condition is satisfied, stop. Otherwise, find $\mathbf{x}_B, \mathbf{x}_W \in \{\mathbf{x}_1, \mathbf{x}_2, \mathbf{x}_3, ...\mathbf{x}_{N+1}\}$ such that $f(\mathbf{x}_B) = \min_{j=1,...N+1} f(\mathbf{x}_j)$ and $f(\mathbf{x}_W) = \max_{j=1,...,N+1} f(\mathbf{x}_j)$. Let $\overline{\mathbf{x}} = \sum_{j \neq W} \mathbf{x}_j / N$.

3. Let $\mathbf{x}_R = \overline{\mathbf{x}} + \alpha(\overline{\mathbf{x}} - \mathbf{x}_W)$. If $\max_{j=1,...N+1}\{f(\mathbf{x}_j)_{j \neq W}\} \geq f(\mathbf{x}_R)$, then replace $\mathbf{x}_W$ with $\mathbf{x}_R$ (reflection) to form a new simplex and go to step 4. Otherwise, go to step 5.

4. Let $\mathbf{x}_E = \overline{\mathbf{x}} + \beta(\overline{\mathbf{x}} - \mathbf{x}_W)$. If $f(\mathbf{x}_B) > f(\mathbf{x}_R) > f(\mathbf{x}_E)$, replace $\mathbf{x}_R$ which was $\mathbf{x}_W$ before the reflection step on step 3) with $\mathbf{x}_E$ (expansion) to form a new simplex. Go to step 2.

5. Let $\mathbf{x}'$ be defined by $f(\mathbf{x}') = \min\{\mathbf{x}_R, \mathbf{x}_W\}$ and let $\mathbf{x}_C = \overline{\mathbf{x}} + \gamma(\overline{\mathbf{x}} - \mathbf{x}')$. If $f(\mathbf{x}_C) \leq f(\mathbf{x}')$, then replace $\mathbf{x}_W$ with $\mathbf{x}_C$ (contraction) to form a new simplex. Otherwise, replace $\mathbf{x}_j$ with $\mathbf{x}_j + (\mathbf{x}_B - \mathbf{x}_j)/2$ for $j = 1, ..., N+1$. Go to step 2.

The procedure will conclude on step 2 if either of the following conditions are satisfied: (i) if the points forming the current simplex converge to a point, within a given tolerance; (ii) the total number of iterations reaches a predetermined number.

B.2 Graphical Representation of Basic Simplex Algorithm

A graphical representation of a simplex algorithm can be done for systems of low dimensionality. A 2-dimensional system has a convex hull with three vertices and can be plotted on a 2-dimensional graph with the evaluated functional value represented by a contour map. A 3-dimensional system would require a hull with four vertices, that is, a tetrahedron, to visualize.

Consider a system defined by a function dependent upon two variables. That is, $f = f(x_1, x_2)$. Three points are chosen in the space defined by x_1 and x_2 and the system function is evaluated at these points. The points are ranked according to their fitness, where in this case, a lower value of the function is desired. Figure B.1 illustrates this starting condition.

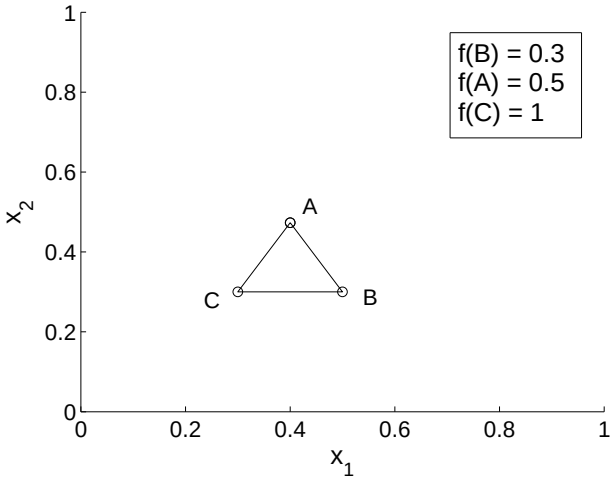

Figure B.1: 2-dimensional simplex with initial points and ranked fitness values shown. Here, the simplex has been arbitrarily chosen to have side length of 0.2 units.

A point R is created by reflecting the worst point in the line defined by the better two points. If the reflection point has a better fitness than the worst point, the reflection point is entered into the simplex as shown in figure B.2.

This procedure continues until an exit condition is met. The size of the area defined by the simplex triangle never changes and it is important to choose a small enough area to allow sufficient sampling of the solution space. If the algorithm ever returns to a previous point in the solution space, the system will oscillate. For this reason, it is necessary to record previously attempted solutions and exit the algorithm if oscillations do occur.

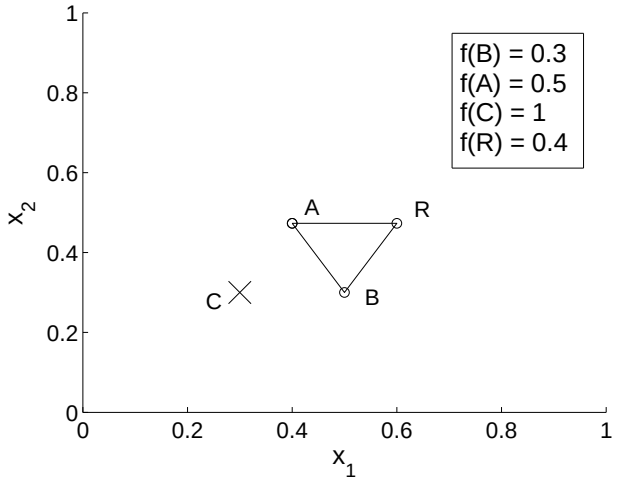

Figure B.2: Updated simplex with reflected point R having replaced initial point C.

B.3 Graphical Representation of Dynamic Simplex Algorithm

Several enhancements can be made upon the basic simplex algorithm. These enhancements dynamically change the size of the simplex area to allow for a faster optimization routine.

B.3.1 Expansion in the optimal direction

If the reflection operation from the basic simplex produced a better result than the second worst point (A in B.3), it may be that traveling further along the same vector will produce an even better result. An expansion point, indicated by E, is computed and the fitness at that point is evaluated. As shown in figure B.3, if the fitness at E is better than at R, E is placed in the simplex.

B.3.2 Contraction in the optimal direction

If upon reflection the point R was found to be *worse* than the second worst point, it may still be worthwhile to move some distance in the direction of R. A contraction point, indicated by X_C, is computed by taking the better of points C and R and finding the point halfway between that point and the line of reflection. The fitness is once again evaluated and if X_C is better, it is added to the simplex. See figure B.4.

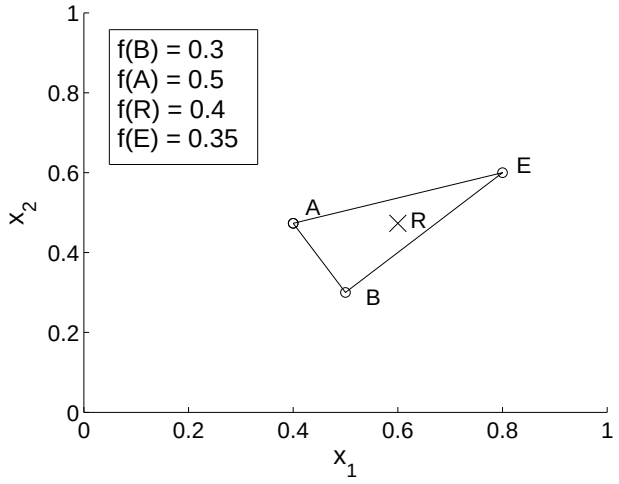

Figure B.3: Updated simplex with reflected point R having been replaced by expansion point E.

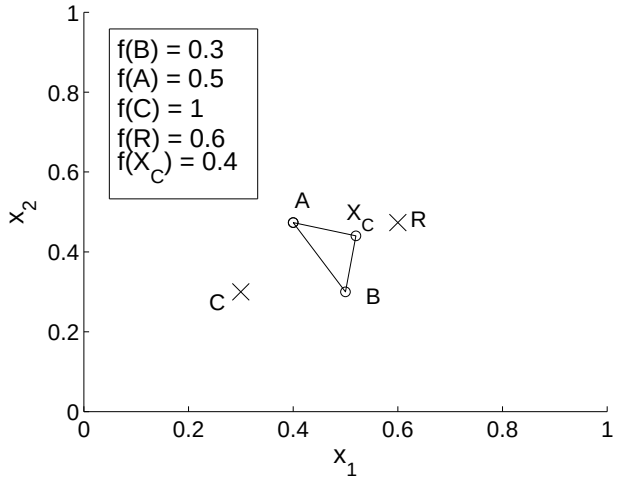

Figure B.4: Updated simplex with compression point X_C. In this case, the point R was found to have a worse fitness than the second worst point in the original simplex, point A.

B.3.3 Contraction of simplex

If the reflection, expansion and contraction operations are unable to locate a better point than the worst point in the simplex, the simplex is contracted in the direction of the best point. This operation usually occurs when the algorithm is near to the optimal solution and has a relatively minor change on the system. This is shown graphically in figure B.5.

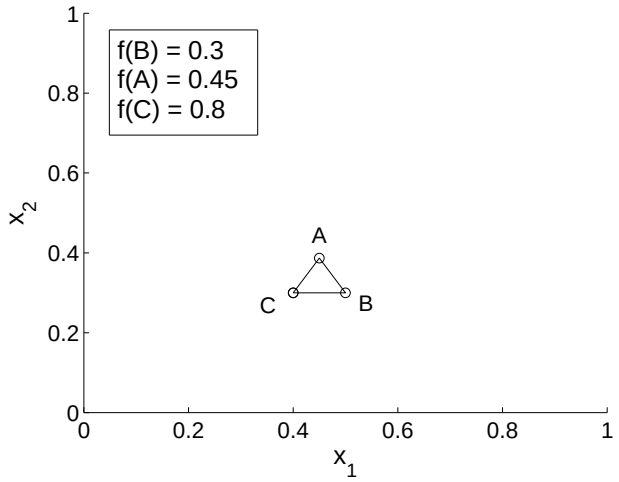

Figure B.5: Updated simplex with system compression. In this case, all previous operations have failed to produce a point better than the point C. The system is contracted in the direction of the best point, B.

References

[1] A. L. Basham. *Cultural History of India*. Oxford University Press, 1999. 1

[2] A. A. Long, editor. *The Cambridge Companion to Early Greek Philosophy*. 1979. 1

[3] N. Melchert. *The Great Conversation: A Historical Introduction to Philosophy*. McGraw Hill, 2002. 1

[4] R. Boscovich. *Theoria philosophiae naturalis redacta ad unicam legem virium in natura existentium*. 1758. 1

[5] I. Newton. *Principia*. 1687. 1

[6] J. Dalton. *New System of Chemical Philosophy*. 1808. 1

[7] E. Rutherford. *Philos. Mag.*, 6(21):669–688, 1911. 2

[8] N. Bohr. *Philos. Mag.*, 6(26):1–25, 1913. 2

[9] J. Chadwick. *Proc. Roy. Soc., A*, 136:692–708, 1932. 2

[10] G. N. Lewis. *J. Am. Chem. Soc.*, 38:762, 1916. 2

[11] R. A. Serway. *Physics for Scientists and Engineers with Modern Physics*. Saunders College Publishing, third edition, 1992. 2

[12] P. F. Bernath. *Spectra of Atoms and Molecules*. Oxford University Press, second edition, 2005. 2

[13] G. Herzberg. *Molecular Spectra and Molecular Structure: Spectra of Diatomic Molecules*. Krieger Publishing, second edition, 1989. 2

[14] G. Herzberg. *Molecular Spectra and Molecular Structure: Electronic Spectra and Electronic Structure of Polyatomic Molecules*. Krieger Publishing, 1991. 2

[15] G. Herzberg. *Molecular Spectra and Molecular Structure: Infrared and Raman Spectra of Polyatomic Molecules*. Krieger Publishing, 1991. 2

[16] E. G. Stout and L. H. Jensen. *X-Ray Structure Determination: A Practical Guide*. Macmillan, 1968. 2

[17] J. P. Glusker and K. N. Trueblood. *Crystal Structure Analysis*. Oxford University Press, 1972. 2

[18] P. Goodman, editor. *Fifty Years of Electron Diffraction*. Reidel, 1981. 2

[19] J. D. Watson and F. H. C. Crick. Molecular structure of nucleic acids: A structure for deoxyribose nucleic acid. *Nature*, 171:737–738, 1953. 3

[20] J. C. Kendrew, G. Bodo, H. M. Dintzis, R. G. Parrish, H. Wyckoff, and D. C. Phillips. A three-dimensional model of the myoglobin molecule obtained by X-ray analysis. *Nature*, 181:662–666, 1958. 3

[21] C. C. Blake, D. F. Koenig, G. A. Mair, A. C. North, D. C. Phillips, and V. R. Sarma. Structure of hen egg-white lysozyme: A three-dimensional Fourier synthesis at 2 å resolution. *Nature*, 206:757–761, 1965. 3

[22] R. Henderson. The potential and limitations of neutrons, electrons and X-rays for atomic-resolution microscopy of unstained biological molecules. *Q. Rev. Biophys.*, 28:171–193, 1995. 3

[23] E. P. Kanter, P. J. Cooney, D. S. Gemmell, K. O. Groeneveld, W. J. Pietsch, A. J. Ratkowski, Z. Vager, and B. J. Zabranski. Role of excited electronic states in the interactions of fast (MeV) molecular ions with solids and gases. *Phys. Rev. A*, 20:834–854, 1979. 3

[24] Z. Vager, R. Naaman, and E. P. Kanter. Coulomb explosion imaging of small molecules. *Science*, 244:426–431, 1989. 4

[25] D. Zajfman and Z. Amitay. Measurement of the vibrational populations of molecular ions and its application to dissociative recombination in storage rings. *Phys. Rev. A*, 52:839–842, 1995. 4

[26] J. H. Sanderson, R. V. Thomas, W. A. Bryan, W. R. Newell, P. F. Taday, and A. J. Langley. Multielectron-dissociative-ionization of SF_6 by intense femtosecond laser pulses. *J. Phys. B: At. Mol. Opt. Phys.*, 30:4499–4507, 1997. 4

[27] T. Mizogawa, Y. Ayawa, Y. Isozumi, R. Katano, S. Ito, and N. Maeda. New readout technique for 2-dimensional position-sensitive detectors. *Nucl. Instrum. Methods Phys. Res., Sect. A*, 312:547–552, 1992. 4, 37, 38

[28] J. Becker, K. Beckord, U. Werner, and H. O. Lutz. A system for correlated fragment detection in dissociation experiments. *Nucl. Instrum. Methods Phys. Res., Sect. A*, 337:409–415, 1994. 4, 37

[29] U. Werner, K. Beckord, J. Becker, and H.O. Lutz. 3D imaging of the collision-induced coulomb fragmentation of water molecules. *Phys. Rev. Lett.*, 74:1962–1965, 1995. Online abstract: `http://prola.aps.org/abstract/PRL/v74/i11/p1962_1`. 4, 5

[30] U. Werner, K. Beckord, J. Becker, H.O. Folkerts, and H.O. Lutz. Ion-impact-induced fragmentation of water molecules. *Nucl. Instrum. Methods Phys. Res., Sect. B*, 98:385–388, 1995. 4

[31] J. H. Sanderson, T. Nishide, H. Shiromaru, Y. Achiba, and N. Kobayashi. Near-Coulombic behaviour in the dissociative ionization of CO_2 due to impact by Ar^{8+}. *Phys. Rev. A*, 59:4817–4820, 1999. 5, 6, 18, 38

[32] H. Shiromaru, T. Nishide, T. Kitamura, J. H. Sanderson, Y. Achiba, and N. Kobayashi. Dissociation scheme of highly charged triatomic molecules. *Phys. Scr. T.*, 80A:110–113, 1999. 6, 38

[33] T. Nishide, F. A. Rajgara, T. Kitamura, H. Shiromaru, Y. Achiba, and N. Kobayashi. Dissociation of highly charged CS_2 formed by low energy collisions with HCI. *Phys. Scr. T.*, 92:415–419, 2001. 6, 38

[34] F. A. Rajgara, M. Krishnamurthy, D. Mathur, T. Nishide, T. Kitamura, H. Shiromaru, Y. Achiba, and N. Kobayashi. Fragmentation dynamics of CS_2^{q+} (q=3-10) molecular ions. *Phys. Rev. A*, 64:032712, 2001. Online abstract: `http://link.aps.org/abstract/PRA/v64/e032712`. 6, 7, 19, 38, 53, 81, 83, 84, 85, 86, 87, 88, 89, 106

[35] T. Kitamura, T. Nishide, H. Shiromaru, Y. Achiba, and N. Kobayashi. Direct observation of "dynamic" chirality by Coulomb explosion imaging. *J. Chem. Phys.*, 115:5–6, 2001. 7, 38

[36] K. Codling, L. J. Frasinski, P. A. Hatherly, and J. R. M. Barr. On the major-mode of multiphoton multiple ionization. *J. Phys. B: At. Mol. Opt. Phys*, 20:L525–L531, 1987. 7

[37] L. J. Frasinski, K. Codling, P. Hatherly, J. Barr, I. N. Ross, and W. T. Toner. Femtosecond dynamics of multielectron dissociative ionization by use of picosecond laser. *Phys. Rev. Lett*, 58:2424–2427, 1987. 7, 8

[38] L. J. Frasinski, K. Codling, and P. A. Hatherly. Covariance mapping - a correlation method applied to multiphoton multiple ionization. *Science*, 246:1029–1031, 1989. 7, 8

[39] K. Codling and L. J. Frasinski. Dissociative ionization of small molecules in intense laser fields. *J. Phys. B: At. Mol. Opt. Phys*, 26:783–809, 1993. See also references therein. 7

[40] L. J. Frasinski, K. Codling, and P. A. Hatherly. Multiphoton multiple ionization of N_2 probed by covariance mapping. *Phys. Lett. A*, 142:499–503, 1989. 8, 9

[41] P. A. Hatherly, L. J. Frasinski, K. Codling, A. J. Langley, and W. Shaikh. The angular-distribution of atomic ions following the multiphoton ionization of carbon-monoxide. *J. Phys. B: At. Mol. Opt. Phys.*, 23:L291–L295, 1990. 9, 12

[42] P. A. Hatherly, M. Stankiewicz, K. Codling, L. J. Frasinski, and G. M. Cross. The multielectron dissociative ionization of molecular-iodine in intense laser fields. *J. Phys. B: At. Mol. Opt. Phys.*, 27:2993–3003, 1994. 9, 10, 12

[43] L. J. Frasinski, P. A. Hatherly, K. Codling, M. Larsson, A. Persson, and C. G. Wahlstrom. Multielectron dissociative ionization of CO_2 in intense laser fields. *J. Phys. B: At. Mol. Opt. Phys.*, 27:L109–L114, 1994. 9, 10, 12

[44] W. H. Knox, R. S. Knox, J. F. Hoose, and R. N. Zare. Observation of the 0-fs pulse. *Opt. Photonics News*, 1:44–45, 1990. 9

[45] C. Cornaggia, J. Lavancier, D. Normand, J. Morellec, P. Agostini, J. P. Chambaret, and A. Agonetti. Multielectron dissociative ionization of diatomic-molecules in an intense femtosecond laser field. *Phys. Rev. A*, 44:4499–4505, 1991. 9, 12

[46] C. Cornaggia, D. Normand, and J. Morellec. Role of the molecular electronic configuration in the Coulomb fragmentation of n_2, c_2h_2 and c_2h_4 in an intense laser field. *J. Phys. B: At. Mol. Opt. Phys.*, 25:L415–L422, 1992. 9, 12

[47] C. Cornaggia, M. Schmidt, and D. Normand. Coulomb explosion of CO_2 in an intense femtosecond laser field. *J. Phys. B: At. Mol. Opt. Phys.*, 27:L123–L130, 1994. 9, 12, 67

[48] M. Schmidt, D. Normand, and C. Cornaggia. Laser-induced trapping of chlorine molecules with picosecond and femtosecond pulses. *Phys. Rev. A*, 50:5037–5045, 1994. 9, 10, 12

[49] C. Cornaggia, M. Schmidt, and D. Normand. Laser-induced nuclear motions in the Coulomb explosion of $C_2H_2^+$ ions. *Phys. Rev. A*, 51:1431–1437, 1995. 9, 67

[50] C. Cornaggia. Carbon geometry of $C_3H_3^+$ and $C_3H_4^+$ molecular-ions probed by laser-induced Coulomb explosion. *Phys. Rev. A*, 52:R4328–R4331, 1995. 9, 10

[51] C. Cornaggia. Large-amplitude nuclear motions in the laser-induced Coulomb explosion of carbon dioxide molecules. *Phys. Rev. A*, 54:R2555–R2558, 1996. 9, 10, 18, 67, 72, 73, 74, 75, 76

[52] C. Cornaggia, F. Salin, and C. Le Blanc. Changes in the SO_2 geometry during the laser-induced multiple ionization and fragmentation. *J. Phys. B*, 29:L749–L754, 1996. 9, 10, 16, 67, 74

[53] W. C. Wiley and I. H. McLaren. Time-of-flight mass spectrometer with improved resolution. *Rev. Sci. Instr.*, 26:1150–1157, 1955. 9, 28

[54] J. H. Posthumus, L. J. Frasinski, A. J. Giles, and K. Codling. Dissociative ionization of molecules in intense laser fields - a method of predicting ion kinetic energies and appearance intensities. *J. Phys. B: At. Mol. Opt. Phys.*, 28:L349–L353, 1995. 10, 11, 67, 77, 78, 90, 92, 93, 97

[55] T. Zuo and A. D. Bandrauk. Charge-resonance-enhanced ionization of diatomic molecular ions by intense lasers. *Phys. Rev. A*, 52:R2511–R2514, 1995. 10, 12, 67, 93

[56] T. Seideman, M. Yu. Ivanov, and P. B. Corkum. Role of electron localization in intense-field molecular ionization. *Phys. Rev. Lett.*, 75:2819–2822, 1995. 10, 67

[57] J. P. Nibarger, S. V. Menon, and G. N. Gibson. Comprehensive analysis of strong-field ionization and dissociation of diatomic nitrogen. *Phys. Rev. A*, 63:053406, 2001. 12, 79, 105

[58] S. V. Menon, J. P. Nibarger, and G. N. Gibson. A framework for understanding molecular ionization in strong laser fields. *J. Phys. B: At. Mol. Opt. Phys.*, 35:2961–2974, 2002. 12, 90

[59] M. V. Ammosov, N. B. Delone, and V. P. Krainov. Tunnel ionization of complex atoms and atomic ions in a varying electromagnetic-field. *Zh. Eksp. Teor. Fiz.*, 91:2008–2013, 1986. 12, 13, 93, 96

[60] L. D. Landau and E. M. Lifshitz. *Quantum Mechanics, Non-Relativistic Theory*, volume section 77. Oxford: Pergamon, 1991. 12

[61] A. M. Perelomov, V. S. Popov, and M. V. Terentev. *Sov. Phys. – JETP*, 23:924, 1965. 13

[62] S. Augst, D. D. Meyerhofer, D. Strickland, and S. L. Chin. Laser ionization of noble-gases by Coulomb-barrier suppression. *J. Opt. Soc. Am. B*, 8:858–867, 1991. 13, 93, 94, 98, 104, 107

[63] M. Protopapas, C. H. Keitel, and P. L. Knight. Atomic physics with super-high intensity lasers. *Rep. Prog. Phys.*, 60:389–486, 1997. 13, 99

[64] S. L. Chin, Y. Liang, J. E. Decker, F. A. Ilkov, and M. V. Ammosov. Tunnel ionization of diatomic-molecules by an intense CO_2-laser. *J. Phys. B: At. Mol. Opt. Phys.*, 25:L249–L255, 1992. 13

[65] P. Dietrich and P. B. Corkum. Ionization and dissociation of diatomic-molecules in intense infrared-laser fields. *J. Chem. Phys.*, 97:3187–3198, 1992. 13, 98

[66] P. Dietrich, D. T. Strickland, and P. B. Corkum. Multiphoton ionization of inertially confined molecular-ions. *J. Phys. B: At. Mol. Opt. Phys.*, 92:2323–2334, 1993. 13

[67] M. Ivanov, T. Seideman, F. Ilkov, P. Dietrich, and P. Corkum. Explosive ionization of molecules in intense laser fields. *Phys. Rev. A*, 54:1541–1550, 1996. 13

[68] A. Saenz. Behavior of molecular hydrogen exposed to strong dc, ac, or low-frequency laser fields. II. Comparison of *ab initio* and Ammosov-Delone-Krainov rates. *Phys. Rev. A*, 66:063408, 2002. 13, 101

[69] X. M. Tong, Z. X. Zhao, and C. D. Lin. Theory of molecular tunneling ionization. *Phys. Rev. A*, 66:033402, 2002. 13

[70] Z. X. Zhao, X. M. Tong, and C. D. Lin. Alignment-dependent ionization probability of molecules in a double-pulse laser field. *Phys. Rev. A*, 67:043404, 2003. 13

[71] K. Mishima, K. Nagaya, M. Hayashi, and S. H. Lin. Theoretical studies of high-power laser ionization of molecules in the tunneling region. *Phys. Rev. A*, 70:063414, 2004. 13

[72] X. Urbain, B. Fabre, E. M. Staicu-Casagrande, N. de Ruette, V. M. Andrianarijaona, J. Jureta, J. H. Posthumus, A. Saenz, E. Baldit, and C. Cornaggia. Intense-laser-field ionization of molecular hydrogen in the tunneling regime and its effect on the vibrational excitation of H_2^+. *Phys. Rev. Lett.*, 92:163004, 2004. Online abstract: `http://link.aps.org/abstract/PRL/v92/e163004`. 13, 15, 93, 95, 97

[73] G. H. Dunn and B. Van Zyl. Electron impact dissociation of H_2^+. *Phys. Rev.*, 154:40–51, 1967. 15

[74] F. von Busch and G. H. Dunn. Photodissociation of H_2^+ and D_2^+ - experiment. *Phys. Rev. A*, 5:1726–1743, 1972. 15

[75] A. Hishikawa, A. Iwamae, K. Hoshina, M. Kono, and K. Yamanouchi. Mass-resolved two-dimensional momentum imaging of the Coulomb explosion of N_2 and SO_2 in an intense laser field. *Chem. Phys. Lett.*, 282:283–291, 1998. 14, 17

[76] A. Hishikawa, A. Iwamae, K. Hoshina, M. Kono, and K. Yamanouchi. Coulomb explosion dynamics of N_2 in intense laser field by mass-resolved momentum imaging. *Chem. Phys.*, 231:315–329, 1998. 14, 16

[77] A. Hishikawa, A. Iwamae, and K. Yamanouchi. Ultrafast deformation of the geometrical structure of CO_2 induced in intense laser fields. *Phys. Rev. Lett.*, 83:1127–1130, 1999. 14, 16, 67, 72, 73, 74, 75, 76, 105, 106

[78] A. Hishikawa, A. Iwamae, and K. Yamanouchi. Ultrafast structural deformation of NO_2 in intense laser fields studied by mass-resolved momentum imaging. *J. Chem. Phys.*, 111:8871–8878, 1999. 14, 16, 67

[79] A. Iwamae, A. Hishikawa, and K. Yamanouchi. Extraction of molecular dynamics in intense laser fields from mass-resolved momentum imaging maps: application to Coulomb explosion of NO. *J. Phys. B: At. Mol. Opt. Phys.*, 33:223–240, 2000. 14, 17

[80] A. Iwasaki, A. Hishikawa, and K. Yamanouchi. Real-time probing of alignment and structural deformation of CS_2 in intense nanosecond laser fields. *Chem. Phys. Lett.*, 346:379–386, 2001. 14, 17, 21, 67, 82, 83, 85, 86, 88, 89, 106

[81] J.H. Sanderson, A. El-Zein, W.A. Bryan, W.R. Newell, A.J. Langley, and P.F. Taday. Geometry modifications and alignment of H_2O in an intense femtosecond laser pulse. *Phys. Rev. A*, 59:R2567–R2570, 1999. 14, 18, 67

[82] W.A. Bryan, J.H. Sanderson, A. El-Zein, W.R. Newell, P.F. Taday, and A.J. Langley. Laser-induced Coulomb explosion, geometry modification and reorientation of carbon dioxide. *J. Phys. B*, 33:745–766, 2000. 14, 18, 67, 71, 72, 73, 74, 75, 76, 105

[83] K. Zhao, G. Zhang, and W. T. Hill III. Image labeling: a graphical interface to correlation in multiparticle ejection dynamics. *Opt. Express*, 9:42–48, 2001. 18, 19

[84] K. Zhao, G. Zhang, and W. T. Hill III. Strong-field dissociative ionization of a linear triatomic molecule: Relationship between Coulomb-explosion energies and bond angle. *Phys. Rev. A*, 68:063408, 2003. Online abstract: `http://link.aps.org/abstract/PRA/v68/e063408`. 19, 20, 67, 75

[85] M. Brewczyk, K. Rzążewski, and C. W. Clark. Multielectron dissociative ionization of molecules by intense laser radiation. *Phys. Rev. Lett.*, 78:191–194, 1997. 19

[86] Ph. Hering, M. Brewczyk, and C. Cornaggia. Hydrodynamic description of laser-induced Coulomb explosion for small molecules. *Phys. Rev. Lett.*, 85:2288, 2000. 19

[87] H. Hasegawa, A. Hishikawa, and K. Yamanouchi. Coincidence imaging of Coulomb explosion of CS_2 in intense laser fields. *Chem. Phys. Lett.*, 349:57–63, 2001. 19, 20, 81, 83, 84, 85, 86, 88, 89, 106

[88] A. Hishikawa, H. Hasegawa, and K. Yamanouchi. Sequential three-body Coulomb explosion of CS_2 in intense laser fields appearing in momentum correlation map. *Chem. Phys. Lett.*, 361:245–250, 2002. 19, 21, 22, 81

[89] A. Hishikawa, H. Hasegawa, and K. Yamanouchi. Nuclear dynamics on the light-dressed potential energy surface of CS_2 by coincidence momentum imaging. *Chem. Phys. Lett.*, 388:1–6, 2004. 19, 21

[90] M. Ueyama, H. Hasegawa, A. Hishikawa, and K. Yamanouchi. Concerted and sequential Coulomb explosion processes of N_2O in intense laser fields by coincidence momentum imaging. *J. Chem. Phys.*, 123:154305, 2005. 19, 22, 61, 62, 88

[91] R. Dörner, V. Mergel, O. Jagutzi, L. Spielberger, J. Ullrich, R. Moshammer, and H. Schmidt-Böcking. Cold Target Recoil Ion Momentum Spectroscopy: a 'momentum microscope' to view atomic collision dynamics. *Phys. Rep.*, 330:96–192, 2000. 20, 69

[92] H. Hasegawa, A. Hishikawa, and K. Yamanouchi. Unpublished data. 20

[93] H. Kono, S. Koseki, M. Shiota, and Y. Fujimura. A theoretical study of electronic dynamics and deformation of CO_2 in intense laser fields. *J. Phys. Chem. A*, 105, 2001. 22, 23, 75, 87, 88, 105

[94] Y. Sato, H. Kono, S. Koseki, and Y. Fujimura. Description of molecular dynamics in intense laser fields by the time-dependent adiabatic state approach: Application to simultaneous two-bond dissociation of CO_2 and its control. *J. Am. Chem. Soc.*, 125, 2003. 22, 23

[95] F. Légaré, Kevin F. Lee, I. V. Litvinyuk, P. W. Dooley, S. S. Wesolowski, P. R. Bunker, P. Dombi, F. Krausz, A. D. Bandrauk, D. M. Villeneuve, and P. B. Corkum. Laser Coulomb-explosion imaging of small molecules. *Phys. Rev. A*, 71:013415, 2005. 22, 23, 67, 71, 75, 84

[96] B. Schenkel, J. Biegert, U. Keller, C. Vozzi, M. Nisoli, G. Sansone, S. Stagira, S. De Silvestri, and O. Svelto. Generation of 3.8-fs pulses from adaptive compresssion of a cascaded hollow fiber supercontinuum. *Opt. Lett.*, 28, 2003. 22

[97] A. H. Zewail. *Femtochemistry: Ultrafast Dynamics of the Chemical Bond*. World Scientific, Singapore, 1994. 23

[98] V. Sundström, editor. *Femtochemistry and Femtobiology: Ultrafast Reaction Dynamics at Atomic-Scale Resolution*. World Scientific, Singapore, 1994. 23

[99] A. W. Castleman Jr. and V. Sundström. Special issue on ten years of femtochemistry. *J. Phys. Chem. A*, 102:4021, 1998. 23

[100] P. W. Dooley, I. V. Litvinyuk, Kevin F. Lee, D. M. Rayner, M. Spanner, D. M. Villeneuve, and P. B. Corkum. Direct imaging of rotational wavepacket dynamics of diatomic molecules. *Phys. Rev. A*, 68:023406, 2003. 24

[101] Kevin F. Lee, F. Légaré, D. M. Villeneuve, and P. B. Corkum. Measured field-free alignment of deuterium by few-cycle pulses. *J. Phys. B: At. Mol. Opt. Phys.*, 39:4081–4086, 2006. 24

[102] F. Légaré, Kevin F. Lee, I. V. Litvinyuk, P. W. Dooley, A. D. Bandrauk, D. M. Villeneuve, and P. B. Corkum. Imaging the time-dependent structure of a molecule as it undergoes dynamics. *Phys. Rev. A*, 72:052717, 2005. Online abstract: `http://link.aps.org/abstract/PRA/v72/e052717`. 24, 25, 50, 53

[103] F. Légaré, Kevin F. Lee, A. D. Bandrauk, D. M. Villeneuve, and P. B. Corkum. Laser Coulomb explosion imaging for probing ultra-fast molecular dynamics. *J. Phys. B: At. Mol. Opt. Phys.*, 39:S503–S513, 2006. 24

[104] H. Stapelfeldt, H. Sakai, E. Constant, and P. B. Corkum. Formation and measurement of molecular quantum picostructures. *Phys. Rev. A*, 55:R3319–R3322, 1997. 24

[105] S. J. Walker. Development and characterization of a regeneratively amplified ultrafast laser system with an all-glass stretcher and compressor. Master's thesis, University of Waterloo, Waterloo, Ontario, Canada, 2006. URI http://hdl.handle.net/10012/2981. 26

[106] D. Strickland and G. Mourou. Compression of amplified chirped optical pulses. *Opt. Commun.*, 56:219–221, 1985. 26

[107] O. Svelto. *Principles of Lasers*. Plenum Press, fourth edition, 1989. 27

[108] M. Gisselbrecht, A. Huetz, M. Lavollée, T. J. Reddish, and D. P. Seccombe. Optimization of momentum imaging systems using electric and magnetic fields. *Rev. Sci. Instrum.*, 76:013105, 2005. 35

[109] Robert J. Cotter. *Time-of-Flight Mass Spectrometry - Instrumentation and Applications in Biological Research.* American Chemical Society, Washington, DC, 1997. 36

[110] T. Mizogawa, M. Sato, M. Yoshino, Y. Ito, and Y. Awaya. A two-dimensional position-sensitive anode for microchannel plates based on the "MBWC" technique. *Nucl. Instrum. Methods Phys. Res., Sect. A*, 387:395–400, 1997. 36, 38

[111] C. Firmani, E. Ruiz, C. W. Carlson, M. Lampton, and F. Paresce. High-resolution imaging with a two-dimensional resistive anode photon counter. *Rev. Sci. Instrum.*, 53:570–574, 1982. 37

[112] O. Jagutzki, V. Mergel, K. Ullmann-Pfleger, L. Spielberger, U. Meyer, R. Dörner, and H. Schmidt-Böcking. A broad-application microchannel-plate detector system for advanced particle or photon detection tasks: large area imaging, precise multi-hit timing information and high detection rate. *Nucl. Instrum. Methods Phys. Res., Sect. A*, 477:244–249, 2002. 37

[113] C. Martin, P. Jelinsky, M. Lampton, R. F. Malina, and H. O. Anger. Wedge-and-strip anodes for centroid-finding position-sensitive photon and particle detectors. *Rev. Sci. Instrum.*, 52:1067–1074, 1981. 37

[114] M. Yamamoto and E. Tanaka. Two-dimensional position-sensitive proportional chamber using weighted coupling capacitor read-out. *Radioisotopes*, 24:379–385, 1975. [Japanese]. 37, 38

[115] M. Yamamoto. Influence of amplifier noise on multi-wire proportional chamber using weighted coupling capacitor read-out. *Radioisotopes*, 24:386–390, 1975. [Japanese]. 37

[116] R. Allemand and G. Thomas. New position detector - backgammon device. *Nucl. Instrum. Methods*, 137:141–149, 1976. [French]. 37

[117] H. Shiromaru, K. Kobayashi, M. Mizutani, M. Yoshino, T. Mizogawa, Y. Achiba, and N. Kobayashi. An apparatus for position sensitive TOF measurements of fragment ions produced by Coulomb explosion. *Phys. Scr. T.*, 73:407–409, 1997. 38

[118] G. Veshapidze, T. Nishide, H. Shiromaru, N. Kobayashi, and T. Mizogawa. A time- and position-sensitive detector using a resistive film anode combined with a "modified backgammon with weighted capacitors" readout pad. *Jpn. J. Appl. Phys.*, 41:871–875, 2002. 39

[119] G. Veshapidze. Private communication. 39

[120] O. Bretscher. *Linear Algebra With Applications, 3rd ed.* Upper Saddle River NJ: Prentice Hall, 1995. 56

[121] J. A. Snyman. *Practical Mathematical Optimization: An Introduction to Basic Optimization Theory and Classical and New Gradient-Based Algorithms.* Springer Publishing, 2005. 57, 59

[122] W. Spendley, G.R. Hext, and F.R. Himsworth. Sequential application of simplex design of optimization and evolutionary operations. *Technometrics*, 4:441–461, 1962. 58, 71, 84

[123] F. H. Walters Jr., L. R. Parker, S. L. Morgan, and S. N. Demming. *Sequential Simplex Optimization: A Technique for Improving Quality and Productivity in Research, Development, and Manufacturing*. Boca Raton, FL: CRC Press, 1991. 58

[124] S. Liu, A. Hishikawa, A. Iwamae, and K. Yamanouchi. *Advances in Multiphoton Processes and Spectroscopy*. World Scientific, Singapore, 2001. Editors: Y. Fujimura and R. J. Gordon. 67

[125] J. H. Sanderson, R. V. Thomas, W. A. Bryan, W. R. Newell, A. J. Langley, and P. F. Taday. Alignment and bending of CO_2 by intense femtosecond laser pulses. *J. Phys. B: At. Mol. Opt. Phys.*, 31:L599–L606, 1998. 67

[126] A. S. Alnaser, C. M. Maharjan, X. M. Tong, B. Ulrich, P. Ranitovic, B. Shan, Z. Chang, C. D. Lin, C. L. Cocke, and I. V. Litvinyuk. Effects of orbital symmetries in dissociative ionization of molecules by few-cycle laser pulses. *Phys. Rev. A*, 71:031403(R), 2005. 67

[127] W. M. Johnstone, N. J. Mason, and W. R. Newell. Electron-scattering from vibrationally excited carbon-dioxide. *J. Phys. B: At. Mol. Opt. Phys.*, 26:L147–L152, 1993. 68

[128] T. Mizogawa, Y. Awaya, Y. Isozumi, R. Katano, S. Ito, and N. Maeda. New readout technique for 2-dimensional position-sensitive detectors. *Nucl. Inst. and Meth. A*, 312:547–552, 1992. 69

[129] B. Siegmann, U. Werner, H. O. Lutz, and R. Mann. Complete Coulomb fragmentation of CO_2 in collisions with 5.9 MeV u^{-1} Xe^{18+} and Xe^{43+}. *J. Phys. B: At. Mol. Opt. Phys.*, 35:3755–3765, 2002. 72, 74, 75, 77

[130] C. Cornaggia and Ph. Hering. Nonsequential double ionization of small molecules induced by a femtosecond laser field. *Phys. Rev. A*, 62:023403, 2000. 75

[131] J. H. Sanderson, T. R. J. Goodworth, A. El-Zein, W. A. Bryan, W. R. Newell, A. J. Langley, and P. F. Taday. Coulombic and pre-Coulombic geometry evolution of carbonyl sulfide in an intense femtosecond laser pulse, determined by momentum imaging. *Phys. Rev. A*, 65:043403, 2002. 76, 77, 97

[132] C. Cornaggia and L. Quaglia. Experimental observation of non-Coulombic states of transient multicharged molecular ions N_2^{4+} and O_2^{4+}. *Phys. Rev. A*, 63:030702, 2001. 77, 79

[133] L. Quaglia, O. Chiappa, G. Granucci, V. Brenner, Ph. Millié, and C. Cornaggia. Non-Coulombic states of N_2^{4+} and O_2^{4+} ions probed by laser-induced multi-ionization of N_2 and O_2. *J. Phys. B: At. Mol. Opt. Phys.*, 35:L145–L151, 2002. 77

[134] R. N. Coffee and G. N. Gibson. Identifying fragment vuv excitations with dissociative channels from the strong-field ionization of N_2. *Phys. Rev. A*, 72:011401, 2005. 77

[135] W. A. Bryan, W. R. Newell, J. H. Sanderson, and A. J. Langley. Observation of multiple ionization pathways for OCS in an intense laser field resolved by three-dimensional covariance mapping and visualized by hierarchical ionization topology. *Phys. Rev. A*, 74:053409, 2006. 77, 78, 105

[136] J. P. Brichta, W-K Liu, A. A. Zaidi, A. Trottier, and J. H. Sanderson. Comparison of ADK ionization rates as a diagnostic for selective vibrational level population measurement. *J. Phys. B: At. Mol. Opt. Phys.*, 39:3769–3779, 2006. 77

[137] J. S. Wright, G. A. DiLabio, D. R. Matusek, P. B. Corkum, M. Yu. Ivanov, Ch. Ellert, R. J. Buenker, A. B. Alekseyev, and G. Hirsch. Dissociation of molecular chlorine in a Coulomb explosion: Potential curves, bound states, and deviation from Coulombic behaviour for Cl_2^{n+} (n=2,3,4,6,8,10). *Phys. Rev. A.*, 59:4512–4521, 1991. 78

[138] P. Millié, I. Nenner, P. Archirel, P. Lablanquie, P. G. Fournier, and J. H. D. Eland. Theoretical and experimental studies of the triatomic doubly charged ions CO_2^{2+}, OCS^{2+} and CS_2^{2+}. *J. Chem. Phys.*, 84:1259–1269, 1986. 78

[139] H. Hogreve. Stability properties of CO_2^{2+}. *J. Phys. B: At. Mol. Opt. Phys.*, 28:L263–L270, 1995. 78

[140] M. Hochlaf, F. R. Bennett, G. Chambaud, and P. Rosmus. Theoretical study of the electronic states of CO_2^{++}. *J. Phys. B: At. Mol. Opt. Phys.*, 31:2163–2175, 1998. 78

[141] J. P. Nibarger, M. Li, S. Menon, and G. N. Gibson. Direct observation of excited state fragments following molecular ionization and dissociation in strong fields. *Phys. Rev. Lett.*, 83:4975–4978, 1999. 80

[142] L. Quaglia and C. Cornaggia. Experimental evidence of excited multicharged atomic fragments coming from laser-induced Coulomb explosion of molecules. *Phys. Rev. Lett.*, 20:4565–4568, 2000. 80

[143] S. Banerjee, G. R. Kumar, and D. Mathur. Dynamic and geometric alignment of CS_2 in intense laser fields of picosecond and femtosecond duration. *Phys. Rev. A*, 60:R3369–R3372, 1999. 81

[144] C. Y. Wu, H. Z. Ren, T. T. Liu, R. Ma, H. Yang, H. B. Jiang, and Q. H. Gong. Field induced ionization and Coulomb explosion of carbon disulfide. *Opt. Communications*, 216:133–138, 2003. 81

[145] J. X. Chen, R. Ma, H. Z. Ren, X. Li, C. Y. Wu, H. Yang, and Q. H. Gong. Kinetic energy release of diatomic and linear triatomic molecules in intense femtosecond laser fields. *Chinese Phys.*, 13:24–29, 2004. 81

[146] A. Saenz. On the influence of vibrational motion on strong-field ionization rates in molecules. *J. Phys. B: At. Mol. Opt. Phys.*, 34:4365–4372, 2000. 93, 94, 95, 97, 101

[147] J. H. Posthumus, L. F. Frasinski, and K. Codling. *Super Intense Laser-Atom Physics (Silap 2000) NATO Science Series*, volume 12. Dordrect: Kluwer, 2001. 93, 95, 97

[148] T. K. Kjeldsen and L. B. Madsen. Vibrational excitation of diatomic molecular ions in strong field ionization of diatomic molecules. *Phys. Rev. Lett.*, 95:073004, 2005. 93

[149] J. F. Xia, J. H. Sanderson, W.-K. Liu, and D. Strickland. Experimental observation of Raman chirped adiabatic rapid passage. *J. Phys. B: At. Mol. Opt. Phys.*, 36:L409–L414 and references therein, 2003. 93, 94, 101

[150] J. H. Posthumus and J. F. McCann. *Molecules and Clusters in Intense Laser Fields*. Cambridge: Cambridge University Press, 2001. 93, 94, 97, 98, 104, 107

[151] J. H. Posthumus. The dynamics of small molecules in intense laser fields. *Rep. Prog. Phys.*, 67:623–665, 2004. 93, 94, 97, 104, 107

[152] G. R. Hanson. Dissociative field-ionization of H_2 and HD. *J. Chem. Phys.*, 62:1161–1180, 1975. 93

[153] T. E. Sharp. Potential-energy curves for molecular hydrogen and its ions. *At. Data*, 2:119–169, 1971. 94

[154] K. P. Huber and G. Herzberg. *Molecular Spectra and Molecular Structure*, volume 4. Princeton, NJ: Van Nostrand-Reinhold, 1979. 94, 95

[155] J. Zuniga, A. Bastida, M. Alacid, and A. Requena. Variational calculations of rovibrational energies for CO_2. *J. Mol. Spectrosc.*, 205:62–72, 2001. 94, 96

[156] M. Brommer, G. Chambaud, E.-A. Reinsch, P. Rosmus, A. Spielfiedel, N. Feautrier, and H.-J. Werner. Theoretical potential energy function and rovibronic spectrum for CO_2^+ $X^2\Pi_g$. *J. Chem. Phys.*, 94:8070–8082, 1991. 94, 96

[157] R. S. Mulliken. Intensities of electronic transitions in molecular spectra II. Charge-transfer spectra. *J. Chem. Phys.*, 7:20–34, 1939. 94

[158] A. Saenz. Behavior of molecular hydrogen exposed to strong dc, ac, or low-frequency laser fields: I. Bond softening and enhanced ionization. *Phys. Rev. A*, 66:063407, 2002. 95, 96, 100

[159] E. W. Thulstrup and A. Andersen. Configuration interaction studies of bound, low-lying states of N_2^-, N_2, N_2^+ and N_2^{2+}. *J. Phys. B: At. Mol. Phys.*, 8:965–976, 1975. 96

[160] J. Liu, W. Chen, M. Hochlaf, X. Qian, C. Chang, and C. Y. Ng. Unimolecular decay pathways of state-selected CO_2^+ in the internal energy range of 5.2-6.2 eV: An experimental and theoretical study. *J. Chem. Phys.*, 118:149–163, 2003. 96

[161] R. J. Le Roy. Level 7.5: a computer program for solving the radial Schrödinger equation for bound and quasibound levels, 2002. *University of Waterloo Chemical Physics Research Report* CP-655 (the source code and manual for this program may be obtained for the 'Computer Programs' link on the www site http://leroy.uwaterloo.ca). 97

[162] NIST Chemistry WebBook http://webbook.nist.gov/chemistry. 98